Transition metal clusters on h-BN/Rh(111): surface interaction and catalytic activity.

THÈSE N^{O} 7521 (2017)

PRÉSENTÉE LE 24 MARS 2017

À LA FACULTÉ DES SCIENCES DE BASE
LABORATOIRE DE NANOSTRUCTURES SUPERFICIELLES
PROGRAMME DOCTORAL EN PHYSIQUE

ÉCOLE POLYTECHNIQUE FÉDÉRALE DE LAUSANNE

POUR L'OBTENTION DU GRADE DE DOCTEUR ÈS SCIENCES

PAR

Hamed ACHOUR

acceptée sur proposition du jury:

Prof. V. Savona, président du jury
Dr W. Harbich, Prof. H. Brune, directeurs de thèse
Dr F. Esch, rapporteur
Dr V. Dupuis, rapporteuse
Prof. M. Grioni, rapporteur

ÉCOLE POLYTECHNIQUE
FÉDÉRALE DE LAUSANNE

Suisse
2017

And your lord has decreed that you not worship except Him, and to parents, good treatment. Whether one or both of them reach old age with you, do not say to them a word of disrespect, nor scold them, but speak to them a noble word. And lower to them the wing of humility out of mercy and say, “My Lord, have mercy on them as they brought me up when I was small”. — The Quran

To my mother and father…

Abstract

The main aim of this dissertation is to study the catalytic aspects of very small transition metal clusters supported on h-BN/Rh(111). At very low scale, each system is unique and any modification in the support or cluster morphology, composition or size would considerably change the catalytic properties of the corresponding clusters. The originality of this work relies on the preparation and investigation of a model system in which h-BN/Rh(111) is the support to elucidate how does it influence the intrinsic properties of the catalyst. The catalytic reactions of interest were ammonia synthesis and CO oxidation on mass selected and soft landed iron and platinum clusters, respectively. A special focus was devoted to the investigation of the stability of these very small clusters on h-BN before and after the reaction. It was found that Pt_7 clusters soft landed at room temperature with an energy of 1.2 eV per atom and annealed to 700 K exhibit Smoluchowski ripening. Above this temperature, these clusters undergo partial intercalation between the h-BN monolayer and the Rh(111). The intercalation initiates at 900 K and becomes more pronounced when the clusters are annealed under gas reaction conditions. A high catalytic activity was observed when the Pt catalyst remains supported on h-BN. In this case, the reaction starts at 480 K and follows Langmuir-Hinshelwood mechanism. However, the catalytic activity strongly reduces when the Pt clusters undergo partial intercalation. Nevertheless, in this case the reaction starts at only 380 K, revealing a reduction by 100 K in the Pt poisoning as a result of substrate effect and charge redistribution. In a second trail, the cluster-h-BN interaction was studied through h-BN irradiation with Pt clusters, at room temperature, within an energy window of 30-416 eV/atom. The results show that even irradiation at 30 eV/atom can lead to entire non thermal intercalation of the clusters. The energetic Pt clusters were found to be site selective as they settle only under the h-BN wires, in contrast to soft landed Pt_7 clusters that were found to settle at the side edge of the h-BN depressions. After being exposed to irradiated Pt clusters, at an energy above 100 eV/atom, the h-BN layer starts to display visual cavity-type defects. These defects, induced by collision, disappeared after annealing to 600 K under gas reaction leaving behind an h-BN with no visual defects. CO temperature desorption spectroscopy (TDS) indicates that the intercalated Pt is inactive towards CO oxidation due to h-BN screening. Subsequently, we were able to produce a catalyst system made of soft-landed Pt/h-BN/intercalated Pt/Rh(111) using a combination between soft and energetic Pt deposition with which a reduction by 100 K in CO poisoning was obtained. Finally, ammonia synthesis was conducted on soft landed Fe_3 clusters, supported on h-BN/Rh(111) and deposited at 100 K under Ultra High Vacuum (UHV). Scanning tunneling microscopy (STM) displays two imaging states of the as deposited clusters; a ring state surrounding h-BN depression which disappears above 300 K and a dot like structure. The Fe clusters are found to grow by Ostwald ripening after annealing to 600 K and above this temperature, they endure partial intercalation. It was found that, in the presence of iron, the nitrogen reaction gas experienced an exchange with the nitrogen species forming the h-BN layer. TPR (Temperature Programmed Reduction) of N_2 with hydrogen revealed that nitrogen reduction occurs at 620 K, under high vacuum, following the Haber-Bosch method. The detection of NH and NH_2 reaction intermediates together with desorbed atomic nitrogen, during ammonia synthesis, confirms that the NH_3 formation involves the stepwise hydrogenation of adsorbed nitrogen.

Key words: Clusters, Catalysis, Soft landing, Energetic deposition, h-BN/Rh(111), Intercalation, CO oxidation, Ammonia.

Résumé

L'objectif de cette thèse est d'étudier les propriétés catalytiques des petits agrégats de métaux de transition sélectionnés en taille et déposés sur h-BN/Rh (111) , sous ultra-vide, à une énergie cinétique bien définie. Les réactions catalytiques étudiées sont la synthèse de l'ammoniac et l'oxydation du CO sur des agrégats du fer et du platine, respectivement. Une attention particulière a été consacrée à l'étude de la stabilité de ces petits agrégats soit avant ou après la réaction chimique. Du fait, il a été constaté que les agrégats Pt_7, déposés à température ambiante avec une énergie de 1,2 eV/atome suivi d'un recuit à 700 K, subissent une agglomération de type Smoluchowski. Au-dessus de cette température, ces agrégats endurent une intercalation partielle entre la mono-couche d'h-BN et la surface du Rh(111). L'intercalation initie à 900 K et devient fortement prononcée lorsque les agrégats sont recuits sous exposition aux gaz (CO et O_2) lors de la réaction chimique. Une activité catalytique élevée a été observée lorsque le catalyseur Pt n'a pas subi une intercalation. Dans ce cas, la réaction commence à 480 K en suivant le mécanisme de Langmuir-Hinshelwood. Par contre, l'activité catalytique diminue fortement lorsque les agrégats du Pt endurent une intercalation partielle. Néanmoins, dans ce cas, la réaction commence à 380 K, révélant une réduction de 100 K dans l'empoisonnement du Pt par CO, à cause de l'effet de la couche intercalée. Dans un deuxième essai, l'interaction agrégat-h-BN a été étudiée en exposant la couche d'h-BN au Pt_7, au sein d'une fenêtre d'énergie comprise entre 30 et 416 eV/atome. Les résultats montrent que dans cette gamme d'énergie, l'impact énergétique donne lieu à une intercalation totale des agrégats. Ces derniers s'installent uniquement sous des régions d'h-BN nommées "wires", contrairement à ceux déposés, avant, à 1.2 eV/atome et qui se posent au bord des régions d'h-BN nommées "dépressions". Notre étude montre que pour une énergie d'exposition supérieure à 100 eV/atome, la couche h-BN commence à paraitre des défauts visuels sous forme de cavités. Toutefois, ces défauts induits par collision disparaissent après un recuit à 600 K en présence du gaz (CO et O_2), laissant derrière une couche h-BN sans défauts apparents. La spectroscopie de désorption thermique (TDS) du CO indique que le Pt intercalé est inactif pour l'oxydation du CO, du fait d'un écrantage exercé par l'h-BN. Par la suite, nous avons pu produire un système catalyseur sous forme de Pt/h-BN/Pt intercalés/Rh(111), en utilisant une combinaison de deux types de dépôt; doux et énergétique. Avec ce système, une réduction de 100 K dans l'empoisonnement du Pt par CO a été obtenue. Enfin, la synthèse de l'ammoniac a été menée sur des agrégats de Fe_3 supportés sur h-BN/Rh(111) avec une énergie de 1,2 eV/atome à 100 K. La microscopie à effet tunnel révèle deux états d'imagerie des agrégats déposés; un état ayant la forme d'un anneau entourant les zones de dépression et qui disparaissent au dessus de de 300 K, et un autre état de forme sphérique. Après un recuit à 600 K, les agrégats de Fe_3 croissent par un mûrissement de type Ostwald et au-delà de cette température ils endurent une intercalation partielle. La dissociation du N_2 moléculaire a été étudier à l'aide du TDS qui montre que l'azote atomique (N) et moléculaire (N_2) désorbent autour de 710 et 670 K, respectivement. Il a été constaté que, en présence du fer, le gaz d'azote de la réaction effectue un échange avec l'azote constituant la couche h-BN. L'étude par TPR (réduction à température programmée) de la réaction du N_2 avec l'hydrogène, a révélé que la réduction de l'azote a lieu à 620 K. Au cours de la synthèse de l'ammoniac, les intermédiaires réactionnel NH et NH_2 ont été détecté. L'observation directe de la dissociation atomique d'azote et des radicaux NH et NH_2 durant la synthèse du NH_3 sur une surface catalytique en utilisant la spectroscopie de désorption est considéré comme une première.

Mots-clés: Agrégats, Pt, Fe, Catalise, h-BN/Rh(111), Intercalation.

Contents

List of Figures

List of Tables

Introduction

In 1981, Swiss researchers "Gerd Binnig" and "Heinrich Rohrer" invented scanning tunneling microscope which has enabled scientists for the first time to deal directly with atoms and molecules, through atomic imaging and manipulation to form nanoparticles.[17] Nanoscience study the basic principles of molecules and compounds that do not exceed 100 nm where a nanometers is a unit of measurement equal to 10^{-9} m. Clusters, are nanoparticles of somewhere between 1 and 10^6 atoms. The properties of small clusters are dominated by a drastic change in surface properties and quantum effects related to electronic confinement. When materials are cut down to very small sizes, the continuum of the bulk electronic states breaks up into discrete states. At very small size, adding or removing even one atom could modify the clusters properties. In fact, investigation of size dependent chemical reactivity of Pt_n ($8 < n < 20$) clusters on MgO(100) showed that every single Pt atom composing the supported cluster counts for this reactivity.[18] Also, study on gold showed that Au_8 supported on MgO is the smallest cluster that is effective for catalysis.[19] Sources for generating particles commonly give rise to clusters with broad size distributions. In order to investigate and exploit the size dependent cluster properties, mass selection technique is vital. There are many techniques in place to achieve mass selection, among them are two most commonly used techniques; quadrupole mass analyzers, used in the present work (see chapter 4), and time-of-flight mass spectrometers.

Two approaches for nanoparticle elaboration are worthy of mention: top-down and bottom-up approachs. The former consists in miniaturizing objects already in the micro or macroscopic size to reach the nanoscale using a sequence of technological steps originating from microelectronics. The major drawback of this approach is its resolution limit. The bottom-up approach consists in assembling elementary species (atoms, molecules or clusters) to build up more complex structures. This is the way employed in almost all clusters-studies including this one.

During the last three decades, cluster science state of the art has been dedicated to free clusters in the gas phase. Studies of free clusters are the key to understand the evolution of the electronic and geometric structure with size. The first catalytic reaction on a free metal cluster was pioneered with cyclopolymerization of ethylene to synthesis benzene using free ${Fe_4}^+$ clusters.[20] Bohm and his group published a comprehensive study on nitrogen oxide reduction with CO using 29 transition metal cations.[21] Nevertheless, for clusters to be useful in catalysis applications, they need to be dispersed on a suitable support. Better choice of a support should combine several properties such as inertness, high chemical and thermal resistivity to be efficient in catalysis applications. Metal oxide surfaces have been widely used in catalysis as supports for metal catalysts. The support effect on the clusters reactivity is nowadays established, as evidences for such effect are numerous. For example, point defects in MgO support could either enhance or quenche the catalytic activity of the catalyst depending on their types.[22] The effect of the reduction state of the TiO_2 support on the catalytic activity of the supported Pt clusters has been analyzed. It is demonstrated that small platinum clusters (in this case Pt_7) are two orders of magnitude more active toward CO oxidation when they are supported on slightly reduced TiO_2 crystals than when they are supported on strongly reduced ones.[23,24] In the latter case, the reduction in catalytic activity is due to the formation of a TiO_x ($0 < x < 2$) encapsulation layer on the clusters upon annealing. This phenomenon is referred to as SMSI effect (strong metal-support interaction) and is known to occur when a metal oxide is used as a support, but in the absence of strong support interactions, clusters can be considered as pseudo-free.

Clusters supported on templated monolayers like h-BN grown on Rh(111) and graphene grown on Ir(111) with moiré pattern periodicity are very promising for catalysis. Example that is included within this thesis is the moiré structures of h-BN/Rh(111)-(12×12) (see chapter 3). In the particular case of h-BN as a support, works on catalytic activity of metal clusters are very few. Recent experimental[25–27] and theoretical[28–30] results demonstrated that metal catalyst supported on h-BN can exhibit better catalytic activity. One of such works has been devoted to oxygen adsorption on defective h-BN sheet supported Pt which was conducted using DFT.[29] The so supported Pt nanoclusters were found to exhibit good catalytic performance for the Oxygen Reduction Reaction (ORR).

Very small nanoparticles like the ones investigated here are very unstable against temperature and reactive gases and the knowledge of bonding strength and morphology change is of crucial importance. In the case of stabilization by defects, for instance, in the case of isolated Pd atoms adsorbed on MgO surface, it was found that bonding of Pd is about three times stronger on defect site such as oxygen vacancy than on O anion defect (coordinatively unsaturated anion).[31] In the case of h-BN support, defects centers are expected to be sparse. Thereafter, the h-BN would bring on the moiré modulability as cluster stabilizer. The difference in the work function between the h-BN wires and depressions regions gives rise to an energy barrier for atoms and molecules trapping.[32] Supported Pd_{19} on h-BN/Rh(111), for example, were found stable up to a temperature as high as 700 K.[33]

Clusters-surface interaction, from soft landing to implantation, can be defined by the clusters kinetic energy. Different techniques are used for clusters generation in vacuum providing a possibility for control of cluster size and energy distribution. For example, the clusters can be produced by high energy ion sputtering then size-selected by a quadrupole mass filter and afterwards soft-landed or accelerated by an ion-optical system. This procedure was used in this thesis. In conventional ion implantation and depending on kinetic energy, the energetic elastic collision of an incident projectile with the atoms of a surface can lead to cluster penetration into the substrate. In some cases, when the energy is high enough, pining, craters formation and surface atoms ejection can be observed. High energy cluster projection on a surface can be used to promote chemical reactions[34,35] or surface polishing.[36] Low-energy cluster implantation, in the order of ten to hundred of eV per atom, is found to be a promising technique for ultra-shallow junction formation and infusion doping of shallow layers[37] which is not possible for conventional ion implantation. It is worth noting that the cluster penetration energy in this case must be significantly lower than the penetration threshold energies of monomer ions. The cluster energy (sum of individual atoms) divided by the very small surface collision area grants high values of the energy density. For example, Ar_n penetrates silicon at 4.7 eV per cluster atom and at 15-20 eV in the case of argon monomers.[38]

This thesis focuses on the stability and the catalytic activity of h-BN/Rh(111) supported Pt and Fe mass selected small clusters. The reactions of interest are CO oxidation and ammonia synthesis. CO oxidation on noble metal catalysts is one of the most studied reactions, as shown by the literature,[39] on various types of surfaces: single crystals, particles models, thin films and supported catalysts. Indeed, CO oxidation has many industrial and academic interest due to the simplicity of the structure of reagents (CO/O_2) and product (CO_2), which makes it a model reaction. Ammonia is consistently among the top chemicals produced in the world. The major use of ammonia is as a fertilizer. It is commonly produced by the Haber-Bosch process, which involves the direct reaction of elemental hydrogen and elemental nitrogen. This reaction requires the use of a Fe based catalyst at high pressure (100–1000 atmospheres) and elevated temperature (400-550 °C). In this work, the stability of Pt and Fe clusters was addressed by studying the influence of the surface temperature and the gas reaction on the mobility and the cluster morphology where cluster coalescence can occurs with increasing annealing conditions and eventually intercalation of the catalyst also can occurs at elevated temperature.

This thesis is structured in several chapters. The first, second and third chapter introduce the reader to related theories. Chapter 4 gives an account of the main experimental designs and routes used to accomplish this work. The results on the Pt/h-BN/Rh(111) system are presented in chapter 5, 6 and 7. CO oxidation reaction in conjunction with cluster stability is reviewed in chapter 5. Cluster-surface interaction using high energy Pt irradiation is exposed in chapter 6. Catalyst deactivation can results from many causes, such as CO poisoning of the catalyst active sites issued from high CO-Pt binding energy. In chapter 7, we propose a method to reduce Pt catalyst poisoning by introducing an intermediate Pt layer between the h-BN and the Rh(111) surface. In chapter 8, ammonia synthesis was studied using pure Fe small clusters following the Haber-Bosch route but under UHV. The Fe Cluster morphology and stability, in particular during chemical reaction was also studied. Finally, chapter 9 summarizes the results and gives brief final conclusions.

1 Catalysis

Catalysis is used in tremendous chemical reactions to facilitate the reaction process by breaking and forming new bonds. All of this happens without a significant change of the catalyst during the reaction pathway. In the absence of the catalyst, the chemical transformation would not occur or requires a very high amount of energy to be efficient. In order to transform the reactants into products, an energy barrier represented by the activation energy must be overcome. If the energy barrier of the catalytic path is much lower than the barrier of the noncatalytic path, significant enhancements in the reaction rate can be realized by use of a catalyst. The role of the catalyst is therefore to modify the energy profile so the activation energy is lowered compared to non-catalyzed system (see Figure 1.1).[40] It has been estimated that catalysis-based processes represent 90 % of current chemical processes and generate 60% of today's chemical products. Catalysis research focuses on promoting selectivity and efficiency and as well as design and development of a new cheap and efficient catalyst.[41]

Catalysts are divided in two main groups: homogeneous catalysts, where the catalyst is in the same phase as the reactants, usually in solution (example of homogeneously catalyzed reaction is the oxidation of toluene to benzoic acid in the presence of Co and Mn[42]) and heterogeneous catalysts, in which the catalyst is in a different phase from the reactants. Typically, heterogeneous catalyst involves a solid catalyst with the reactants as either liquids or gases. One Example of heterogeneously catalyzed reactions are ammonia synthesis over promoted iron catalysts.[43] In this thesis, all studied reactions are of heterogeneous type.

1.1 Heterogeneous catalysis mechanisms and kinetics

In heterogeneous catalysis, the reaction involves adsorption of reactants from a gas phase onto a solid surface, surface reaction of adsorbed species and desorption of products into the gas phase. Explicitly, catalysis follows a cycle of elementary steps (at least three). Before A and B species can react, they must both adsorb on the catalyst surface. The next event is an elementary step that proceeds through a reaction of adsorbed intermediates and is often referred to as a Langmuir-Hinshelwood (LH) step. As an example, the oxidation of carbon

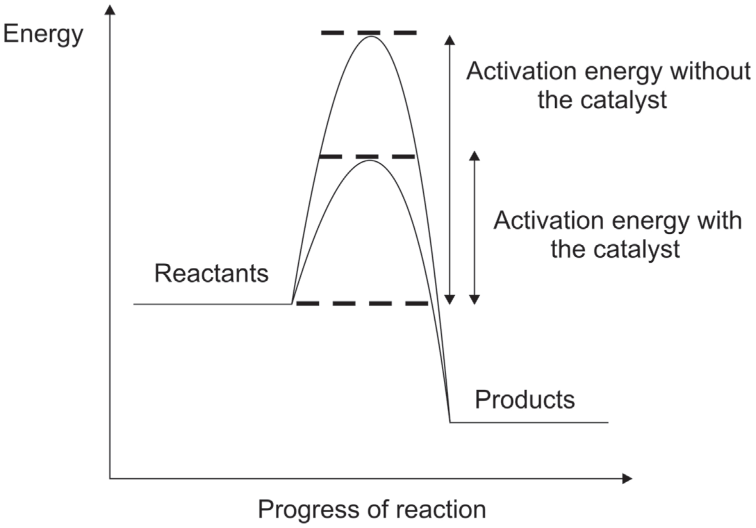

Figure 1.1 – The reaction is energetically favorable but due to a high energy barrier its reaction rate is very small. A catalyst decreases the reaction barrier by creating an alternative reaction path that leads to the same result.

monoxide by molecular oxygen is considered to proceed through the LH mechanism.[44] The rate expression for the bimolecular reaction depends on the number density of adsorbed A molecules that are adjacent to adsorbed B molecules on the catalyst surface. In the case of the Langmuir-Hinshelwood mechanism, the reaction can be written as:

$$\begin{aligned} A^{(g)} + * &\rightleftharpoons A* \\ B^{(g)} + * &\rightleftharpoons B* \\ A* + B* \rightarrow AB* &\rightarrow AB^{(g)} + * \end{aligned} \tag{1.1}$$

where * represents the adsorption sites, A, B and AB are, respectively, the two reactants and the product, and (g) indicates that the molecule is in the gas phase. The milestone for the reaction rate is the one involving the two molecules, which must be sufficiently close to interact. For such a recombination reaction, the rate at which the atoms diffuse on the surface is the limiting step. A simplified rate expression for such reaction is:

$$r = k[A^*][B^*]/[*]_0 = k[*]_0\theta_A\theta_b \tag{1.2}$$

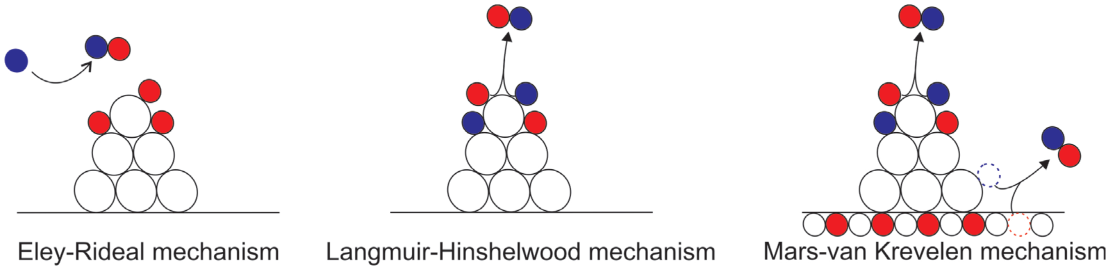

Figure 1.2 – Heterogeneous catalysis mechanisms: Eley-Rideal, Langmuir-Hinshelwood and Mars-van Krevelen.

where $[*]_0$ is the total number of adsorption sites, θ_A and θ_B are the fractional surface coverage for A and B. Their expression is given by:

$$\theta_A = \frac{K_{adsA}[A]}{1 + K_{adsA}[A] + K_{adsB}[B]} \quad , \quad \theta_B = \frac{K_{adsB}[B]}{1 + K_{adsA}[A] + K_{adsB}[B]} \tag{1.3}$$

K_{ads} is a proportionality constant, $K_{ads} = k_{ads}/k_{des}$, where k_{ads} and k_{des} refer to the rate constants for adsorption and desorption, respectively. Thus, the overall rate of reaction of A and B can be expressed as:

$$r = \frac{kK_{adsA}K_{adsB}[*]_0[A][B]}{(1 + K_{adsA}[A]K_{adsB}[B])^2} \tag{1.4}$$

Another event in which the reaction occurs between a reactant molecule in the gas phase and one that is adsorbed on the surface is termed Eley-Rideal mechanism. A gas-phase molecule collides, according to this mechanism, with another molecule adsorbed on the surface for the reaction to proceed. For the case of supported model catalyst, an Eley-Rideal mechanism has so far not been unambiguously identified. It was found experimentally that most of reactions follow Langmuir-Hinshelwood kinetics due to the extremely short time scale (picosecond) of a gas-surface collision. However for the gas-phase clusters, due to the need of reactant-molecule collision, the Eley-Rideal mechanism is more likely to happen. The oxidation of CO on small gold gas-phase clusters is an example.[45] The reaction rate is proportional to the partial pressure of the gas-phase reactant. In the case of the Elay-Rideal mechanism the reaction can be written as:

$$\begin{aligned} & A^{(g)} + * \rightleftharpoons A* \\ & A* + B^{(g)} \rightarrow AB* \rightarrow AB^{(g)} + * \end{aligned} \tag{1.5}$$

If [B*] = K_2 [A*] and [A*] = K_1 [*] with [*] is the concentration of the vacant sites on the surface, the rate equation becomes r = kK_2K_1 [A] [*]. Calculating in the same way as previously, we get the final rate expression as:

$$r = \frac{kK_2K_1[A][*]_0}{(1+(K_1+K_2K_1))[A]} \tag{1.6}$$

In this case, the catalytic reaction depends on the adsorption-desorption behavior of just one of the reactants. Langmuir-Hinshelwood will predominate in the case of strongly bound reactants with large diffusion constants. Whereas, the Eley-Rideal mechanism will rule over in the case the reactants are weakly bound with small diffusion constants. Finally, there is a third mechanism similar to the Eley-Rideal mechanism except that the products are formed from adsorbed reactants and reactants coming directly from the catalyst structure. The process is known as Mars-van Krevelen mechanism[46,47] which predominates in the case, for example, of metal oxide catalysts containing readily reducible metals. In that case, the oxygen consumed during the reaction is continuously regenerated by the oxide layer from the gas phase to preserve the catalyst properties. Figure 1.2 summarizes all the tree mechanisms mentioned above.

1.2 Selectivity

The term selectivity is used to describe the tendency of a reaction to follow a specific path to produce a certain reaction product when several products are involved. Activity has always been an important characteristic for a heterogeneous catalyst in the twenty century, increasing the rates to produce more molecules per unit time while selectivity was of lesser concern because of raw materials abundancy and of undesirable low cost byproducts. Modifying a catalyst in such a way that it becomes 100 % selective for a given chemical reaction is a task for the twenty first century because waste disposal is now expensive and the negative environmental side-effects are considerable.[41,48] The selectivity of metal nanocatalysts, for example, can be modified by controlling the interfacial electronic effects, using organic modification of the metal surface.[49] The catalyst selectivity is measured by the fractional selectivity, S_F, which, for each reaction product, is defined as:

$$S_{F,j} = p_j / \Sigma_i p_i \tag{1.7}$$

where p_i is the amount of product i produced, and by the relative selectivity, S_R, for each pair of products

$$S_{R,j,i} = p_j / p_i \tag{1.8}$$

1.3 CO oxidation on platinum (example 1)

Carbon monoxide is a toxic and harmful gas for humans and animals due to its high affinity with hemoglobin. Huge amounts of carbon monoxide are emitted in the world (1.1 billion tons in 2000), mainly from transportation, power plants, industrial and domestic activities. To achieve CO elimination, it is necessary to catalyze its oxidation. CO oxidation reaction has been extensively studied over the last decade. Some oxides such as hopcalite (a mixture of copper and manganese oxides) have been known to oxidize CO at ambient temperature[50] while noble metals (Pt, Pd and Rh) are highly active towards this reaction.[51] The oxidation of carbon monoxide (CO) on Pt-group metals is one of the most studied prototypical catalytic reactions because of its practical relevance and general applicability.[44,52] Despite its apparent simplicity, the reaction is challenging to study and describe because of peculiar kinetics such as bistability and oscillations, and fascinating spatio-temporal behavior.[53] The oxidation of CO on platinum is known to proceed via the classical Langmuir-Hinshelwood (LH) mechanism which involves the adsorption and reaction of molecular CO with atomic oxygen over metallic platinum surfaces.[24] According to Eq. 1.1, the reaction is resumed by the following equations:

$$\begin{gathered} O_2^{(g)} + * \rightleftharpoons O_2 * \rightarrow 2O * \\ CO^{(g)} + * \rightleftharpoons CO * \\ CO * + O* \rightarrow CO_2 * \rightarrow CO_2^{(g)} + * \end{gathered} \tag{1.9}$$

Where ’g’ donates to species in the gas phase and ’*’ to a surface vacant site. The catalytic reaction cannot be completed if the Pt surfaces become poisoned by adsorbed CO, which prevents dissociation of O_2. When CO is first adsorbed, oxygen adsorption will be difficult since O_2 molecule should find a pair of adjacent Pt sites to be able to adsorb.[54] This is because,

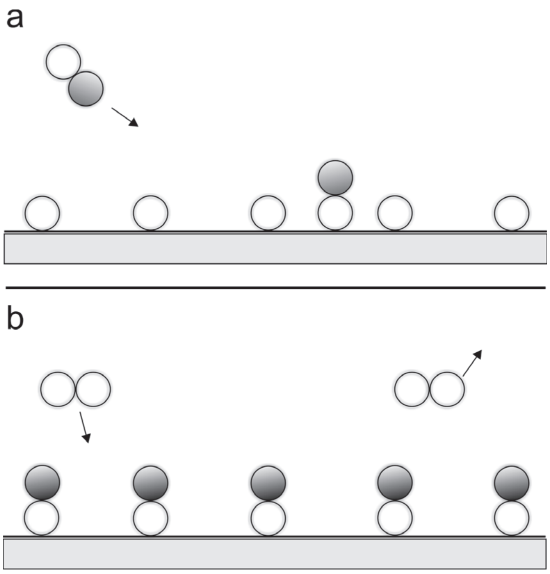

Figure 1.3 – CO and O_2 adsorption on a precovered surface. (a): CO adsorption on predosed surface with O_2. (b): O_2 adsorption on predosed CO.

contrary to CO, oxygen adsorbs dissociatively on most metals at ambient temperature, which requires two adjacent metal atoms. Depending on the adsorption sequence, surface coadsorption of the two species is quite different. When the surface is rich in oxygen (Fig. 1.3a) there still enough place to host CO molecules. In the case of a rich CO surface (Fig. 1.3b), oxygen adsorption is completely blocked due to the lack of available pairs of neighbor sites. The presence of adsorbed CO on the Pt surface limits the oxygen adsorption to a point that the catalyst becomes inactive at temperatures lower than the desorption temperature of CO from the Pt(111) surface, *i.e.*, 450 K.[55] For example, the car catalysts start to perform the CO combustion only a few minutes after the ignition of the car, when the exhausted gases warm them up to the working temperature. CO poisoning is harmful to Pt catalyst in applications such as in fuel cells. Despite almost one century of research on this reaction over clusters, this poisoning is still not fully understood simply because it is extremely difficult to see what exactly happens on very small metallic clusters.[56]

1.4 ammonia synthesis with the Haber-Bosch process (example 2)

Ammonia production is one of the largest mankind synthetic chemical reaction. It is of strategic importance due to its wide utilization ranging from drugs to explosives production and its main application which is the production of fertilizers used in agriculture. Nowadays, ammonia is produced with Haber-Bosch process.[57] In industrial practice, the catalyst consists of highly porous particles with a core of magnetite (Fe_3O_4), encased in a shell of wüstite (FeO), which in turn is surrounded by an outer shell of iron metal. The reaction temperature ranges between 673 and 773 K under 15 to 20 Mpa of pressure of N_2/H_2 gas mixture (25 % N_2 and 75 % H_2). The active catalyst for this process are based on iron promoted with K_2O, CaO, SiO_2, and Al_2O_3 which support the iron catalyst and help it maintain its surface area. Addition of promoters, such as potassium, to iron catalyst can enhance ammonia synthesis by decreasing the barrier for the rate determining step. This was found to be due to electrostatic effects of the potassium.[58] The electric field of a potassium atom provokes a stark effect to nearby molecules, thereby splitting the molecular orbitals and allowing more electron density to enter into the antibonding orbitals. This then would lower the barrier for the rate determining step.[59]

The ammonia production from nitrogen and hydrogen is an exothermic reaction:

$$N_2 + 3H_2 \rightleftharpoons 2NH_3 + 92.4\ kJ/mol \tag{1.10}$$

Industrially, 3 steps are realized for ammonia synthesis:

- Methan conversion with water vapor and production of CO/H_2 mixture.
- CO elimination from the synthetic gas using H_2O.
- NH_3 synthesis using Harber-Bosch process.

Without any catalyst, breaking the N-N and H-H bonds to form reactive atoms needs a huge amount of energy. The spontaneous ammoniac formation in N_2-H_2 mixture at a temperature below 773 K does not proceed at a detectable rate. However, the use of a catalyst allows nitrogen and hydrogen dissociation through adsorption on its surface and reacting to form NH_3.

The reaction mechanism, involving the heterogeneous catalyst for ammonia synthesis, is believed to involve the following steps :

$$\begin{aligned}
N_2^{(g)} + * &\rightleftharpoons N_2* \rightarrow 2N* \\
3H_2^{(g)} + * &\rightleftharpoons 3H_2* \rightarrow 6H* \\
N* + 3H* &\rightarrow NH* + 2H* \\
NH* + 2H* &\rightarrow NH_2* + H* \\
NH_2* + H* &\rightarrow NH_3* \rightarrow NH_3^{(g)} + *
\end{aligned} \tag{1.11}$$

Where 'g' donates to species in the gas phase and '*' to a surface vacant site. All the reaction steps for ammonia production are represented in the energy profile in Figure 1.4 for the cat-

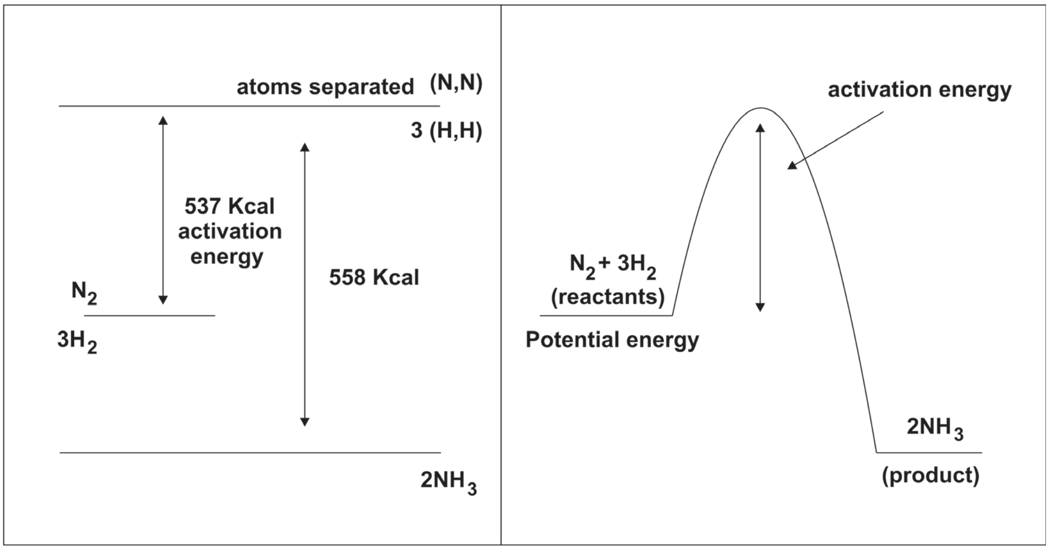

Figure 1.4 – Energy profile diagram of the ammonia production in the gas phase and on an iron surface in kJ/mole. Adapted from Ref.[1]

alyzed reaction and for the reaction in the gas phase. The nitrogen and hydrogen molecules dissociate on the iron surfaces.[60] Hydrogen atoms sequentially react with the atomic nitrogen until NH_3 is formed and desorbed. These steps are summarized by the schematic of Figure 1.5. It is believed that the overall reaction rate of ammonia synthesis is determined by dissociation of nitrogen adsorbed on the catalyst surface under reaction. Nevertheless, there is evidence of experiments performed at higher pressures, suggesting the step of hydrogen reaction with adsorbed nitrogen to be the rate-determining.[61]

1.5 Model catalysts

Model catalysts, such as single crystals are used to realize and study the surface chemistry and structure by investigating catalytically active sites on the atomic scale, usually at ultrahigh vacuum.[53] Catalysis shows very complex kinetics on supported clusters and depends on numerous parameters such as particle size, structure and support effect. In order to understand the reaction mechanisms, a simplified version of the problem needs to be considered. For this reason model catalysts are produced and studied in ultra high vacuum with the powerful tools of surface science. Several types of supported metal model catalysts have been developed. The simpler model consists in single crystal surfaces whose properties are controlled at the atomic scale. Keeping the system as simple as possible, these models open the possibility to introduce certain complex properties of real catalysts, and most importantly they are still easily accessible for most surface science probes.[62] CO combustion on Pt surfaces and Haber-Bosch process, already discussed above, are two examples of these kinds of systems. More complex models, based on supported nanoclusters, inspired by real catalysts, are now broadly used. These complex model catalysts are synthesized for the purpose of understanding processes such as

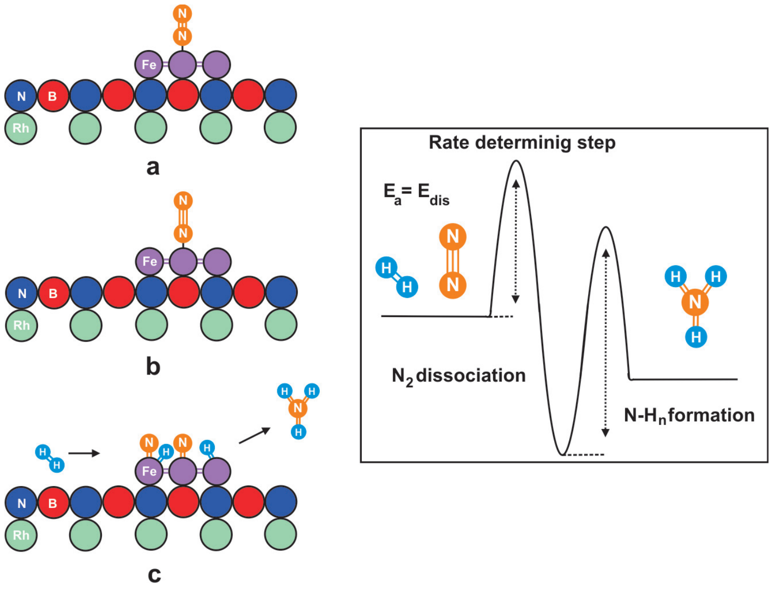

Figure 1.5 – Proposed reaction mechanism and energy profile for ammonia synthesis over iron cluster catalysts. (a) the reacting gases (N_2 and H_2) adsorb onto active sites on the iron clusters. (b) the N-N bond distance is more or slightly lengthened (depending on the interaction with cluster surface) while adsorbed on the surface compared to the N-N distance in the N_2 gas molecule. (c) reagents undergo chemisorption that results in dissociation into adsorbed atomic species and where nitrogen and hydrogen react on the catalyst surface through Langmuir-Hinshelwood mechanism to form NH_3 in which N_2 dissociation is the rate determining step. (d) the energy barrier (E_{dis}) for this mechanism corresponds to the apparent activation energy (E_a) for ammonia synthesis.

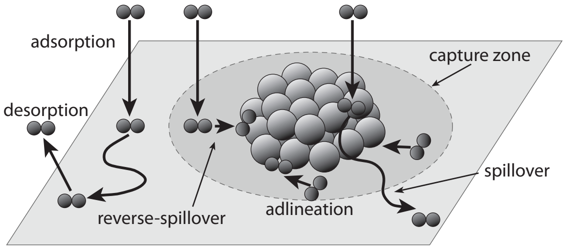

Figure 1.6 – Representation of the dynamic phenomena that can take place in a catalytic process on supported nanoparticles. Adapted from Ref.[2]

the effects of the cluster size,[63–66] shape[67,68] and composition.[69]

1.6 Catalysis on supported clusters

At very small scales, supported clusters are very complex systems in catalysis. The reaction dynamic depends on the composition and structure of the catalyst. For example, the effects of geometrical structure induce different atomic arrangements from those of solids. Small clusters give rise to faces, kinks and corners each exhibits different adsorption sites. Interaction with the support material is another important factor. It can modify the morphology, the electronic properties and the catalyst reactivity and selectivity. All these parameters have a great influence on the reaction kinetics and should be taken in consideration in designing supported size-selected cluster catalysts. A representation of the adsorption-desorption processes taking place in the vicinity of a supported cluster is shown in Figure 1.6. In the following, some of these effects[70] are, briefly, presented:

- **Support related effects:** The dynamic of reaction on supported nanoparticles is in general more complex than in the case of reactions on single crystal surfaces. The higher complexity is due to the fact that supported metal clusters expose different faces each of which can interact differently with the adsorbates. At the same time the presence of the substrate can modify the behavior and the adsorption dynamics of the adsorbates in ways that can both enhance or hinder the catalytic performance of the clusters. In fact, metal-support interaction does not always lead to a decrease of activity, as is usually observed for strong metal-support interaction, but can considerably increase it[71] as a result of a strong electronic interaction between metal particles and the support.[72] The support can alter the intrinsic cluster properties in many ways. Surface defects, for example, could act as an electron traps or donor centers to the reaction. A correlation is found between Au reactivity for CO oxidation and defects concentration in MgO support.[73] Moreover, the cluster size and the strength of its interaction with the surface could have an effect on the cluster-surface wettability and consequently on the cluster shape and configuration. It can modify whether the cluster is in 2D or 3D shape and also which crystallographic planes are exposed to the reactants.

Besides the mentioned effects, reactants dynamic (migration, adsorption) on the cluster surface can act differently in the presence of a support. In this respect, well-established phenomena such as spill-over and reverse spillover are of great importance in the dynamics of nanocatalysis. In the former, intermediate reactants migrate from the surface of the cluster to the substrate where they can react, for example with defects, before desorbing (Fig. 1.6). In the latter, the adsorbed species on the support diffuse toward the catalyst. If they reach an area, called the capture zone, of a catalyst particle, they migrate onto the metal and then participate in the reaction. This area depends on defects concentration, temperature, adsorption and diffusion of reactants, and also on the cluster surface density. More interesting, however, is the situation at the periphery of the cluster/support. This process assumes that the reaction proceeds at the particle/-substrate interface, or more particularly metal/oxide, where special types of reaction sites appear along the interface. However, there is little direct experimental evidence for that, although this process has repeatedly been suggested for the combustion of CO on Au nanoparticles.

- **Electronic size effects:** The limited number of atoms in small clusters gives rise to discrete electronic levels and high surface to volume ratio. This should have important implications on the catalyst binding energy, *i.e.*, the chemical reactivity towards adsorbate species. Charge transfer between the clusters and the support determines their mutual interaction as well as the dynamic of clusters (ripening, coalescence) through their bonding character to the support. The charge state of the catalysts can change considerably their reactivity. For example, negatively charged Au clusters have been found to activate O-O bond while positively charged ones promote CO and hydrocarbons adsorption.[74,75]

- **Geometrical effects:** As the cluster size decreases, the proportion of low coordinated atoms increases. This would rises the concentration of steps and kink sites and therefore promotes the activity of the catalyst which has been interpreted in terms of the enhanced proportion of the low-coordinated sites at the cluster surfaces. Metal nanoclusters surrounded by well-defined facets show better catalytic activities compared to their bulk surfaces. Metal nanoclusters enclosed by multi-facets are very noble catalysts and are reported to be very promising for electro-catalytic reactions due to the presence of high surface insaturations.[3] A 1 nm size of octahedral nickel nanocluster (Ni_{85}) enclosed by well-defined low index facets (eight (111) facets) (Fig. 1.7) is an example that is mainly observed in the experimentally synthesized Ni-nanoclusters.[76,77]

- **Restructuring effects:** It is not excluded that the cluster surface suffers restructuring during catalytic reaction. Interaction with the reactants can modifies the cluster shape, induces ripening or can change the chemical composition of the clusters.

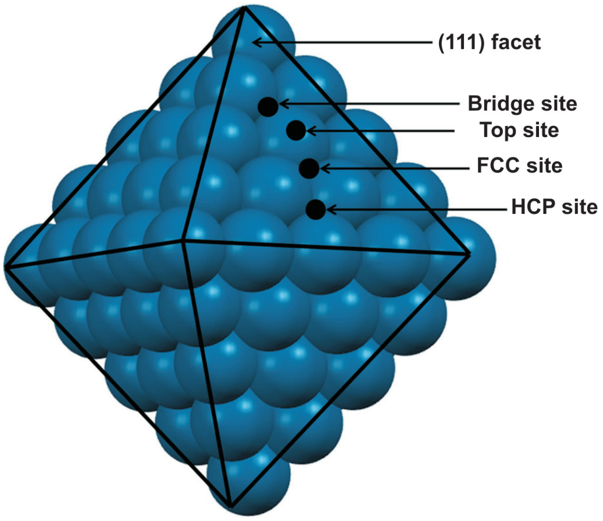

Figure 1.7 – Octahedral Ni_{85} nanocluster enclosed by eight (111) facets. Adapted from Ref.[3]

2 Clusters

Clusters are particles consisting of a limited number of atoms or molecules, linked by various bonds. They are composed from two to around 10^6 atoms. Clusters were observed and used by humans since ancient times. For example, they were already used in the middle ages by the glaziers who discovered a way to make beautiful stained glass by a suitable treatment of the glass containing various metals. The superb color results were due to the diffraction of light by small metal clusters dispersed in the glassy mass. The characteristics of clusters are due to their defined size, which results in high surface to volume ratio making them suitable for applications in the field of catalysis and gas sensing. Moreover, the energy separation of small cluster electronic levels is quite close to that of a molecule and varies as function of cluster size. It is therefore considered as an intermediate state between the atoms or molecules of the gas phase and the bulk state. The clusters properties can give rise to physical and chemical properties different from that of the bulk state. Haruta, in his work in the field of catalysis, found that small Au clusters are highly active to many reactions which is not the case where gold is known to be an inert material in the bulk state.[78]

For almost two decades, isolated metal clusters in the gas phase have been considered as model systems for understanding different cluster properties, in particular chemical and catalytic properties.[79] However with such models, no real applications could develop. In order to be useful in applications, clusters should be either in solution or supported on a surface. The support is a key player and in many cases will interact with the clusters changing their morphology, electronic structure and catalytic activity. Due to their interest in technological application, supported metal cluster are well-considered in many research groups all over the world.[7,29,78,80–83]

2.1 Cluster production

The cluster properties highly depend on their morphology and their size. Therefore, producing them in a reliable way is necessary. Real cluster-based catalysts are usually produced through wet chemistry techniques like impregnation or co-precipitations.[84] More conventional ways

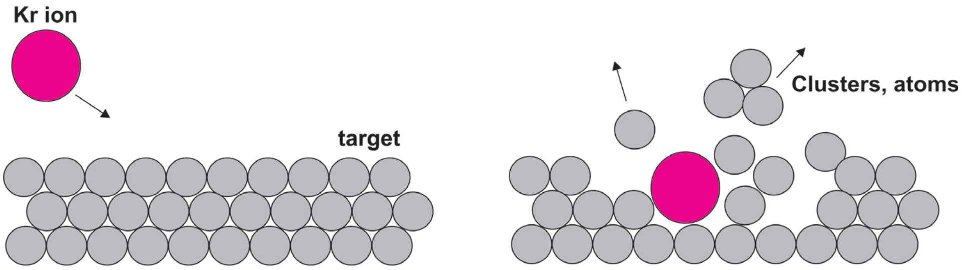

Figure 2.1 – Kr ions-target collision and clusters emission after impact.

apply lithography, of which the maximal resolution is about 5 nm, or scanning tunneling microscopy to displace atoms. The drawback of these techniques is that they give rise to broad size distributions.[85] Since in this thesis the clusters were in UHV, we will focus only on similar production.

- **Clusters formed by laser evaporation:** Basically, laser evaporation is used for materials with high melting point. It consists of evaporating a material using a high power laser. The unleashed particles form a plasma which is cooled and carried out by a noble gas injected through a pulsed valve. Charged clusters are formed during the expansion and carried to the outlet of the evaporation chamber to form a supersonic molecular beam.
- **Evaporation:** Vacuum evaporation is itself based on a thermal principle. Thus, the heating allows the material to reach its melting point and then, in a second time its vaporization point. It is based on two elementary processes, evaporation of a heated material (by joule effect, electronic bombardment or through effusion) and condensation of the evaporated material on the substrate.[86]
- **Sputtering:** Clusters produced by sputtering have been an important topic during the last decade. The principle of this method lies on removing constituents from a material target using high energetic noble gas ions accelerated by an applied potential (Fig. 2.1). This collision of incident ions results in a kinetic energy and momentum transfer to the target releasing a bunch of positively and negatively charged ions as well as neutral atoms. In most cases, the charged particles are only 10 to 20 % (80 % in the case of magnetron sputtering, depending on clusters species). The plasma sputtering produces charged and neutral metal atoms, by traveling through a region with a relatively high pressure of rare gas, the atoms cool down and condensate into metal clusters. After the cluster production, the mass selection takes place, typically, through quadrupole mass filters or time of flight filters.

These techniques usually produce clusters with wide size distribution. For many practical applications, the narrowest size distributions, up to perfect monodispersion, is required. This can be achieved through mass selecting the clusters before deposition. This method depends on the charge state and the mass range of the clusters. In the case of neutral cluster beam, one has to rely on separation through a difference in momenta or velocities. Buck and Meyer developed a method based on the scattering of a cluster beam at an intersection angle of 90°.[87] The heavier clusters are scattered into smaller angles compared to the lighter ones. Another approach applies aerodynamic focusing of an expanded beam, containing different sized particles, through a nozzle. In this case the clusters are focused and dragged using their outward radial velocities. Since the effect of radial drag is size dependent, it can be used for size separation of the clusters. In the case of charged cluster beam a quadrupoles is widely used as a filter. This later is made by 4 parallel metallic rods in which are applied a direct and an alternative potential. Only particles with a defined charge to mass ratio can go through it. The experimental setup used for this thesis uses sputtering with a Cold Reflex Discharge Ion Source (CORDIS)[88] to produce clusters and a quadrupole mass filter to perform the mass selection. Our cluster source, based on the design by Schaffner et al. *et al.*,[89] is described in the experimental section.

2.2 Cluster deposition

Let us now consider a cluster arriving on a surface. The collision time is very short, of the order of 1 ps. This time interval is too small to allow significant energy dissipation by heat diffusion across the surface. The local temperature and pressure during the impact can be extreme, leading to a modification of the cluster and/or the surface. The subsequent evolution of the cluster-surface system after impact is related to relaxation. Only then, on a time scale of up to several days, the system finds an equilibrium through thermally activated processes. For a comprehensive review of cluster deposition processes, the reader is referred to Ref.[90] The system status after impact depends on the following parameters:

- The cluster size N.
- The cohesion energy per atom of the cluster (E_{coh}^{cl}) and the surface (E_{coh}^{surf}). If this ratio is large, the cluster easily penetrates the surface and if it is small the cluster fragments without significant surface modification.
- The impact energy E_0 per atom.
- The adsorption energy of the cluster atoms on the surface.
- The angle of incidence.
- The atomic mass ratio of cluster and surface.

The variation of these parameters provides different results from a cluster gentle deposition to the destruction of the cluster and the surface. Figure 2.2 represents the more relevant deposition processes for our study:

- **Soft landing:** The cluster lands on the surface without any damage to the cluster itself or to the surface. This is an ideal case. The cluster sits on the surface maintaining its 3-D structure, without experiencing any collision-induced deformation. In practice, there is always some deformation induced by the cluster absorption energy so that the structure of the cluster is modified. An alternative way to perform softlanding conditions is to deposit clusters into a rare gas buffer layer before deposition on a support.
- **Plastic deformation:** If the cluster landing energy is close to the cohesive energy, the clusters upon impact will still intact, and is plastically deformed. This is a more realistic model.
- **Fragmentation:** The surface remains intact but the cluster decomposes into two or more constituents. To fragment, a cluster has to overcome the cohesive energy of its constituents.
- **Implantation:** The cluster impact modifies locally the surface structure creating defects which can act as pinning point for the cluster and enhance its stability.

A hard substrate shows a strong resistance to deformation and the cluster fragments upon impact.[91] At low energies, the local temperature during surface impact can evaporate small fragments and few atoms might get implanted in or reflected from the surface. At higher energies, fracture of the cluster takes place and scattered fragments can be composed by small clusters. On the contrary, a hard cluster crashing on a soft substrate can infiltrate partially or totally into the substrate without breaking itself. It can create a crater with a rim of ejected substrate atoms. It should be mentioned here that the stability of clusters on surfaces can be strongly enhanced by pinning some of its atoms into the surface.[92] The threshold for this process depends on the cluster-target combination. By further increasing the cluster kinetic energy, the substrate atoms can even be pushed out and leave the surface. This phenomenon could give rise to reactive sputtering in which the projectile and the target atoms form an alloy.

2.3 Atoms and clusters on the surface

It is crucial to know what is the becoming of a cluster as it lands on the substrate. Instead of remaining stationary and preserving its free structure after landing, it might fragment, or become embedded in the surface. The presence of the surface will, likely, cause perturbation to the free cluster structure. A further possibility is the diffusion of clusters, so that they may aggregate together to form islands.[93] Driven by the thermal energy, the adsorbed clusters and adatoms on the surface find their equilibrium through diffusion and aggregation processes. Figure 2.3 resumes the typical atom and cluster movements. An atom meets another, forming a dimer which can evolve in three ways: either, it dissociates, remains stationary or diffuses. In the latter two cases, the dimer increases by capturing other atoms or clusters. Atoms may diffuse along or across steps on the surface, they can exchange their position with one of the atoms of the support or they can migrate on a cluster. During surface diffusion, the

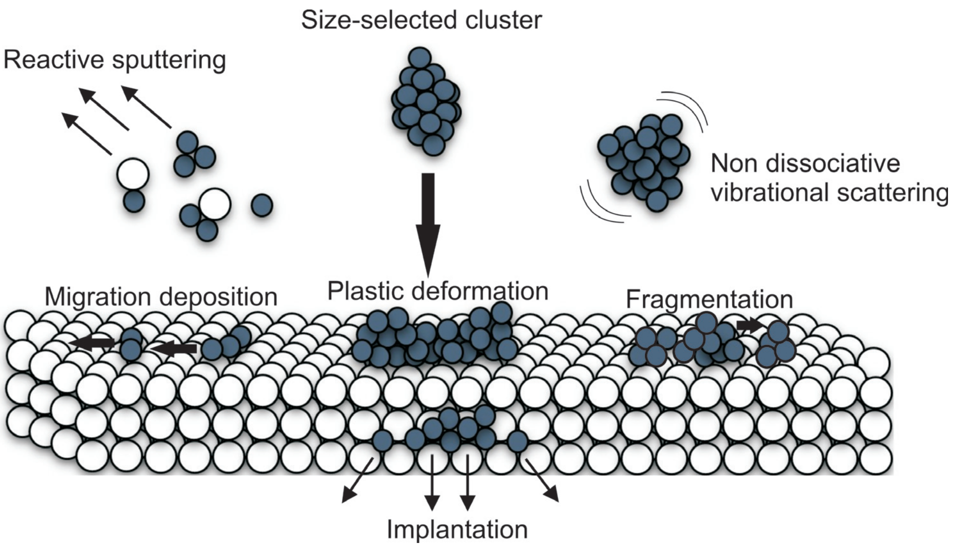

Figure 2.2 – Possible outcomes of the cluster deposition on a surface depending on the deposition parameters and on the properties of the cluster and the support.

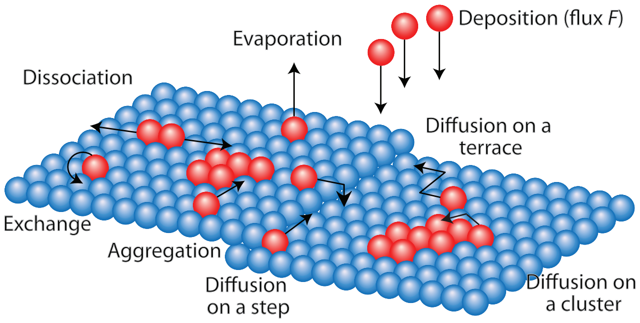

Figure 2.3 – Evolution of atoms and clusters (red balls) on a surface (blue balls). Adapted from Ref.[4]

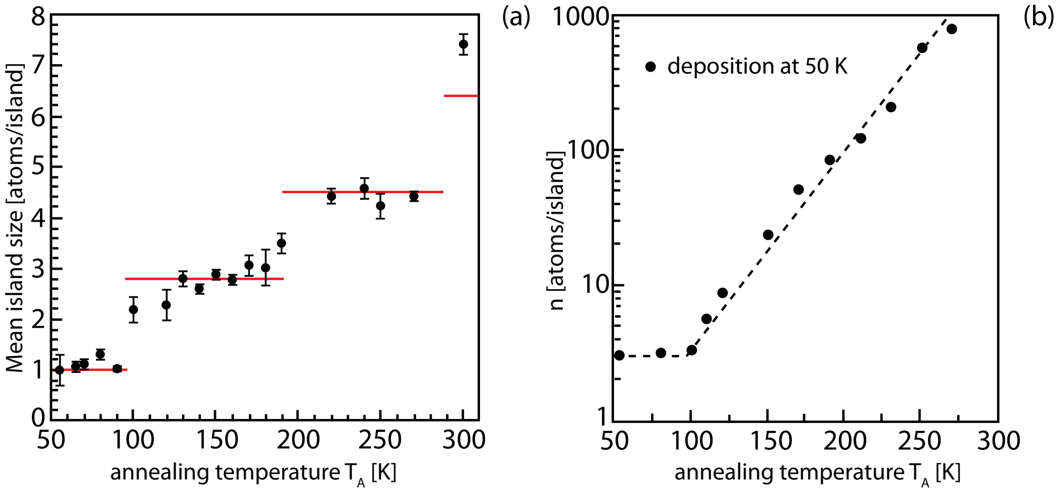

Figure 2.4 – (a) Average cluster size versus annealing temperature for a system that grows in following cluster diffusion (Co/Pt(111))[5] and (b) a system following Ostwald ripening. Adapted from Ref.[6]

clusters could cross surface defects, that is to say an incomplete coordinated atomic area in which adsorption of atoms are energetically favorable. These defects are stabilizer centers for diffusive species. The cluster growth can follow two different path:

- **Ostwald ripening:** This corresponds to the case when larger clusters grow at the expense of smaller ones.[94,95] Large clusters, with their lower surface to volume ratio, results in a lower energy state (have a lower surface energy). As the system evolves, to lower its overall energy, adatoms on the surface of a small cluster will tend to detach and diffuse, then attach to the surface of larger cluster. Consequently, the number of smaller clusters continues to shrink, while larger clusters continue to grow. Suppression of Ostwald ripening through elimination of its main driving force via size-selection could be conceivable by designing model systems with precise atom-by-atom particle size control.[96]

- **Cluster diffusion:** It corresponds to the case of diffusing of entire clusters that merge when they meet to form new bigger clusters. The result of this process is a stepwise growth of the cluster size.

It is possible to distinguish the two different processes by studying the particle-size distribution (PDS) with temperature. In the case of Ostwald ripening, the PSD shows an analogous shape with a tail in the small-diameter regime, which results from the continuous supply of small clusters (Fig. 2.4b). The total cluster coverage remains constant and the maximum of the PSD does not shift significantly.[33] For the diffusive mechanism or what is called Smoluchowski mechanism, the PSD shape corresponds to a log-normal distribution function, tailed towards higher particle sizes. The smaller particles tend to shrink and disappear, this leads to a short cutoff of the PSD at lower particle diameters. As a result, the total cluster coverage decreases immediately. As it is shown in Figure 2.4a, a system which grows in following cluster diffusion (0.1 ML of Co/Pt(111))[5] presents a stepped evolution of the mean cluster size as a function of the annealing temperature.

In the case of a multilayer system or when a monolayer is used as a second stage on top of a support, supported small clusters, often, undergo a process named intercalation. Driven by temperature, detaching adatoms from clusters cross under the top support layer and stacks below. For example, it was found that Mn clusters deposited at room temperature on graphene and h-BN supported on Rh(111) can intercalate under annealing.[97] It is believed that the gates for cluster intercalations are area of high density of surface defects. Intercalation can lead to possible controlling of size and arrangement of intercalated clusters as well as the properties of the surface. Inserting foreign atoms or molecules between hexagonal two-dimensional sheets of graphite, can be used to tune the system properties such as the interlayer spacing and charge transfer of graphite.[98] For example in the case of graphene on Ni(111), Cs intercalation weakens the strong interaction between graphene and substrate which leads to ideal free standing graphene.[99] In the case of cobalt-graphene/Ir(111), Co intercalation enhances the out-of-plane magnetic anisotropy at the graphene/Co interface.[100]

2.4 Equilibrium structure of the clusters

At the thermodynamic equilibrium, all diffusion process mentioned above are conducted at equivalent rates and in opposite directions. So there is, macroscopically, no growth or evolution. the reorganization of nanostructures can be activated again by annealing the system at certain temperature in order to provide sufficient energy and allow the sample to evolve freely. After cooling, the resulting state is the most stable for this annealing temperature and depends only on the cluster surface-energy ($\gamma_{Cluster}$), the support surface-energy ($\gamma_{Support}$) and the cluster-surface interaction energy($\gamma_{Interaction}$). The cluster wetting behavior of the surface, according to Bauer, would define different growth modes.

These three energies define the parameter $\Delta\gamma = \gamma_{Cluster} - \gamma_{Support} + \gamma_{Interaction}$. The sign of $\Delta\gamma$ allows distinguishing between different growth regimes[101,102]:

- **$\Delta\gamma < 0$:** The results of surface energy is favorable for wetting. The deposited particles organize themselves so as to form two-dimensional layers. Growth, layer after layer, is known as Franck-van der Merwe type. This is the case generally met during the deposition of a metal on a metal support in which the difference in the lattice parameters (or lattice mismatch) is low, such as the case of Ag/Pt, for example.

- **$\Delta\gamma > 0$:** The surface free energy of the deposited material prevails and one should sees scattered dimensional nanostructures. This type of growth is typical for a metal over an oxide and is named Volmer-Weber. Cu/TiO$_2$ is an example of this type of growth.

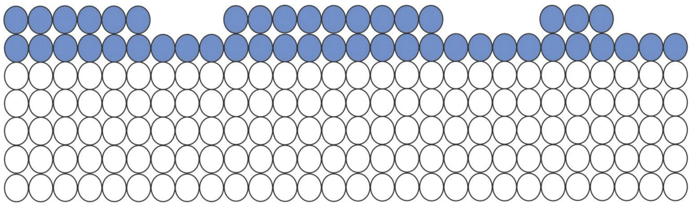

2-D or layer-by-layer growth, also known as Frank-va DerMerwe mode

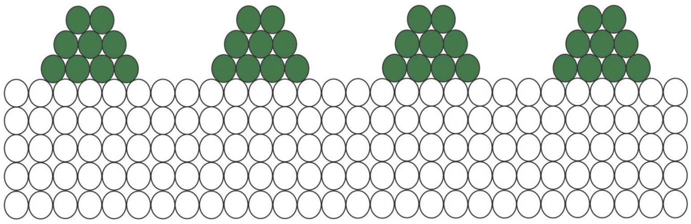

3-D or island growth mode, also known as Volmer-Weber mode

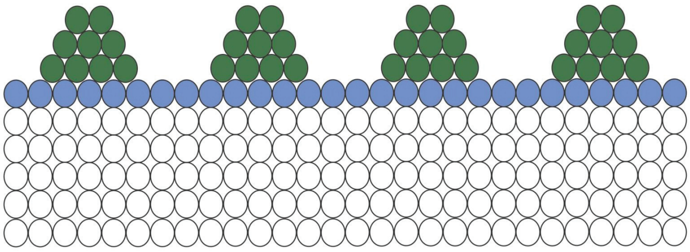

a mixed mode, also known as the Stranski-Krastanov mode

Figure 2.5 – Representation of the growth regimes: (a) in the Frank-Van der Merwe growth, the deposited atoms wet the surface and the growth takes place layer by layer. (b) in the Volmer-Weber growth, three-dimensional clusters are formed since the beginning. (c) in the Stranky-Krastanov growth, the initial two-dimensional growth is followed by the formation of three-dimensional islands.

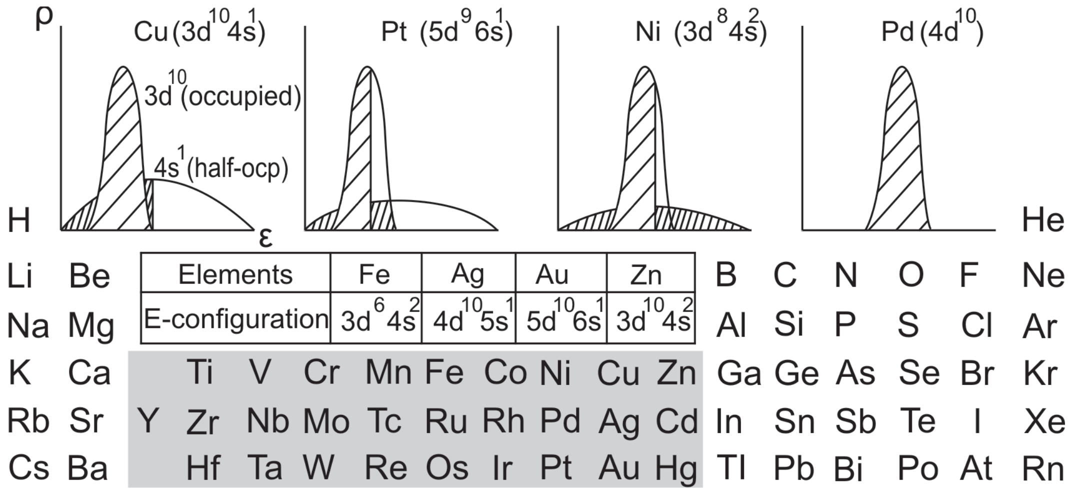

Figure 2.6 – Periodic table with the transition metals highlighted and electron density ρ distribution for d and s orbitals for Cu, Pt, Ni, Pd.

- $\Delta\gamma \approx$ **0:** A transition from a 2D growth for the first 3D layers for a certain coverage can occur. This transition is due to the relaxation of the network induced by the difference in the lattice parameters of the two materials. We are dealing with a Krastanov-Stransky type of growth that we encounter typically in the case of a metal deposited on another metal whose lattice mismatch is important, for example in the system of Ag/Pd(110).

A representation of the three regimes is shown in Figure 2.5.

2.5 Transition metals clusters

Transition metals elements share a range of considerable properties such as high melting points, hardness and good electrical and heat conduction. The transition elements may be splitted with respect to their electronic structures into three main transition series. The first main series begins with scandium and ends with zinc. The second series starts with yttrium to cadmium and the third one ranges from lanthanum to mercury. These three main transition series envelopes 30 elements called the d-block transition elements. They are known to possess, or can give rise to, electronic configuration containing incomplete d subshells which has an important role in the formation of chemical bonds (especially surface bonds). It should be noted that some of them, such as Cu, Ag and Au, are noble metals with a completely filled d sub-layer which give them quite different properties with respect to the other elements. The specificity of d-orbitals resides on the long range interaction, so they yield small barrier for adsorption (compared with s and p orbitals) and due to this, the activation energy for a catalytic process decreases drastically, promoting such metals to be good candidates for the creation of highly catalytic systems (see Figure 2.6).

The partially filled d-orbitals catalysts exhibits properties of special importance because of

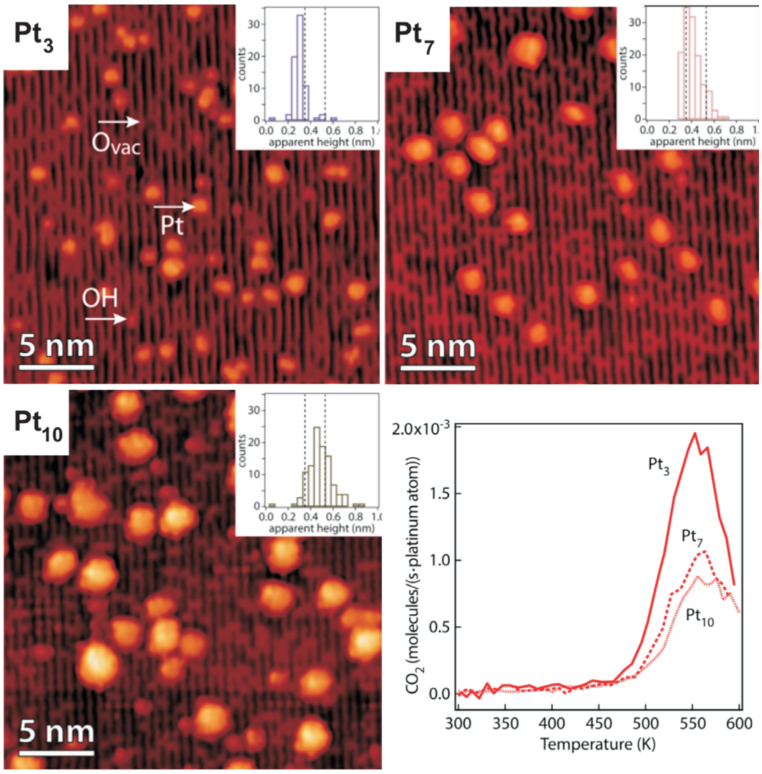

Figure 2.7 – STM images of Pt_3, Pt_7 and Pt_{10} as deposited on TiO_2(110)-(1×1) and their corresponding CO_2 production. The STM insets represent the cluster height distributions. Adapted from Ref.[7]

their tendency to form coordination compounds, ability to form multiple chemical bonds as well as their ability to accommodate multiple accessible oxidation states. They are very important in science, and on the industrial scene. Pd as a catalyst is widely used in chemical processes such as oil refining and exhaust gas treatment. It is used for CO and CH_4 oxidation, and recently Pd clusters are found to exhibit high activity and selectivity towards hydrogenation of Nitroarenes.[103] Ru promoted catalyst was introduced as an alternative to iron for ammonia synthesis at reduced pressure and reaction temperature.[104] Some reactions of complex molecule synthesis are only compatible with heavy transition metals. Ru is found to catalyze, using hydrogen exchange, new C-C links formation in alcohols.[105] Au is used in various catalytic processes such as, CO and H_2 oxidation, NO reduction and water-gas shift reaction. Selective hydrogenation of carbonyl groups can also be hydrogenated to alcohols using copper catalysts.

2.6 Platinum clusters

Platinum based catalysts are critical and essential to many industrial chemical processes. Nevertheless their efficiency per atom is extremely low, because only the exposed atoms contribute to the reaction. Small Pt clusters provide high surface area to volume ratio, and a large number of highly active low coordination sites. It was also demonstrated that small platinum clusters perform the oxidative dehydrogenation of propane 40 to 100 times more efficiently than traditionally platinum and vanadium catalysts.[106] The properties of very small size selected clusters have been studied both in the gas phase and supported state. There have been significant theoretical efforts to investigate the structures of isolated platinum clusters, but so far these are inconclusive, predicting different low-energy structures.[107,108] DFT shows that up to Pt_5, the cluster forges in the planar structure.[109] In disagreement with DFT prediction, experimental determination of the cluster structure in the gas phase shows that Pt_4 is three dimensional.[107] Catalytic activity of the unsupported platinum cluster has also been studied, showing that Pt_n^+ (n=3-5) are effective catalysts for CO oxidation at room temperature.[110] Size selected Pt clusters have been studied with STM on different supports. Clusters supported on TiO_2 with less than seven atoms appear planar on the surface. Pt_8 and Pt_9 show two and three-dimensional isomers, while bigger clusters are three dimensional.[111] Subnanometer platinum clusters are highly active as catalysts due to large fraction of undercoordinated surface atoms. However, this makes them very sensitive to ripening. Figure 2.7 shows STM images of small Pt_n(n=3,7,10) clusters supported on TiO_2, where a size effect can be demonstrated. In these cases, the catalytic activity decreases monotonically with increasing the initial cluster size. The clusters are found stable in UHV up to 600 K, but only up to 430 K when reaction gas is adsorbed on them.[7] Pt_n (n less than 10) supported on graphene/Ir(111) are unstable upon CO adsorption and they grow in size through Smoluchwski ripening, while larger clusters remained immobile, but became more three dimensional.

2.7 Iron clusters

Iron is a ferromagnetic element and it belongs to a small group of ferromagnetic atoms, at room temperature, which consists of Fe, Co and Ni. In transition metal, only Fe, Co and Ni are ferromagnetic at room temperature However, it is also highly active to many catalytic applications in many industrial processes such as ammonia (the Haber-Bosch process) and paraffin (the Fischer-Tropsch process) synthesis. The catalytic activity of free Fe clusters has been studied and was found to exhibit high activity in the reaction of ethylene to benzene[20] and the oxidation of CO in the gas phase.[112] Research on supported iron catalysts is of great interest for many applications, especially, for ammonia synthesis. Theoretical calculation performed on Fe_7 nanoclusters supported on MgO, shows the possibility of a low-temperature synthesis of ammonia if the Fe nanoclusters are passivated with nitrogen.[8] It was found that N_2 hydrogenation starts only after the adsorption of 10 H atoms to the pre-nitrogenated Fe cluster as indicated in Figure 2.8. Industrial nano-iron catalyst supported on cerium oxide has been produced allowing ammonia synthesis at reduced pressures and temperatures where about 50 % of energy could be saved against current methods.[113] Part of the work of this thesis is dedicated to the catalytic aspect of iron clusters supported on corrugated h-BN monolayer whose structure and properties are discussed in the following section.

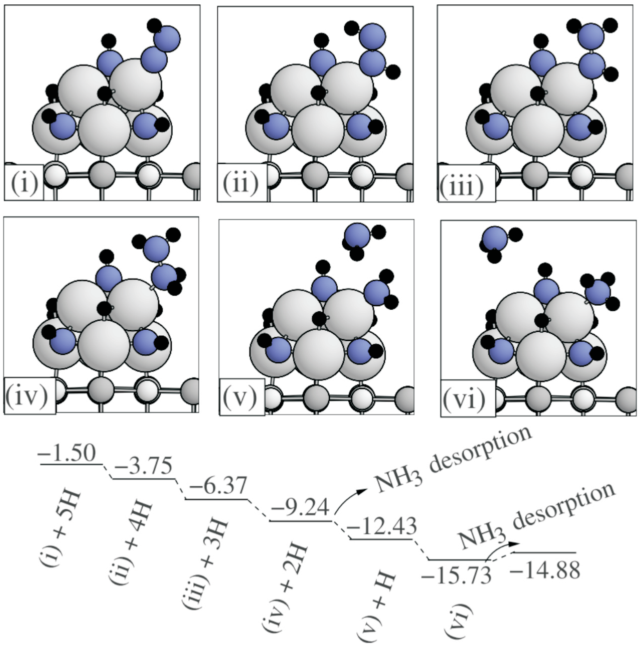

Figure 2.8 – Side views of the intermediate states during hydrogenation of the N_2 molecule at the nitrogenated Fe_7/MgO cluster and the corresponding potential-energy profile. The indicated amounts of H correspond to atoms in the gas phase. All energies are in eV. Color code : grey (Fe), blue (N) and black (H). Adapted from Ref.[8]

3 Hexagonal boron nitride: h-BN/Rh(111)

3.1 Structure

The investigation of catalytic reactivity, stability and the underlying chemical or physical processes of small particles and clusters needs a proper choice of the substrate and the substrate preparation. Recent studies have shown that two-dimensional nanomaterials can serve as excellent candidates for the support of metal nanoparticles.[29] Among these supports, two-dimensional hexagonal boron nitride (h-BN) (Fig. 3.1) which possesses similar planner structure (single layer of sp^2 hybridized h-BN) like graphene but with different properties, is getting intensive attention due to its capacity for self-assembling of atoms and molecules[114,115] and its interesting properties, such as exceptional mechanical and thermal behaviors, and chemical stability.[116] The difference in electronegativity of B and N, allows h-BN to be more ionic, making its interaction and charge transfer with deposited transition metal (TM) atoms to be different from those on graphene beside various defects, such as vacancies and boundaries, that exist in the as synthesized h-BN single layers and are ready to anchor nanoparticles and change the electronic properties of adsorbed atoms, molecules and clusters.[115]

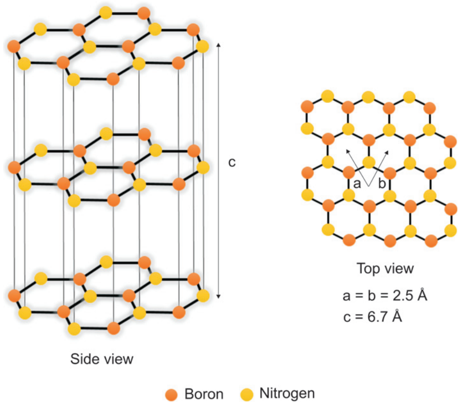

Figure 3.1 – Molecular models for boron nitride as viewed from the side and the top.

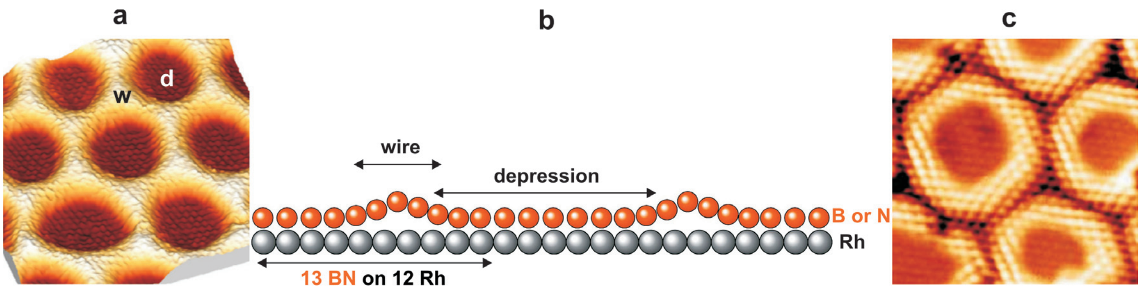

Figure 3.2 – (a) Monolayer model for h-BN moiré showing depressions (d) and wires (w). (b) cross-section of h-BN on rhodium showing depression and wire regions. The unit cell of the moiré pattern contains 13 × 13 unit cells of the h-BN lattice, fitting onto 12 × 12 unit cells of the underlying Rh(111) surface. (c) BN moiré observed by STM. The center of each ring corresponds to the center of the depressions. Adapted from Ref.[9,10]

The interest in single layer h-BN has mainly been driven by its ability to form self-assembled nanostructures on lattice mismatched substrates, in particular, on Rh(111) and Ru(111), which makes it a promising candidate for creating nanostructured templates for a variety of applications. In 2004, Corso et al. reported curious epitaxial BN which adopts a highly regular superstructure that has been called ‘nanomesh’ as observed under scanning tunneling microscopy (STM).[117] Unlike Chemical Vapor Deposition (CVD) preparations of single layer BNs which were carried out in low-pressure chambers with lattice-matched Cu or Ni substrates,[118] the BN nanomeshes were grown from a borazine ($B_3N_3H_6$) precursor in an UHV chamber on a hot (800 °C) Rh(111) surface. The original recipe for preparing the nanomeshes consisted of heating a Rh(111) surface at 1050 K under low pressure of pure borazine gas. Rh(111) has a lattice mismatch of about 7 % with h-BN, leading to arrays with 2 nm diameter depressions (pore-like structures) and an ordered periodicity of 3.2 nm as seen in STM images (Fig. 3.2). It has been shown that the h-BN is a coincidence of 13 h-BN units per 12 Rh substrate units with a corrugated monolayer (Fig. 3.2b). The h-BN on Rh(111) consists essentially of a regular hexagonal structure of 2 nm wide depressions in the h-BN layer and the distance between 2 depression centers is 3.2 nm.[119] The lattice constant of 3.2 nm is determined by the mismatch between the boron nitride and Rh and the depressions are in fact shallow regions of about 2 nm diameter that strongly interact with the substrate, thus with a closer distance, while the surrounding areas (the wires) are weakly bound regions with a larger h-BN distance to the substrate. This happens because the nanosheet-metal interactions are such that N atoms are attracted to the metal atoms while the B ones are repelled from them. The hexagonal arranged high and low regions have a height difference of 0.55 Å. The h-BN single layer, in fact, does not exhibit holes. So, it is sometimes, referred to as a moiré pattern and not as a nanomesh.[120] The existence of a lattice mismatch between the BN layer and the substrate, leads to periodic areas where N atoms are sitting right above Rh atoms and thus have the most interaction strength due to the hybridization of the N lone pair orbital with the Rh d-states, while there are offsets at other regions where N atoms are situated on the threefold Rh hollow sites.[121]

The corrugation pattern, shown in Figure 3.3a, represents the modulation of the B-N bond

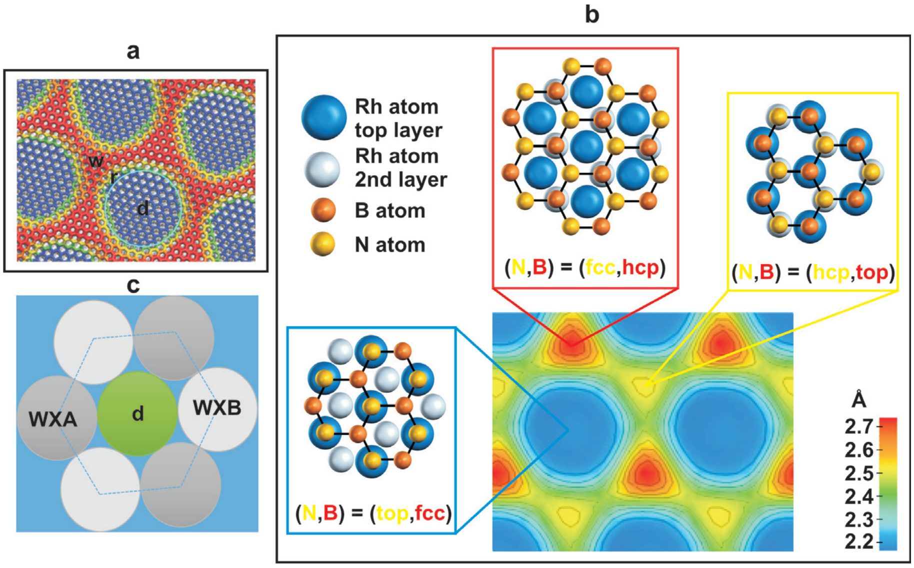

Figure 3.3 – (a) The h-BN/Rh(111) moiré and the corrugation of the h-BN layer. The color code of the h-BN monolayer reflects the height of the B and N atoms with respect to the substrate. The blue areas correspond to the depression regions (pores), the red to the wire regions, and the atoms colored with yellow and green form the so-called "rim". (b) The N height relative to the underlying substrate. The exact arrangement of Rh, N and B atoms is given for three different areas (blue: depression, yellow-red: wires). (c) WXA is where (B-hcp, N-fcc), and it is slightly higher (0.2 Å) over Rh than WXB where (B-top, N-hcp).

length which also stands for the modulation of the electronic properties of the monolayer. This should contributes to the spatial modulation of the electrostatic potential above the moiré which is responsible for trapping of atoms and molecules.[122] The h-BN moiré has two different wire crossing sites characterized by different registry to the substrate (Fig. 3.3b and c). One site (WXA) with boron on top of a Rh atom and nitrogen on hcp hollow sites, *i.e.*, (N-hcp, B-top), and another one (WXB) where boron stays at hcp hollow sites and nitrogen at fcc sites, namely (N-fcc, B-hcp). These two sites are weakly bound to Rh. The strongest bound to Rh is where (N-top, B-fcc), *i.e.*, in the depression region.

Flat monolayer hexagonal boron nitride (h-BN) which is insulating and stable against high temperatures and reactive gases[123] can be deposited by chemical vapor deposition (CVD) on transition metal surfaces, such as Pt, Pd, Cu (3d) and Ni (3d), using either ammonia borane (H_3B-NH_3) or borazine ($B_3N_3H_6$). On Rh(111) and Ru(0001) surfaces, however, a corrugated unique h-BN layer[124] is formed. For h-BN deposition on Rh(111), a partial pressure of borazine (Fig. 3.4a) is introduced into the UHV system and exposed to the hot Rh surface. The interaction with the Rh decomposes the borazine (Fig. 3.4b) leaving fully dehydrogenated hexagonal molecules that diffuse about the surface and combine to saturate their open bonds. The tiling of many molecules finally results in a perfect two dimensional crystal lattice of hexagonal boron nitride, as is sketched in Figure 3.4c,d.

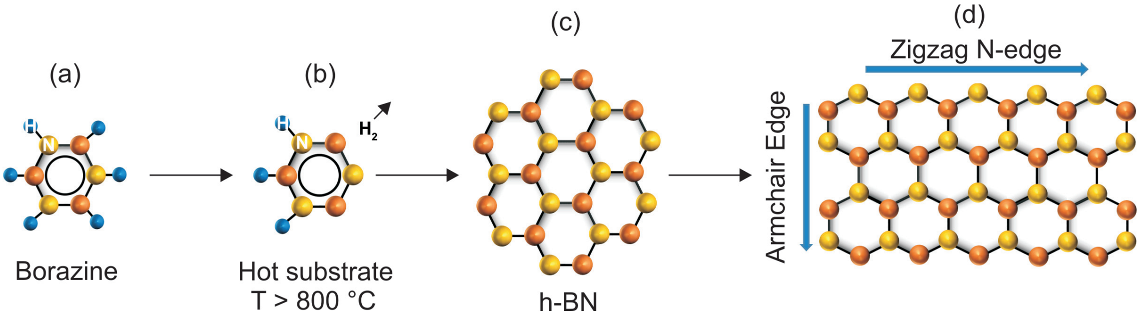

Figure 3.4 – h-BN monolayer deposition from borazine. (a) the borazine molecule is isostructural to benzene. (b) the catalytic interaction with the hot sample surface removes hydrogen from the molecule. (c) periodic tiling of dehydrogenated borazine that forms the layer of hexagonal boron nitride. (d) a monolayer BN with a honeycomb structure made up of ring units of borazine. The B–N bonds, covalent in nature but with ionic characteristics, are 1.45 Å in length. The distance between the centers of neighboring borazine rings is 2.50 Å. The edge of a monolayer could be either zigzag (B- or N-edged) or armchair (BN pair-edged).

Due to epitaxial stress resulting from lattice mismatch between the substrate and the sp^2 layer, a corrugated nanosheet could be formed if the interaction between the substrate and the deposited layer is sufficiently strong. Because of the misfit between h-BN and Rh, and the preference of nitrogen to bond on top of Rh, the 13 × 13 BN units divide into bonding areas, the "depressions" where the h-BN wets the substrate, and into "wires" where the h-BN has a pure van der Waals bonding to the substrate. However, if the mismatch is small, a single layer h-BN on the metal surface remains flat or only slightly deformed, providing more homogeneous adsorption on the surface. It should be mentioned that a large lattice mismatch does not necessarily lead to strong corrugation. In fact, the corrugation is more dependent on the monolayer-substrate interaction strength. For example, Pt(111) has a larger lattice mismatch with h-BN (10.8 %) than Rh(111) (7.6 %), but little to no corrugation was found on the grown monolayer on Pt(111). The Rh(111) substrate is among ones that interact strongly with h-BN monolayers, resulting in nanosheets with periodic corrugation.[121] The h-BN on Rh(111)[117] and on Ru(0001)[125] is under consideration for use as a template for self-assembly or self-organization processes and supporting various nanoparticles and clusters such as Pt and Au as well as for trapping atoms and molecules.[126] Therefore, applications in catalysis could be easily realized because the depression zones in the moiré could serve as traps to aid in nanotemplating for subsequent arrangement of metals or molecules into arrays of nanoparticles.[119,127] Figure 3.5 shows a schematic view of a single layer h-BN on metallic substrate, with adsorbed molecules. If the single layer is flat (Fig. 3.5a), molecules adsorb homogeneously over the surface, while in corrugated layer systems (Fig. 3.5b), molecules will be trapped in the depression zones. The h-BN coating has been demonstrated to remain intact under ambient conditions and at high temperatures thus protecting the underlying substrate against oxidation.

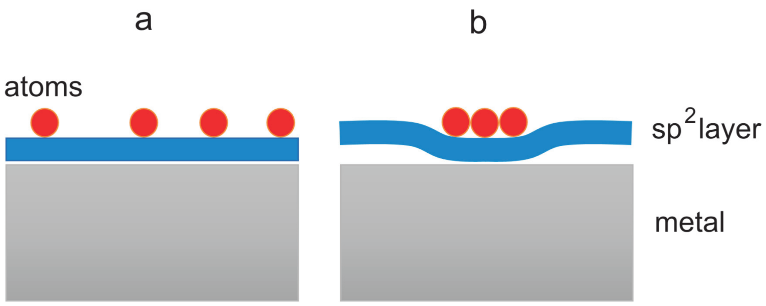

Figure 3.5 – Schematic side view of a flat (a) and corrugated (b) single layer on top of a metal.

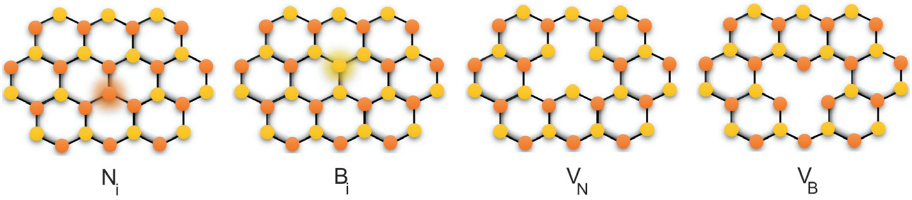

Figure 3.6 – Schematic presentation of the h-BN intrinsic defects: nitrogen impurity (N_i), boron impurity (B_i), nitrogen vacancy (V_N), and boron vacancy (V_B). Color code: Boron in yelow and nitrogen atoms in red.

3.2 Defects in h-BN

Defects play a key role in determining the properties and technological applications of nanoscale materials. Since 2D BN layers are promising for many interesting application, it is crucial to understand the nature and behavior of its intrinsic defects. Four types of point defects, such as nitrogen vacancy (V_N), nitrogen impurity (N_i), boron vacancy (V_B) and boron impurity (B_i), can form in h-BN single layer (Fig. 3.6). The N_i and B_i impurity defects have low formation energies, comparable to those of the vacancies V_N and V_B. So, N_i was found to be the most stable defect in h-BN under N-rich conditions followed by the nitrogen vacancy.[128]

Formation and aggregation of vacancy defects on h-BN can be realized by ion bombardment which sputters out boron and nitrogen atoms, leaving vacancy defects within the h-BN layer. The B and N vacancies formation and their stability and mobility is of great importance for h-BN application as active template and its functionalization processes. These vacancies can be annealed at elevated temperatures due to their mobility. Nevertheless, vacancies generated in the depressions may not leave during annealing due to the strong interaction of the pore regions which allows for an increased stabilization of vacancies in the depression zones. It has been shown that N vacancies which were found to act as donors are less stable than B vacancies and STM experiments have revealed an accumulation of defects at the rim and the wire of h-BN. Furthermore, BN vacancy pairs were found to be more stable than the corresponding single vacancies and that they have, also, a tendency to accumulate towards the rim.[122] Another type of defects that is worth to mention is defect lines that result from merging of two h-BN domains with different registry to the substrate which have been observed in h-BN/Ni(111),*i.e.*; where the stacking of the B atoms with respect to the substrate changes from fcc to hcp while the N atoms are always at on-top sites.[129,130]

3.3 Electronic properties and support effects

Strong correlation between the electronic structure and the catalytic activity has been revealed in catalysis. So, controlling the active site electronic structure is crucial for creating suitable chemical bonding with the reactants (not too weak and not too strong), which ensures both a good electron transfer between the catalysts and the reactants and a facile products-releasing process.[131] Contrary to graphene which has semi metallic properties with a zero band gap, the h-BN which possesses partially ionic B-N bonds, is an insulator with a wide direct band gap of 5-6 eV. Like graphene, BN forms a sp^2 honeycomb network with strong σ in plane bonds and soft π bonds to the substrate and the adsorbates. However, unlike graphene where the π derived electrons are delocalized, the corresponding electrons in h-BN are bond to the nitrogen atom. On the other hand, the electronic properties of low-dimensional h-BN systems differ considerably from those of bulk h-BN. The band gap in single layer h-BN can be considerably reduced by vacancy and impurity defects[132] or by decorating the BN sheet with hydrogen atoms.[133] Support effects can significantly modulate the band gap in two-dimensional (2D) nanostructures. It was found that monolayer h-BN is weakly bound to the metal surfaces and remains an insulator.[123] However, it has been shown that some mixing of the π h-BN and d metal bands can occur[134] and strong orbital hybridization between the Ni 3d and h-BN π states has been demonstrated, indicating a strong interaction between h-BN and the Ni(111) substrate.[135] Moreover, it was reported that monolayer h-BN deposited on a transition-metal support such as Ni(111) can be considered as metallic or "partially" metallic and that a monolayer of h-BN on the Ni(111) surface can exhibit catalytic activity where it is shown that mixing of the Ni dz^2 orbitals with the N pz and B pz orbitals of monolayer h-BN considerably modifies the adsorption energies of simple molecules on h-BN/Ni(111) and functionalizes the inert h-BN. However, the results of experimental and theoretical studies on the electronic properties of monolayer h-BN adsorbed on transition-metal surfaces are still very controversial.[136] The h-BN has a peculiar electronic structure that is reflected in the core level binding energies of the elements, which are sensitive to the position of the atoms. Ultraviolet photoelectron spectroscopy (UPS) of h-BN on Rh revealed a splitting of the σ-band, indicating two different types of bonds between the overlayer and the Rh.[137] A splitting of the N 1s core level into two components also has been observed by X-ray photoelectron spectroscopy (XPS) and is ascribed to the h-BN layer corrugation.[138] Also, it has been observed that the local work function above h-BN changes following the corrugation of the BN overlayer. Few angstroms above the atoms forming the depression of h-BN, the work function is about 310 meV lower than above the atoms of the wire.[32] Therefore, the different registries of h-BN on Rh should be responsible for the modulation of the electronic properties, which is well recognized by the modulation in brightness of the simulated STM topography. This modulation is expected to have an influence on the behavior of adsorbed molecules. In transition metals (TMs), the d-electrons are valence electrons often engaged in chemical reactions. The work function of a surface system changes when adsorbates with unsaturated π bonds, such as -B=N- in h-BN and -C=C- in graphene, interact with the metal surface dipoles, which causes electron donation from the highest occupied π-orbitals to the metal and back donation from the metal d states to the lowest unoccupied π^*-orbitals. This is called adsorption induced charge transfer at the interface.[40] The measurement of work function of a surface system can therefore shed light on the charge transfer and consequently, on the details of the interfacial interaction. Since the interaction of h-BN with TM substrates is determined mainly by the orbital hybridization between the TM d states and the states of h-BN, the strength of chemical bonding at the h-BN/TM interfaces must depend on the character of the substrate d states energy, occupancy, and angular and radial distributions, varying from very weak to rather strong chemisorptions. This is why stronger h-BN chemisorptions on Rh(111) results in a much stronger corrugation of the adsorbed monolayer due to larger difference in energy between favorable and unfavorable adsorption sites within the interfacial super cell.[139]

3.4 Sticking and intercalation

At the nanoscale, textured surfaces play a crucial role in the adsorption of atoms and molecules and their equilibrium with the gas phase and new applications are expected if the texture can be switched between different states.[138] The binding energy of adsorbed species on h-BN should be dependent on its work function which would be related to both the type of configuration (nitrogen- or boron-substituted) and the site of adsorption (depression or wire). Thus it is expected that the binding energy will be predominantly governed by the nature of the moiré only and the substrate could have only a small effect on the adsorbed binding energy.[140] Recently, intercalation processes of Ar and Rb, forming the so-called 'nanotent' structures, have been reported after irradiating h-BN with low energy ions.[141] It has been shown that impacting Ar ions with low energy close to the penetration threshold (in the order of 100 eV) can be intercalated and trapped between the metal and h-BN by breaking some BN bonds and penetrating the over layer. The resulting defective structure relaxes quickly, while Ar moves to a stable site where a protrusion appears on top of the characteristic super honeycomb lattice of h-BN. Ar atoms do not rest in depression-sites of h-BN, but are situated beneath the wires, particularly where wires cross (Fig. 3.7).[11,142]

The intercalation beneath h-BN is not limited to noble gas atoms. The intercalation of Rb^+ ions with 100 eV kinetic energy in h-BN/Rh(111) has been demonstrated[12] as shown in Figure. 3.8.

Upon intercalation, the structural properties and electronic structure of the overlayer can be altered. The adsorbate-substrate interaction may have some impact on the overlayer such as weakening of the interatomic bonds and altering of the overlayer surface structure. In the case of metal adatoms, adsorption or surface alloying may form at the topmost layer as shown in Figure. 3.9a. For metal substrate covered with an overlayer, energetic or reactive adatoms can

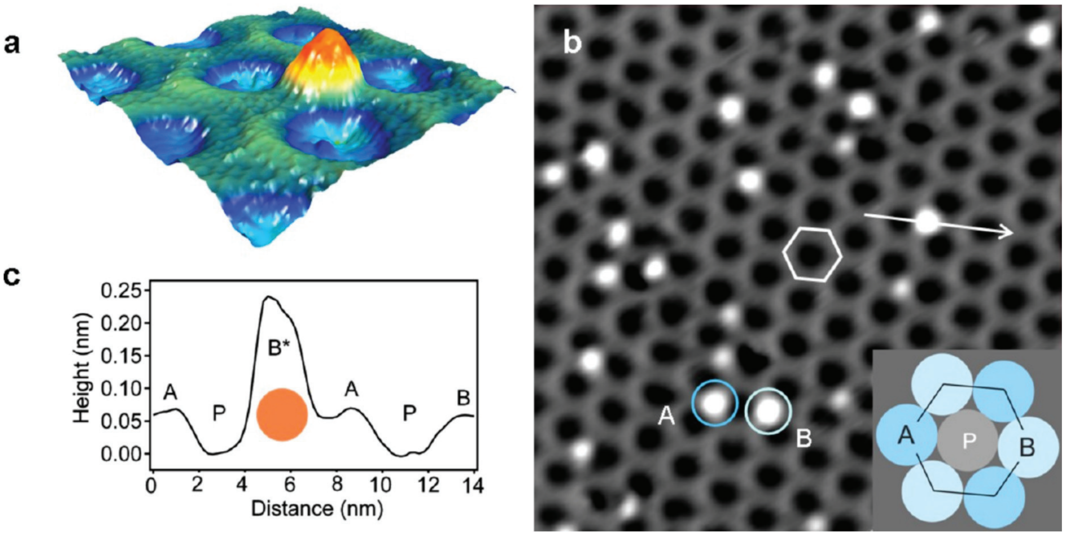

Figure 3.7 – STM data of ion-implanted Ar beneath h-BN/Rh(111) at room temperture. (a) 3D STM image of one Ar nanotent (red-yellow peak). The green and blue regions represent wires and depressions beneath the moiré, respectively. (b) STM image (38 x 38 nm^2) showing the selective Ar implantation: Ar locates at two distinct sites beneath h-BN wire crossings, (labelled as A (dark blue circle) and B (light blue circle)), but not in the depressions (P). The bright protrusions are Ar clusters. The hexagon represents the honeycomb super cell, also shown in the right-bottom inset. U_t = -1.10 V, I_t = 0.10 nA. (c) cross-sectional profile along the white line in panel b. A pore, an occupied B site, an empty A site and another depression (pore-like) are indicated. Adapted from Ref.[11]

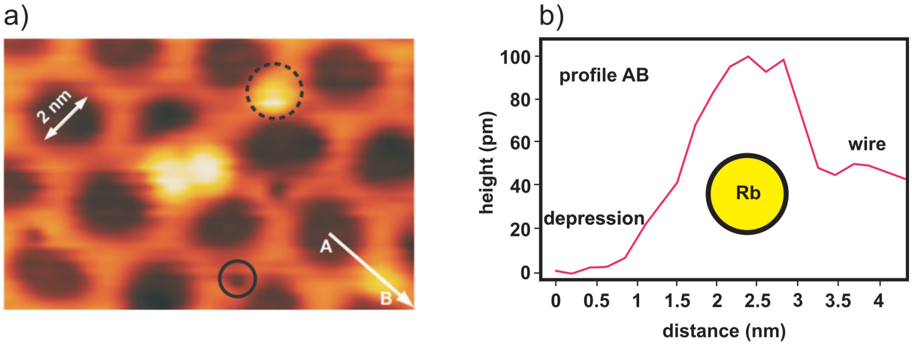

Figure 3.8 – (a) STM (13.5 nm × 9 nm) of Rb atoms implanted beneath h-BN/Rh(111), V_t = 2.0 V, I_t = 0.1, nA and T = 34 K. The Rb atoms have a tendency to stay at wire intersection sites (dashed circle). Vacancy defects generated by the penetration of the h-BN by the ions can, also, be observed (solid circle). (b) Height Profile along the arrow AB in image (a). Adapted from Ref.[12]

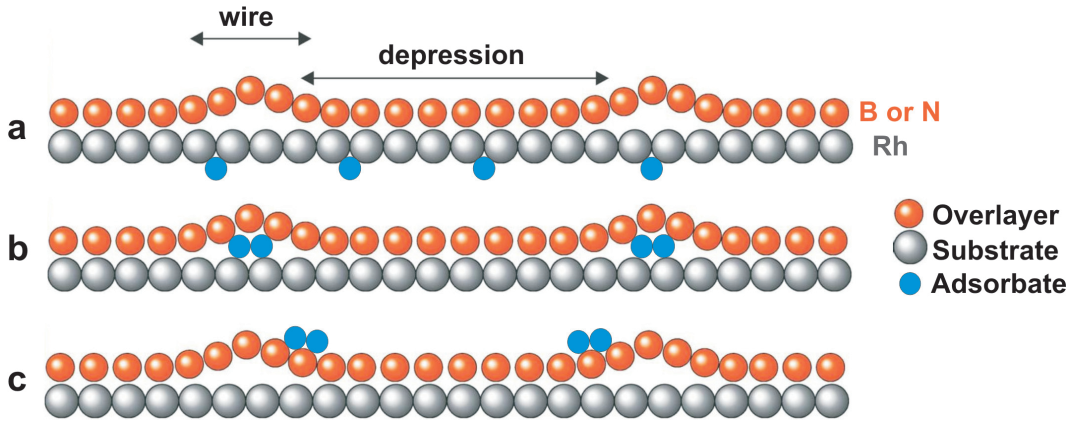

Figure 3.9 – Schematics of adsorbate-substrate interactions, (a) substrate penetration at high kinetic energy, (b) intercalation at medium kinetic energy, and (c) adsorption at low kinetic energy.

still reach the underlying metal surface by intercalation via the defected sites and the edges of the overlayer. Depending on kinetic energy and reactivity, these adatoms may gradually penetrate further into the metal substrate or simply reside between the overlayer and the metal surface, as depicted in Figure. 3.9b.[143]

Metal atoms with low ionization potential such as Cs, K and Na can be intercalated easily at relatively low temperature while the intercalation of atoms with high ionization potential such as Pt, Ni and Mo can only be induced chemically or thermally (at elevated temperature)[144] and metal adsorbates with very high surface free energy such as Co and Pt tend to agglomerate into large clusters to lower their surface energy. The immobilization of single atoms beneath an ultimately thin sp^2 hybridized layer, in so called “nanotents” is an interesting way to functionalize a surface. For atoms, the necessary kinetic energy to penetrate a monolayer of graphene or h-BN can be estimated from the displacement threshold energies T_d^α where α is index for B, N, or C, atoms, respectively. This threshold energy is the minimum kinetic energy that an atom needs to absorb in order to be ejected from the system. If this energy is provided in a head on elastic collision with another atom, the kinetic energy of the incident atom like Rb is given by:

$$E_{kin}^{Rb} = 2(1+\beta)\frac{T_d^\alpha}{4\beta} \tag{3.1}$$

where $\beta = (m_\alpha/m_{Rb})$ is the atomic mass ratio, with α = B, N, or C. With the values of T_d^α from first principles, E_{kin}^{Rb} is approximately 50 eV for both h-BN and graphene.[12] The electronic and geometric structure of clusters are commonly known to be unaffected when deposited on inert supports such as h-BN. Therefore, such clusters can be considered as pseudo-free.[145] However, it has been shown that even a weak interaction of Au and Au_2 with the defect-free inert h-BN surface can have an unusually strong influence on the binding and catalytic activation of the molecular oxygen by pushing electrons from the gold to the adsorbed oxygen. Therefore, Au supported on the h-BN surface (pristine or defected) cannot be considered as a pseudo-free atom. The support effects have to be taken into account.[127] Due to the strong σ-bonds with strength in the order of 10 eV, defect-free monolayers of hexagonal boron nitride and graphene are expected to act as perfect and strong membranes that are inert to chemical attack and impermeable for atoms. If atoms penetrate a sp^2 layer, they need significant energies that can lead to knocking out of constituent atoms. On the other hand, the implantation between the sp^2 layer and the substrate implies that the atoms do not penetrate deeper into the substrate, which imposes an upper bound to the ion energy.[141] BN/metal systems are often used in gaseous atmospheres. Atoms and molecules may diffuse and intercalate at the BN/metal interfaces. For instance, the periodic corrugation of monolayer BN on Rh(111) can disappear when a layer of hydrogen atoms intercalate at the BN/Rh interface[138] and the BN-substrate interaction can be tuned by the intercalation, which could affect the physico-chemical properties of BN overlayers.[97] Moreover, BN overlayer on Ru can even be decoupled from the Ru substrate by oxygen intercalation in O_2 atmosphere.[146] M. L. Ng et al[147] have intercalated CO in h-BN/Rh(111) at only 300 K and under pressure of 0.01 mbar. In this experiment, h-BN was found to decouple electronically from the Rh(111) substrate undergoing a mostly flat layer and the pristine h-BN can be restored upon heating to above 625 K, demonstrating possible opportunity for a reversible tuning of the electronic and structural properties of monolayer BN sheets. H_2, H_2O, O_2, as well as a mixture of O_2 and CO also have been tested for intercalation at room temperature (RT) but only CO can intercalate because the other gas desorbs from Rh(111) below RT. It was also found that intercalated CO resides at the same adsorption sites as on the free Rh(111) surface, *i.e.*, in the top and hollow sites of the Rh(111), assuming the same coverage and site distribution as on a free Rh(111) surface. Functionalization could change the solubility of the monolayer in common solvents or tailor its electronic and magnetic properties. It has been shown that defect-free h-BN can be functionalized either by doping or by the metallic substrate for becoming catalytically active.[136] Atomic or molecular preferential adsorption on a template surface provides a facile and feasible means of fabricating ordered low-dimensional nanostructures with tailored functionality for novel applications. The essential interest in h-BN comes from its unique ability to trap molecules, clusters and atoms thereby allowing it to function as a surface template in applications such as hydrogen storage at nanoscale. Covalent functionalization of h-BN with hydroxyl and hydrogen has been explored. It was found that the most stable products are formed by reaction of OH with boron in the depression region of h-BN and that the transition state energy is considerably reduced in the depressions. This suggests that one can expect a strong templating effect for radical-based functionalisation of h-BN/Rh(111).[122] The most energetically preferential site of adsorption is dependent on the type of atomic species (B or N) that is substituted by a dopant in the lattice. For example, in C-doped h-BN the binding energy of adsorbate can be expressed as:

$$\delta E = E_{ads/C-BN/Rh} - E_{C-BN/Rh} - E_{ads} \tag{3.2}$$

where $E_{ads/C-BN/Rh}$, $E_{C-BN/Rh}$, and E_{ads} are the total energies of the structure with adsorbate, without adsorbate, and the adsorbate, respectively. Thus, a bound atom/molecule will be associated with a negative binding energy. In this case, the calculated results of density functional theory showed that atomic species are bound to h-BN while the molecular species are not.[140]

4 Experimental

This chapter introduces the reader to the setup and the various experimental components used in this thesis. It is a completely home-built device allowing *in-situ* morphology and catalytic activity characterization of size selected clusters based catalysts. This setup consists of an ultra high vacuum (UHV) system (shown in Fig. 4.1), equipped with a size selected cluster source, gas-surface analysis instrument and a scanning tunneling microscope (STM). Working with clusters as model catalysts require good vacuum conditions (less than 10^{-9} mbar) to avoid too much pollution of the sample and assure uncontaminated clusters during the deposition period. The whole system is equipped with a stage of turbo-molecular pumps in continuous operation. Since the STM microscopy resolution is very sensitive to mechanical vibration, and is hardly compatible with the turbo-molecular pumps, the microscope chamber is separately pumped by an ion pump, which has no moving parts and therefore does not vibrate. The STM can be coupled to the deposition chamber by a small intermediate chamber (transfer chamber). The transfer chamber serves for sample and tip loading as well as an airlock for STM coupling and decoupling. It can also be used as a chemical vapor deposition (CVD) chamber. The clusters are produced using a Cold Reflex Discharge Ion Source which will be described later. They are sorted by size and released into the deposition chamber by a quadruple mass spectrometer (QMS). No valve separates the source from the deposition chamber which are forming a single enclosure. The sample is fixed onto a manipulator that may be heated or cooled and its preparation is accomplished by ion bombardment and heating. After cluster deposition, the sample is transferred in the STM chamber for observation. Subsequently, the sample is dragged back to the deposition chamber to study the chemical reactions of the clusters using a home-made device called sniffer. In the following, the sniffer, which is used for catalytic activity measurements, the gas analysis techniques, the STM principle operation and the setup source for cluster production and deposition will be presented.

4.1 UHV compatible reactor

In order to conduct catalytic measurements, a sniffer has been designed to deliver and collect reaction gases to and from the surface. In a typical measurement, gases are injected contin-

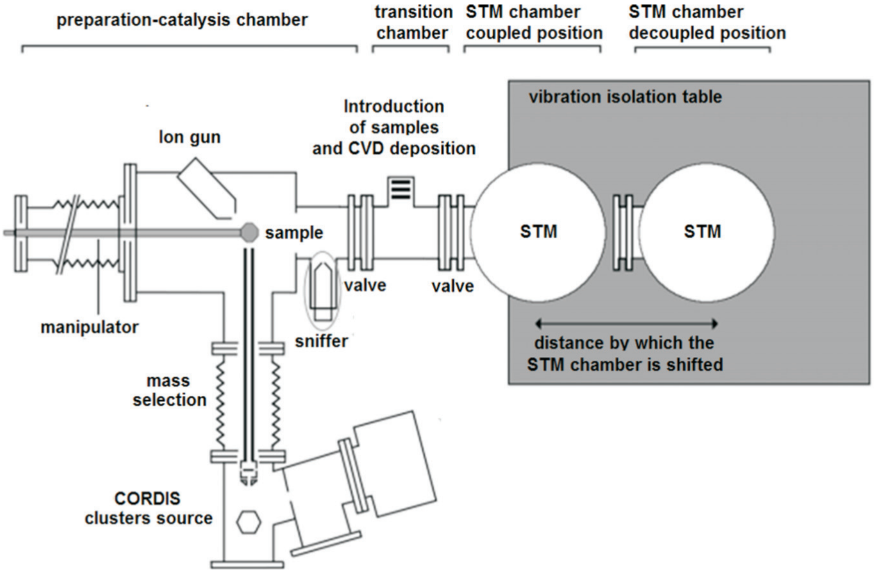

Figure 4.1 – schematic overview of the experimental setup.

uously or as pulses of high pressures onto the sample. The reaction products then desorb from the surface and get trapped in the "Collector" (Fig. 4.2) and are continuously analyzed by means of an integrated quadrupole mass spectrometer (Prisma QMS 200 Pfeiffer-Vacuum). A hot yttrium filament emits electrons that are accelerated through an aperture into the ionizer. The aperture also serves to pump the Collector. The electrons ionize the gas, and a system of electrostatic lenses guides the ions through a 1 mm 2 hole into the quadrupole. The sniffer used in this thesis is an improved version of a previous one described elsewhere.[148] The motivation behind these improvements is to increase the detection sensitivity from the sample by reducing the unwanted background contribution of the sniffer itself. In this sense, 2 major developments can be cited; the first was to introduce a heating system in which the sniffer core could be degassed prior to any catalytic experiment. This was accomplished using a simple home made oven of a non-porous ceramic material (Al_2O_3) and a tantalum (Ta) wire (diameter of 0.1 mm). During the reaction, the system is kept warm in order to avoid molecules stacking. The second improvements was to replace the upper part of the collector, previously made of stainless steel, by a tube made of quartz. At approximately 400 °C, the surfaces of the quartz becomes dehydrated and so the quartz tube will not desorb water. Moreover, the quartz electrically isolates the head of the sniffer from the rest of its components. This allows the study of what is called the electrochemical promotion of catalytic reactions (EPOC).

4.1.1 Temperature desorption spectroscopy

The forces binding the molecules adsorbed on the surface of a material can be of low energy nature such as van der Waals attraction forces. They may also be of high energy nature such as chemical bonding forces with electronic orbitals overlap. A simple way to break these bonds is to provide thermal energy or thermal desorption. By performing this thermal desorption in

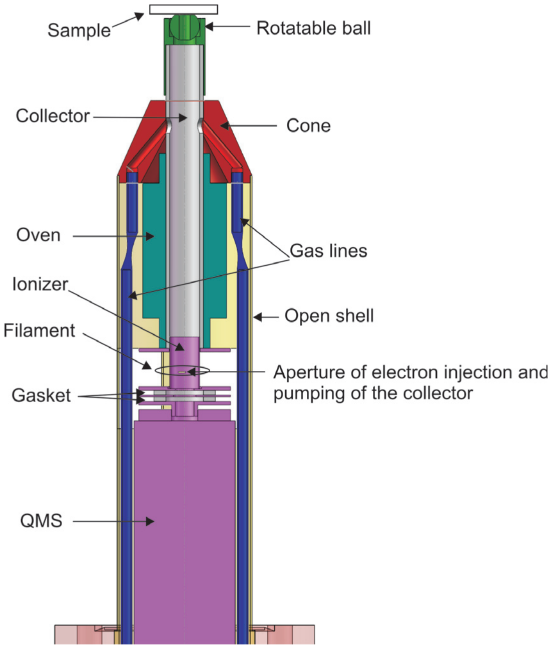

Figure 4.2 – 2D representation of the sniffer.

vacuum, it could be simple to analyze desorbed molecules using a mass spectrometer. Temperature desorption spectroscopy (TDS), is one of the fundamental techniques of surface science. This technique is performed by linearly increasing the temperature of a sample while measuring the partial pressures of the desorbing gas species. It is used to determine the relative coverage and activation energies of the desorbing species. The reader can find a detailed analysis of TDS in Ref.[149,150] and references therein. The desorption of a molecule from a surface is an activated process,*i.e.*, the molecule needs to overcome an energy barrier to leave the surface. The desorption rate can be calculated using the Polanyi-Wigner expression.[149]

$$\frac{d\Theta}{dt} = -\nu\Theta^n e^{-\frac{E_d}{k_b T}} \tag{4.1}$$

Where E_d is the activation energy to desorption, Θ is the adsorbate coverage, ν is a frequency factor and n is the Kinetic desorption order (n=1 indicates a simple desorption process). If E_d is larger or ν is smaller, the desorption peak shifts to higher T. There are different procedures to evaluate the activation energy from TDS spectra. Especial and simple is the Redhead analysis in which the activation energy can be derived by a simple relation between E_d, ν and T_{max}. Redhead assumed that activation parameters are independent of surface coverage and that desorption followed 1^{st} order kinetics (n=1). According to Redhead's equation[151]:

For a linear temperature ramp: T = T_0 + β_H t. Combining with equation 4.1 yields:

$$\frac{r_d}{\beta_H} = -\frac{\Theta}{dT} = \frac{\nu_n}{\beta_H}\Theta^n e^{-\frac{E_d}{k_b T}} \tag{4.2}$$

$$\frac{E_d}{RT_{max}} = \ln\frac{\nu_n}{T_{max}}\Theta_{max}\beta_H - \ln\frac{E_d}{RT_{max}} \tag{4.3}$$

Where T_{max} and Θ_{max} are values at desorption peak maximum. Using Redhead's approximations we get the simplified equation:

$$E_d = RT_{max}[\ln\frac{\nu_1 T_{max}}{\beta_H} - 3,64] \tag{4.4}$$

Where E_d is given in kJ/mol and T_{max} in Kelvin. ln $\frac{E_d}{RT_{max}}$ is relatively small compared with the first part and is estimated to be 3.64. For $10^8 < \frac{\nu_1}{\beta} < 10^{13}$ K^{-1}, the error introduced through this estimate is less than 1.5 %. More accurate, but more complex are analyses such as the ones described by King[149] or by Bauer.[152]

The measurement of the partial pressures of the desorbing molecules is done with a mass spectrometer, which senses the mass to charge ratio (m/z) of the molecule. For the measurements undertaken in this work, a quadrupole mass spectrometer was used. Since TDS is sensitive to the mass of the molecule, the process gives direct information about what is desorbing from the surface. In addition, TDS gives information about lateral interactions between adsorbates on the surface which is known as the kinetics of desorption. This is done by giving a quantitative measure of the dependence on coverage of the desorption energy. The number of desorbing particles depends on the rate of desorption which increases constantly with T and the number of adsorbed particles which decreases steadily with T. Because the adsorbates may interact with each other, the effective particle-surface interaction potential is in general coverage dependent, so that also the desorption barrier is coverage dependent. For example, Figure 4.3 displays TDS curves of hydrogen on W(100) showing two desorbing states that depend on the reaction order n (β_1 is a first order desorption and β_2 is a second order). Each curve corresponds to a different initial coverage.[13] The inset of the figure presents an example of a typical zero-order desorption kinetics observed in thick layer when supply of molecules is infinite.

There is a range of techniques for studying surface reactions and molecular adsorption on surfaces which utilize temperature-programming such as TPR (Temperature Programmed Reaction). However, there is no substantive difference between TPR and TDS. The basics of TPR are very simple, involving adsorption of one or more molecular species onto the

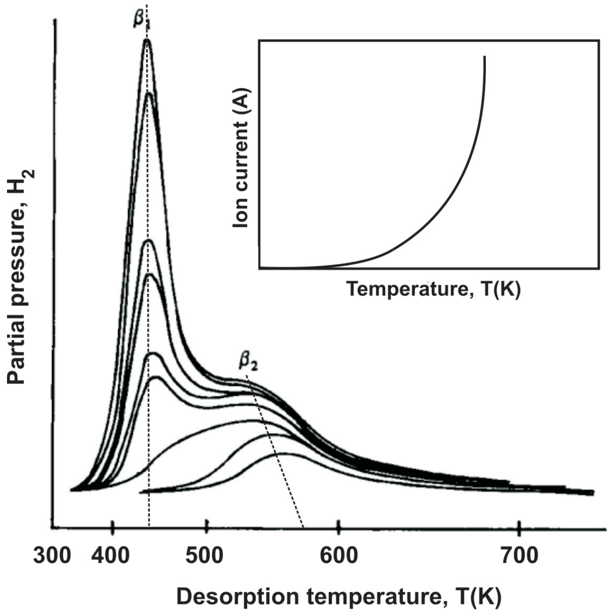

Figure 4.3 – Thermal desorption curves of H on W(100) showing β_1 and β_2 states. The inset shows a zero-order desorption kinetic. Adapted from Ref. [13]

sample surface at low temperature (frequently 300 K, but sometimes sub-ambient). Afterward, the sample is heated in a controlled manner (preferably a linear temperature ramp) while monitoring the evolution of species from the surface.

4.2 Scanning tunneling microscopy (STM)

The STM invented by Binnig and Rohrer in 1981 [17] is widely used nowadays, both in industry and part of basic research, as it allows the study of surfaces at the atomic scale. Its ability to provide a dimensional representation of the sample classifies it among the methods of choice for the characterization of roughness, the observation of surface defects and the determination of the size and conformation of the molecules or other adsorbates present in nature or purposely deposited on supports. It is a local probe analysis method. Unlike methods such as helium diffusion, or other ion scattering spectroscopy (ISS), which give information averaged over a surface, the scanning tunneling microscopy allows to locally discriminate the surface at the atomic scale. In this thesis the STM is used to analyze the model catalyst morphology.

4.2.1 Operational principle

The operation of a scanning tunneling microscope is briefly shown in Figure 4.4. The probe used is a metallic tip which is positioned at a distance d of few angstroms from a conducting or semiconducting surface. At this distance, and when a potential difference is applied between

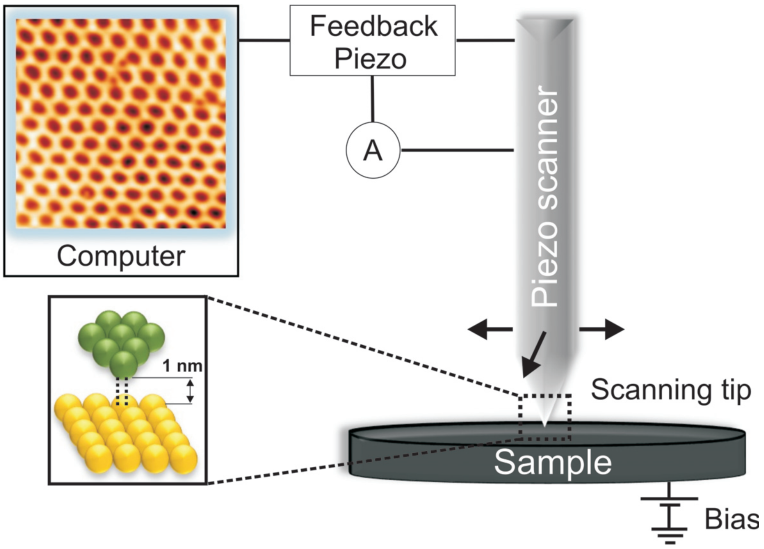

Figure 4.4 – Diagram reassuming the STM working principle. A metallic tip is placed close to the sample surface (usually between 5 and 10 Å). The tip is moved on the plane parallel to the surface by a piezoelectric crystal. A bias is applied between the sample and the tip and the tunneling current is measured. As the tip moves across the surface a feedback system changes its vertical position in order to keep the tunneling current constant. The tip vertical position, as a function of its x-y plane position, is used to produce a map of the surface that is visualized on a computer.

the tip and the sample, a tunnel current I_t in the order of nA or less can be established between the tip and the surface. This current, strongly, depends on the distance d. A mechanical system moves the tip parallel to the surface (x, y) and perpendicularly along the z axis. In the mode of the most common operation, a control loop measures the tunneling current I_t and adjusts z so as to keep I_t constant. The z value is related to the topography and the electronic structure of the surface. The z (x, y) function corresponds to an image of the surface. This phenomenon of a non-contact current, in contradiction with obvious classical mechanics, is a beautiful application of quantum physics. STM in the constant current mode was, always, used in this work.

4.2.2 Tunneling effect

When two surfaces are sufficiently close to one another, the electronic orbitals overlap and a flow of electrons is established through the potential barrier of an electrode towards the other and vice versa, resulting in a zero net current. If a potential difference is applied, the balance is upset and a tunnel current appears. The predominant model of the tunneling current in STM is based on Bardeen theory formulated in 1961.[153] The concept is to consider that the small overlap of the tip and the surface particles wave functions could be treated by first order perturbation theory. On this basis, Tersoff and Hamann have developed a simple theory in which the STM tip is assumed metallic and has such form that can be simulated to an s type

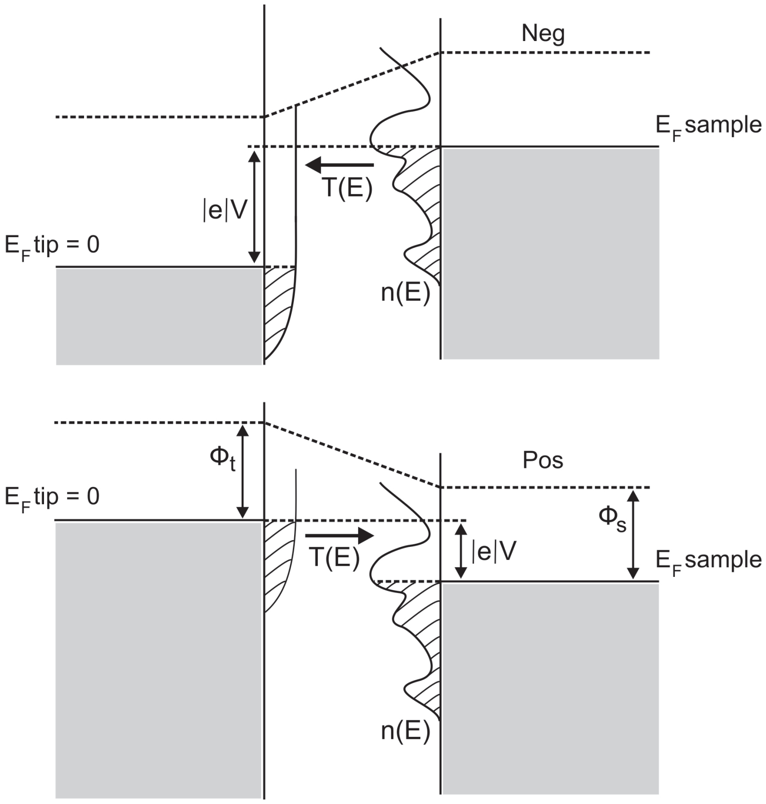

Figure 4.5 – Electronic structure of the tip and sample with a negative and positive bias applied to the sample. The length of the arrows going between the tip and sample indicates the contribution to the net current of different electronic states. The states close to the fermi level contribute the most to the current since electrons have to overcome a smaller barrier.

atomic orbital with a characteristic radius R and density of states $\rho_{\text{tip}}(\mathrm{E}_f)$ at the Fermi energy E_f.[154]

By applying a potential V, a net electron flow is induced. The tunneling current takes then the relatively simple form:

$$I(V) = V\rho_{\text{tip}}(E_f)\rho_{\text{sample}}(r_0, E_f) \tag{4.5}$$

where $\rho_{\text{sample}}(\mathrm{r}_0,\mathrm{E}_f)$ is the sample density of states taken at r_0 (the central position of the tip). It is interesting to note that the tunneling current provides a direct measure of the electronic density of states at the Fermi level. It does not provide a direct image of the atoms. However, this current also depends on the tip density of state. This value is, unfortunately, never exactly known because it is specific to each tip. As a first approximation, one can consider that the surface state wave functions decrease exponentially in vacuum with an effective length equal to $1/\mathrm{k}_{eff}$:

$$k_{eff} = \sqrt{\frac{2m_eB}{h^2} + \left|k_{par}\right|^2} \tag{4.6}$$

where m_e is the electrons effective mass, k_{par} is the wave vector parallel to the tunneling electrons and B the barrier potential. B is dependent of sample and tip work function (Φ_s, Φ_t) and the applied voltage (V). The tunnel current between the tip and the sample will be in the following form:

$$I_t = e^{-2k_{eff}z} \tag{4.7}$$

This term reflects an exponential variation of the tunneling current which will have important consequences experimentally. The slightest variation in tip-sample distance induces a strong modification in the current value. For instance, the tip-sample distance should be controlled very accurately (typically at 0.015 nm). The simplest adaptation of the previous model gives the term of the following tunneling current:

$$I_t = \int_{E_{f,tip}}^{E_{f,tip}+eV} \rho_{\text{tip}}(E)\rho_{\text{sample}}(E+eV)T(E,V)dE \tag{4.8}$$

T (E , V) is the transmission coefficient which depends on the electron energy and applied voltage. The tunneling current is the product of the electronic density of states of the tip and the sample for which the energy is between E_F and (E_F + eV) (see Fig. 4.5).

4.2.3 Details of our STM

The scanning tunneling microscope used in the context of this thesis is a custom made previously developed in our group.[4,14,155] It is enclosed in UHV and employs a double bath cryostat, allowing us to work at 4 K or at 80 K, as well as at room temperature. All Along this thesis, STM measurements were done at 80 K. A cut view of the STM device is shown in Figure 4.6. To achieve atomic resolution, the STM must be provided with a system capable of reducing the external perturbations in order to obtain good stability in the tunnel junction. For this, our STM block is suspended by three long springs connected at the top of the chamber (including additional eddy current dampers). The only other mechanical contacts between the STM and the rest of the chamber are very thin gold wires for electrical and thermal contacts. To avoid vibrations due to the boiling of the nitrogen liquid contained in the outside cryostat, it is possible to pump gas into the cryostat to solidify nitrogen. For mechanical isolation, the chamber is mounted on rails, in order to isolate it from the rest of the installation. For the same reason, the chamber is placed on a concrete table (1600 kg) supported by four Newport feet I-2000 pneumatic feets. A laminar air flow through the feets isolates and stabilizes the table. On the STM block, shown in Figure 4.6, are placed the positioning system and the sample holder. The sample is supported by a drawer that is positioned on top of three shear piezoceramic motors. It is possible to move the drawer in the plane perpendicular to the STM tip, and therefore to select the surface area that will be imaged. A spring clamp system is used to secure the sample firmly against the block when one wishes to take measurements, while a pneumatic piston can release it to withdraw the sample off.

4.2.4 Tip preparation

A tungsten wire of a 0.25 mm diameter was etched with a 2 molar electrolytic solution of NaOH. As shown in Figure 4.7, the solution forms a membrane inside a silver ring electrode. The wire passes through this membrane and is etched when an electric potential is applied between the wire itself and the silver electrode. The tungsten reacts with sodium hydroxide and water producing water-soluble tungstate and hydrogen following the reaction:

$$W(s) + 2OH^{-} + 2H_2O \rightarrow WO_4^{2-} + 3H_2(g) \tag{4.9}$$

A dc voltage, between 10 and 15 V, is used for electrochemical etching. As the etching proceeds, chemical reaction reduces the diameter of that portion of the tip wire that is restricted to being within the electrolyte. When the tensile strength of the etched region of the metallic wire fails

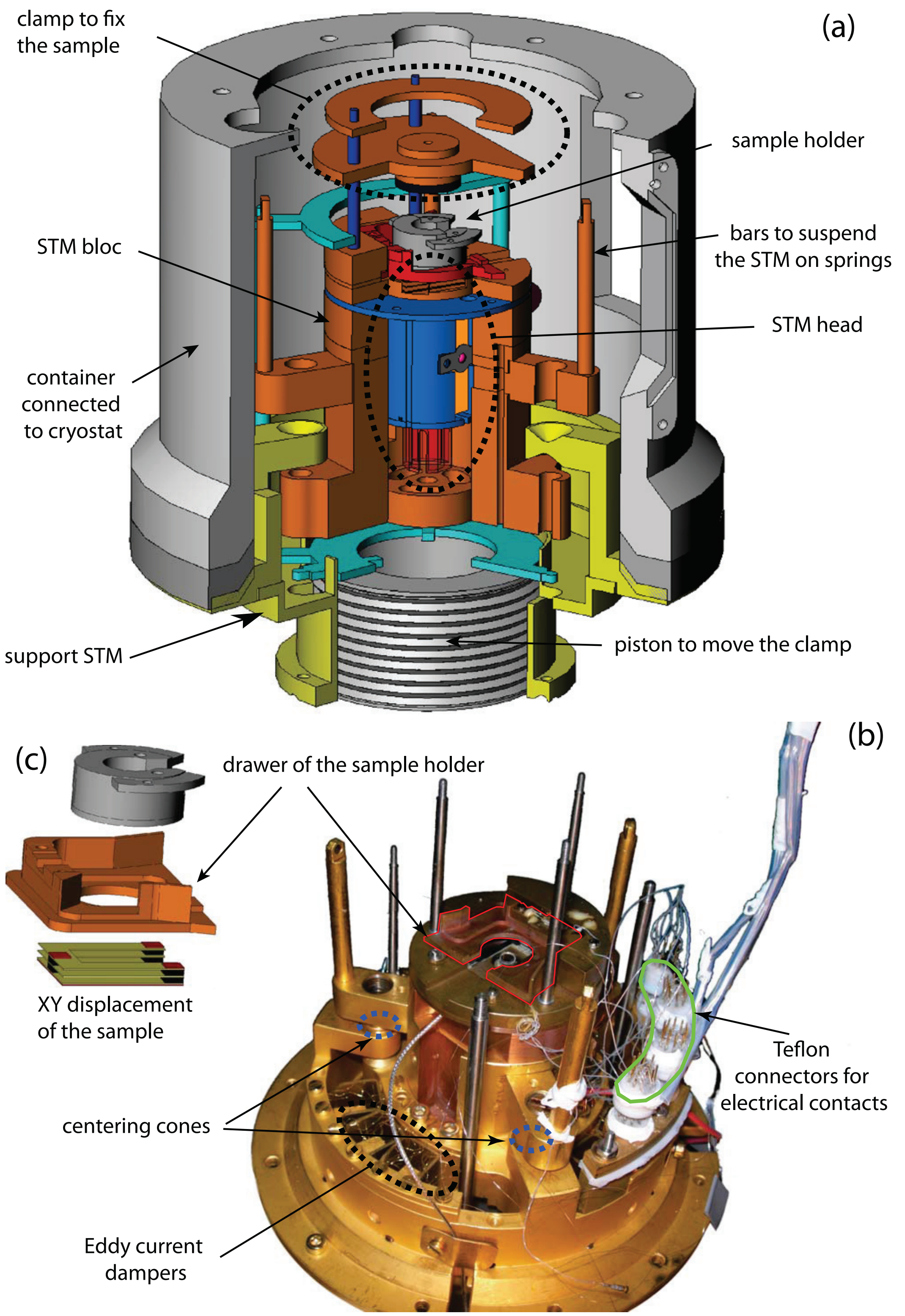

Figure 4.6 – (a) Cut view of the STM block and (b) photo of the system outside the vacuum chamber and (c) a detailed view of the sample-holder and piezo stack for the sample macroscopic displacement. Adapted from Ref.[14]

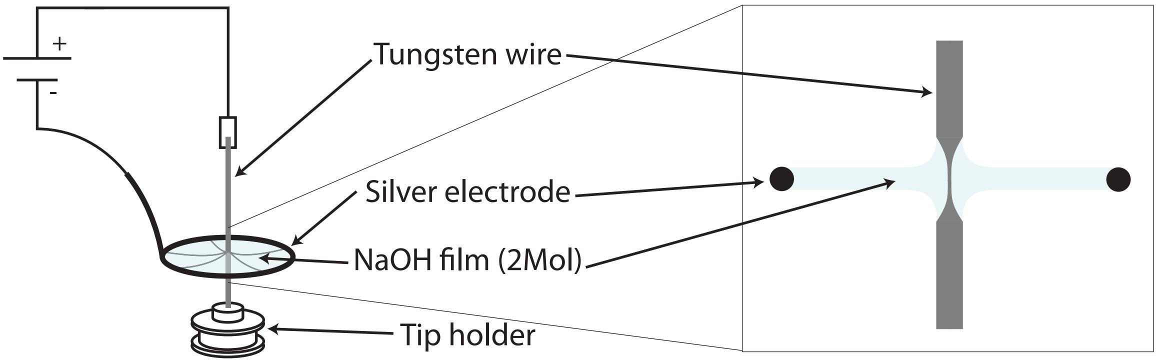

Figure 4.7 – Diagram of the setup for the tip preparation. Adapted from Ref.[4]

to counteract the gravitational pull of the lower part of the tip, the lower part drops off. In this arrangement, as soon as dropping off occurs, the circuit is switched off and the etching process terminates. This is the usual floating-layer technique of electrochemical etching. The great majority of the tips produced this way give immediately atomic resolution images.

4.3 Cluster production and deposition

Clusters are produced by sputtering from a CORDIS (Cold Reflex Discharge Ion Source) ion source which generates a 20 keV rare gas ion beam.[89] The source is represented in Figure 4.8. Rare gas ions are produced in a plasma and accelerated onto the metal target by a potential difference of 20 keV. The typical measured plasma current is on the order of a few amperes. Neutral and charged clusters (among others) are ejected from the metal. Those charged are directed and focused by a system of electrostatic lenses into a Bessel Box. Only particles having a certain energy and mass emerge from this box which, therefore, acts as a barrier for neutral particles and an energy filter as well. The filtered ions are directed through a quadrupole into the deposition chamber. This quadrupole serves as a guide and mass selector for particles of mass M. The quadrupole is formed by four parallel metal cylinders whose radius is defined by the inner and the outer diameter by a ratio of 1.15. The cylinders are electrically connected two by two and are powered by an opposite DC and AC voltage. Only the particles of a defined ratio Q/M have a stable trajectory and can be guided into the deposition chamber. A mass spectra of platinum and iron clusters used in the present work and produced by this cluster source are shown in Figure 4.9. The first small peak visible from the left is due to Kr ions. At the exit of the quadrupole, the particles therefore have a defined kinetic energy, charge and mass. A potential applied to the sample slows down or accelerates the clusters so that they land on the surface with the desired kinetic energy. The coverage is determined by the beam current density and the deposition time. A faraday cup positioned in the deposition chamber is used for cluster current measurement which is usually of the order of 10^{-10} A.

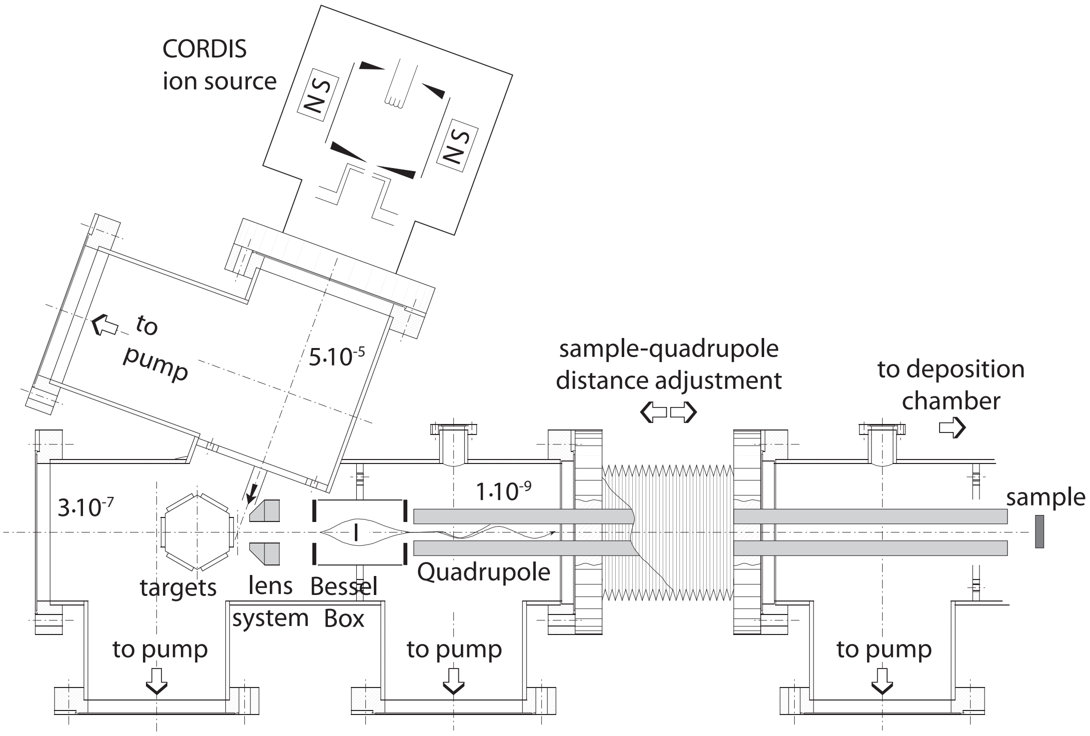

Figure 4.8 – Schematic view of the size selected cluster source. Adapted from Ref.[14]

4.4 Sample and sample holder

Rh(111) single crystals, with a polished (111) surface, have been purchased from Mateck GmbH Corporation in the shape shown in Figure 4.10, where the exposed (111) surface is 0.39 cm^2. The sample holder consists of two parts made of molybdenum, the block and the cover that are welded together with Ta stripes. The block is cylindrical and has two small cavities which allow it to be positioned and attached into the manipulator. An opening allows the heating filament to be positioned close to the surface. The thermocouple is inserted into a hole on the back of the sample and a good thermal contact is guaranteed by gluing the thermocouple and the sample with AREMCO ULTRA-TEMP 516 glue. The sample is clamped to the cover by a Ta sheet.

4.5 Experimental procedure

This section gives the experimental procedure of manipulations performed in the UHV systems combining a size selected cluster source, STM and a UHV compatible reactor, already described in this chapter.

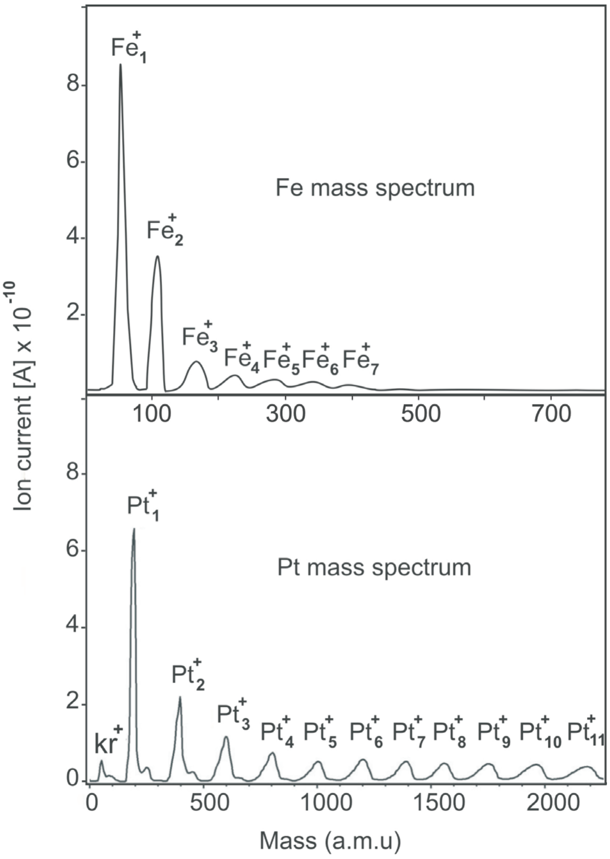

Figure 4.9 – Mass spectra obtained by the bombardment of a Fe and Pt targets by the Kr^+ at 20 keV.

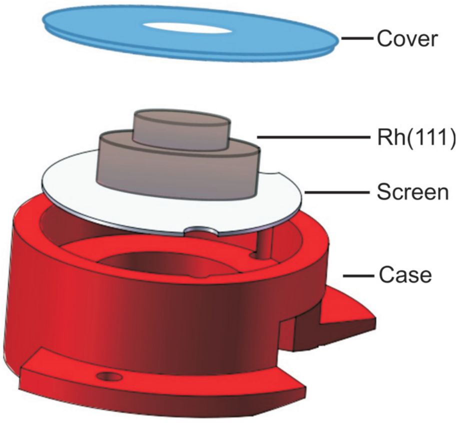

Figure 4.10 – Sample holder design.

4.5.1 Surface preparation

In all pursuing chapters, the h-BN layer was grown on Rh(111) by following the standard procedure as reported in literature.[156] Clean Rh(111) surface was prepared in UHV by Ar^+ sputtering (1 kV, 1.5 μA, 300 K, 3 h) and flashing to 1250 K. The h-BN was grown by thermal decomposition of 50 L (1L = 1.33×10^{-6} mbar×s) of borazine $(HBNH)_3$ on Rh(111) kept at 1150 K. Borazine was stored under dry ice at all times except when charging the gas line. The cleanliness of the sample was examined with STM after each preparation.

4.5.2 Clusters deposition

In chapter 5, mass selected Pt_7 clusters were deposited at room temperature on the prepared h-BN layer, using a retardative voltage on the sample, with a kinetic energy of 1.2 eV/atom. This energy assures soft landing conditions and prevents unwanted processes such as fragmentation and implantation. Platinum target was sputtered by 20 keV Kr^+ ions in the cluster source, the extracted cations are mass selected by the quadruple and then directed to the sample.

In chapter 6, energetic deposition of mass selected Pt_7 on h-BN/Rh(111) was achieved, perpendicularly to the prepared h-BN layer with a well-defined kinetic energies at 30, 60, 100, 170, 314 and 416 eV/atom at room temperature.

In chapter 7, energetic deposition of mass selected Pt_7 on h-BN/Rh(111) was performed at E_k = 170 eV/atom at room temperature.

In chapter 8, mass selected Fe_3 clusters were deposited at 100 K on h-BN/Rh(111) with a kinetic energy of 1.2 eV/atom.

Through all the experiments, the initial deposited clusters density on h-BN/Rh(111) surface was 0.2 % ML. The coverage given in ML (1ML is equal to 1.7×10^{15} atom/cm^2 of the Rh(111) atomic density) is estimated from the cations current, measured with faraday cup, and the deposition time.

4.5.3 STM imaging

STM is the main investigation tool for studying stability and morphology of the clusters. The STM images were taken, in constant current mode at V_t = -1 V and I_t = 100 pA at a temperature of 80 K, at every stage of the experiments ,*i.e.*, before and after cluster deposition, after gas exposure and after annealing except if otherwise specified.

4.5.4 Catalytic reaction

In chapter 5, CO oxidation was studied using alternating $^{13}C^{16}O$ and $^{18}O_2$ pulses (at a frequency of 0.2 Hz) on the Pt_7/h-BN/Rh(111) catalyst as a function of temperature (100-700 K) using a heating rate at 1.5 K/s. It should be noticed that the use of the isotopic gas allows to distinguish the product from any residual CO_2 in the background. At the same time, $^{13}C^{18}O^{16}O$ resulting from the reaction was captured and analyzed by means of the quadruple mass spectrometer combined in the sniffer. This enables us to study the reaction dynamics as a function of the sample temperature. The time duration between two consecutive pulses was 5 s.

In chapter 5, 6 and 7, CO binding to Pt is monitored using TDS of $^{13}C^{16}O$ isotopic gas as a function of temperature (100-600 K) using a heating rate at 1.5 K/s.

For ammonia synthesis (chapter 8), dissociated ^{15}N was reacted with H to form NH_3. Temperature programed reaction (TPR) was performed by dosing the surface with $^{30}N_2$ at low temperature under continuous hydrogen steady flow then heating within a range of 100 to 800 K at a rate of 1.5 K/s.

5 Pt_7 on h-BN/Rh(111): Stability and catalytic activity for CO oxidation

CO oxidation reaction on transition metals, especially on Pt, is an important model reaction which has been widely studied. In this chapter, the stability and catalytic activity of supported Pt_7 clusters on h-BN/Rh(111) were experimentally studied for CO oxidation. The catalyst stability was investigated before and after the reaction using STM, and the catalytic activity was studied by means of TDS and TPR. It was found that annealing under reaction gas promotes catalyst intercalation under h-BN at 700 K while the intercalation can, only, occur at 900 K in the case where the Pt clusters are not exposed to the reaction gas. A high catalytic activity was observed when the catalyst remains supported on h-BN. In this case, the reaction started at 480 K. Below this temperature, the catalyst was completely poisoned by CO. The catalytic activity was strongly reduced when the Pt clusters undergo partial intercalation, because at relatively low pressure, the CO adsorption on Pt is screened by h-BN. Nevertheless, the reaction can start at only 380 K, revealing a reduction by 100 K in the Pt poisoning as a result of substrate effect.

5.1 Introduction

Catalysis is a broad and pioneer field of research nowadays. Its applications range into a variety of industrial chemical areas which all together cover a world annual trade of about 10 billion US dollars. In order to increase the benefits, costs as well as efficiency should be improved. While the cost requires an appropriate low material consumption, efficiency relies on technological advancement and state of the art catalyst engineering. The chemical reactions of interest employ, in general, high cost materials. For example, car exhausts use expensive elements such as Pt, Rh and Pd to oxidize CO, NO_x and hydrocarbons. Therefore, material downsizing or new efficient catalyst substitution would emphasize the trends for cheap catalyst production. Catalysis is a very complex process. So, to understand the behavior of real catalysts, well-defined models have to be elaborated and investigated in order to simplify the reaction mechanisms. Model catalysts consisting of small supported clusters prepared in high-vacuum and approaching the ideal catalyst, have attracted a lot of interest due to their high catalytic efficiency with respect to their size. Clusters that contain only a small number of atoms can exhibit a range of fascinating properties, which are of significant interest in catalysis, due to a variety of factors including their very high ratio of surface-to-bulk atoms, [157] electronic structure, geometry, as well as their interaction with their support. [158] It has been shown that low-coordinated, unsaturated atoms often function as active sites. [159] So downsizing metal nanoparticles to subnanometre clusters or even single atoms could significantly enhance their catalytic activity and/or selectivity [160–164] while substantially lowering their price as a result of significant reduction of metal consumption. However, the high number of low coordination sites and mobility of clusters also significantly destabilize such particles and makes them prone to ripening. [165] Stability which is a major concern in cluster science is believed to be a key factor determining the reactivity of heterogeneous catalysts. [166] The main processes resulting from the instability of the small clusters are dissociation, intercalation and ripening. [167] This latter process is the most common for catalyst instability and in most cases it is driven at elevated temperature. [165] The tendency of sub-nanoparticles to grow into larger clusters results in specific surface area reduction and may block the active sites of the catalyst. [168]

For efficient catalytic activity, noble-metals are usually used and should be finely dispersed on a support. [160] Methods for producing and soft landing size-selected clusters on supports are now well established. However, testing these clusters under realistic reaction conditions is challenging, requiring supports on which they remain stable. [157] High thermal stability, chemical inertness and mechanical strength contribute to a better choice of a suitable catalyst support. Nevertheless, it should be recognized that, even for metal particles of the same size, the support can strongly affect the intrinsic activity and selectivity of catalysts. [169–172] Therefore, investigation of supported cluster stability and reactivity is among the important challenges in heterogeneous catalysis. In this experiment we studied the CO oxidation and the thermal stability of mass selected and soft landed Pt_7 supported on h-BN/Rh(111), correlating the catalytic reactivity to the catalyst stability before and after the reaction. It should be noted that, CO oxidation on noble metal atoms supported on an h-BN surface has been, mainly, studied theoretically [173–176] and the inherent catalytic activity of smaller platinum clusters has not yet been elucidated. Although, doping h-BN with metals has also proven to be efficient in the catalytic conversion of CO to CO_2, [177] it has not been yet demonstrated experimentally that an h-BN monolayer, can be functionalized with Pt clusters in a uniform manner required for effective catalysis.

5.2 Results and discussion

5.2.1 Pt_7 supported on h-BN

AS a reference, Figure 5.1a visualizes a clean h-BN supported on Rh(111), the mismatch as well as the interaction between the 12×12 Rh(111) and the 13×13 top h-BN layer results in a corrugation with a periodicity of 3 nm and modulation height of 0.8 Å, close to what is reported in literature. [117] For more details on supported h-BN structure, the reader is referred to chap-

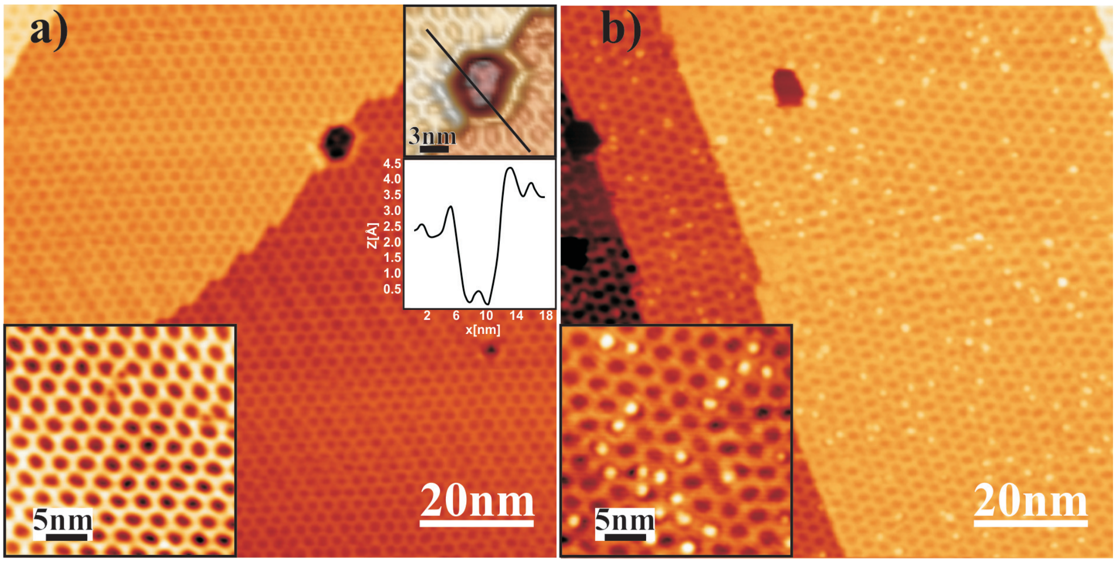

Figure 5.1 – Overview STM images of a) clean h-BN/Rh(111) showing the well-ordered honey comb structure with a periodicity of 3 nm and a corrugation height of 0.8 Å. b) Pt soft landing deposition at 1.2 eV/atom, showing white protrusions. The insets are magnified regions of the corresponding surface. The line profile is taken across the hole shown as an inset.

ter 3. The observed large terraces are separated by a monoatomic steps of 2.3 Å height. This value is very close to the Rh(111) monoatomic step height which can be calculated by the theoretical lattice constant of bulk rhodium according to $h = 1/\sqrt{3}\, a = 2.2$ Å ($a = 0.383$ nm). Some areas in h-BN display less perfect honey comb structures, especially on the wires. This is due to the fact that these weakly bound regions of h-BN are very sensitive to the STM tip distortion. Also, randomly distributed holes with different sizes are visible on h-BN. These defects are induced by sputtering damage during Rh(111) preparation which were not healed due to an insufficient temperature flashing. More interestingly is that the borazine gas was able to access these holes and forms h-BN as indicated in the 3D STM inset at the right corner in Figure 5.1a.

The STM topography in Figure 5.1b displays mass selected and soft landed Pt_7^+ clusters, deposited with $E_k = 1.2$ eV/atom on h-BN/Rh(111) at room temperature, as bright protrusions sitting mainly at the h-BN edge depressions in a random distribution. It is expected that the Pt clusters stand more precisely on the rim of the h-BN depressions.[32] Thus, at room temperature a deposited Pt cluster can easily diffuse across the surface until it becomes trapped in a depression. The ability of the h-BN depressions to trap small metal clusters is a result of strong covalent interaction between metal-boron (M-B) atoms where h-BN is close to the (fcc,top) configuration on Rh(111).[30]

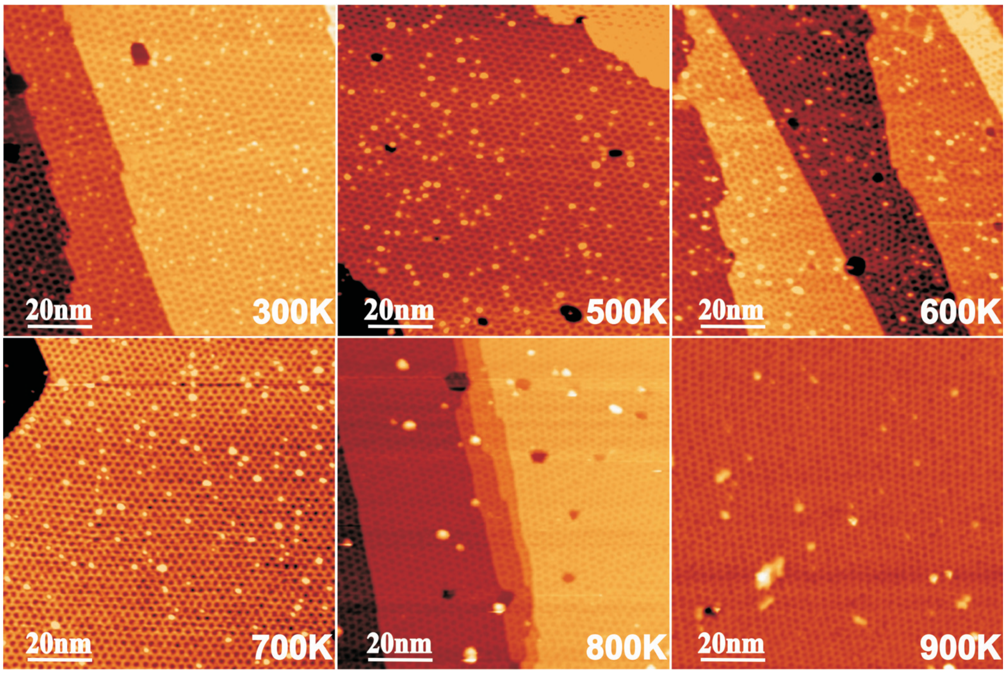

Figure 5.2 – STM images of Pt_7 clusters on h-BN/Rh(111) showing surface distribution and morphology: as deposited at 300 K (a), after annealing to 500 K (b), 600 K (c), 700 K (d), 800 K (e) and 900 K (f). The highly regular honey-comb structure refers to h-BN/Rh(111) and the bright like-protrusions to Pt clusters on top of it. Imaging was done with: V_t = -1 V and I_t = 100 pA.

5.2.2 Pt_7 stability

The STM images in Figure 5.2 show the evolution of Pt_7/h-BN/Rh(111) catalyst after annealing to different temperatures. The Pt clusters were deposited at 300 K with a density of 0.2 % ML ($1.7\text{x}10^{15}$ cm^{-2} with respect to the density of the Rh(111) unit cell) followed by successive annealing up to 900 K in steps of 100 K. In order to predict the structure of our adsorbed Pt clusters on the h-BN, apparent height histograms were extracted from each STM image and compared. The apparent height in conjunction with the cluster density evolution as a function of temperature allow us to have an insight on the stability of the Pt_7 clusters on the h-BN.

The histograms of the cluster height for different annealing temperatures are shown in Figure 5.5a, where one can observe, at 300 K, a narrow size distribution around 3.2 Å (relative to the bottom of a depression) which corresponds roughly to the diameter of one platinum atom (or one monoatomic step height in Pt(111)). A similar value has been found for a flat Pt_7 on TiO_2.[178] Evidently, the clusters do not undergo fragmentation or agglomeration since our initial density distribution at 300 K is the same as that estimated from the cluster deposition current. The limited Pt cluster diffusion, at room temperature, on h-BN/Rh(111) suggests their pinning on the surface. This could be attributed to stabilization via the h-BN intrinsic lattice defects or anchoring on specific sites of the moiré pattern. The difference in the work function of the wires and the depressions accounts for a barrier energy as high as 0.5 eV for species hosted inside the h-BN depressions. It seems that this barrier is enough to keep the Pt clusters trapped, prohibiting their spreading and agglomeration. According to the measured apparent height, we can conclude that the Pt_7 clusters are in planar configuration in contradiction to DFT calculation which predicts that the most stable configurations of Pt_n clusters on various free-standing h-BN sheets establish 3D configuration.[29] The 2D growth mode could be a result of anchoring the Pt cluster to the h-BN defects. Owing to their inertness, the 2D honeycomb structures with strong covalent bonds maintain relatively low surface energy compared to other solid chemical elements. For example at room temperature, the surface free energy of graphene is reported to be 46.7 mJ/m^2.[179] This energy value is considerably smaller than that of transition metal particles, *e.g.*, 2.69 J/m^2 for Pt and 2.94 J/m^2 for Fe.[180] Therefore, the Pt clusters should form 3D clusters at room temperature. However, in the case of h-BN/Rh(111), one can imagine that adsorption of Pt on the h-BN defects provide certain confinement effect to limit the cluster growing vertically in the case of small cluster size.

From the histograms and the coverage evolution shown in Figure 5.5a and c, with the temperature going up, one can see that the cluster density decreases, dropping from 0.2 % ML to 0.05 % ML at the end of the annealing. At the same time, a second peak around 5.2 Å increases simultaneously with no shift in the initial size until 700 K, which indicates a Smoluchowski ripening process. However, a significant broadening of the apparent height distribution is observed at 800 K, and the corresponding STM images show very few large particles distributed on the surface. Smoluchowski ripening strongly depends on the cluster size and density on the substrate. Decreasing the cluster size leads to an increase in the average inter-cluster distances, thus, promoting M-M over M-Substrate binding.[181] On the other hand, as the temperature reaches 900 K, the STM image shows the intercalated Pt as large flake-like features with an apparent height of 2.2 Å. The Pt particles can undergo intercalation in which the cluster adatoms detach and diffuse under h-BN, most probably, through the wires as they host high defects density acting as gates to intercalation. The spacing between h-BN and Rh(111) is relatively more larger than the spacing between atoms within h-BN layer plane (1.44 Å). This means that the hexagonal boron nitride, should be able to accommodate intercalated elements or compounds including Pt. This is typical for the h-BN supports where other systems show similar behavior; for example, Au and Co have been found to intercalate already at room temperature.[182,183] Using the truncated sphere model, one can estimate the cluster size evolution with temperature. The particle diameter is expressed as $D = 2r_w N^{1/3}$, where D is the cluster diameter expressed by the height of the supported clusters, N is the number of atoms in the cluster, $r_w = 1.57$ Å is the Platinum Wigner-Seitz radius. Table 5.1 contains the estimated cluster size evolution with respect to their STM apparent height. Since the measured height for a flat Pt_7 or one Pt atom is 3.2 Å, thus, for a bilayer cluster, the height should be given approximately by D = 3.2 x 2 = 6.4 Å, whereas, the measured apparent height is, only, 5.2 Å. Therefore, in order to estimate more accurately the number of atoms in the supposed spherical clusters, one should correct the above formula by adding 1.2 Å to D for each measurement corresponding to a 3D structure. Accordingly, table 5.1 can be obtained.

measured height [Å]	calculated size [atom/cluster]	corrected height [Å]	corrected size [atom/cluster]	structure
3.2	1	3.2	7	2D layer
5.2	5	6.4	9	3D layer
8.2	18	9.4	27	3D layer
12	56	13	74	3D layer

Table 5.1 – Calculated cluster size, using the truncated sphere model of Pt$_7$ with respect to their apparent height.

The stability of cluster-surface systems is still strongly debated. Studies which address the question whether the catalyst keeps its initial structure during reaction or not are sparse. Our experiment allows us to check the catalyst morphology before and after the reaction. In this context, we show how the reaction gas has a significant influence on the cluster stability. We started with a fresh Pt$_7$/h-BN/Rh(111) catalyst deposited at room temperature (Fig. 5.4a) under soft landing conditions. Afterwards, we performed a catalytic reaction by exposing the surface to alternating CO and O$_2$ pulses while increasing the surface temperature up to 700 K. Exposing the deposited clusters to the CO reaction gas induces a change in the cluster size and distribution as shown in Figure 5.4b. The clusters become bigger (in height as well as width) and less abundant. To further illustrate the effect of the gas on the cluster stability, the sample, at the end of the reaction, was kept at 700 K for 5 min while simultaneously exposing the surface to 60 L of CO impinging pulses. Then, the intercalation was found to be more pronounced and only few large clusters, appearing as bright protrusions, remain above the h-BN layer as shown in Figure 5.4c. The intercalated species are imaged as large flake-like features. Figure 5.4e (a zoom of the depicted region in Figure 5.4c) shows the intercalated and non intercalated Pt clusters as well as their respective schematic presentation. The line profile taken across the two distinct features reveals a decrease in the apparent height from 8.2 Å in the case of the non intercalated cluster to 2.2 Å in the case of the intercalated one, as shown in Figure 5.4d.

The corresponding apparent height histogram, in Figure 5.5b, shows clearly the evolution of the cluster initial state from a well-defined peak situated at 3.2 Å, for the as deposited clusters at 300 K, to a broad peak showing variant distribution between 2.2$\AA$ and 3.2 Å after annealing to 700 K under gas reaction. Moreover, one can clearly observe a second peak at 5.2 Å, which is reminiscent to a monolayer to bilayer cluster transition. The first broad peak is a combination between a monolayer cluster and intercalated Pt adatoms, as the 2.2 Å refers to the intercalation height observed before in Figure. 5.2f. Consequently, the Pt clusters not only undergo coarsening but also partial intercalation as well. It should be noted that the intercalation in pure temperature activated processes starts at 900 K but when combined with gas exposure it initiates at 700 K. Thereby, the stability is clearly affected by the chemical reaction which promotes intercalation. Gerbert et al. investigated the stability of Pt clusters supported on graphene/Ir(111) under CO exposure. They found that small clusters containing

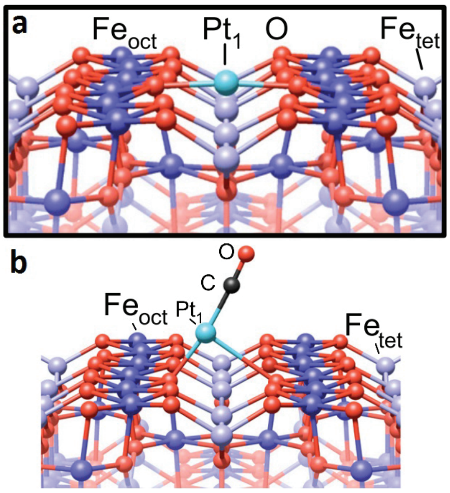

Figure 5.3 – Structural model of Pt_1-CO/Fe_3O_4(001). (a) adsorption configuration of (Pt_1) on the Fe_{oct} rows in between surface O atoms. (b) Upon adsorption of CO, the Pt adatom is lifted up and shifts perpendicular to the Fe rows to an off-centered position. Adapted from Ref.[15]

fewer than 10 atoms were unstable upon CO adsorption and they grow through Smoluchowski ripening, while bigger clusters remained immobile upon CO adsorption but became more three-dimensional.[184] CO oxidation is an exothermic reaction which stimulates energy transfer to the surrounding catalysts. It seems that the barrier induced by h-BN corrugation is somehow reduced upon Pt-CO binding, opening easy access to cluster ripening and intercalation. This phenomenon may be attributed to the skyhook effect (Fig. 5.3), in which ripening is promoted by cluster-CO binding. Examples of this effect exist in the literatures.[184]

For example, it has been shown that the interaction between catalytically active metal particles and reactant gases depends strongly on the particle size, particularly in the subnanometer regime where the addition of just one atom can induce substantial changes in the stability of Pt adatoms on Fe_3O_4(001) surface.[15] The results showed that carbon monoxide plays a role in the coarsening of highly stable Pt atoms on a Fe_3O_4(001) support (Fig. 5.3a): CO adsorption weakens the adatom-support interaction inducing mobility. The Pt adatom is lifted up by almost 1.3 Å away from the surface plane, and shifted perpendicular to the surface (Fig. 5.3b). This would promote its surface mobility.

5.2.3 CO oxidation reaction

In order to investigate whether the Pt clusters are catalytically active for CO oxidation or not, we performed CO TDS by dosing 20 L of the respective gas at 100 K onto Pt_7/h-BN/Rh(111) surface as well as onto $Pt_{27<x<74}$/h-BN/Rh(111) that has undergone partial intercalation, followed by annealing to 600 K until the desorption ceased. The reactants desorption as a function of temperature is a necessary but not sufficient condition for the reaction to occur. Basically, one would like to exclude any contribution of the support to the reaction. For this reason, the CO

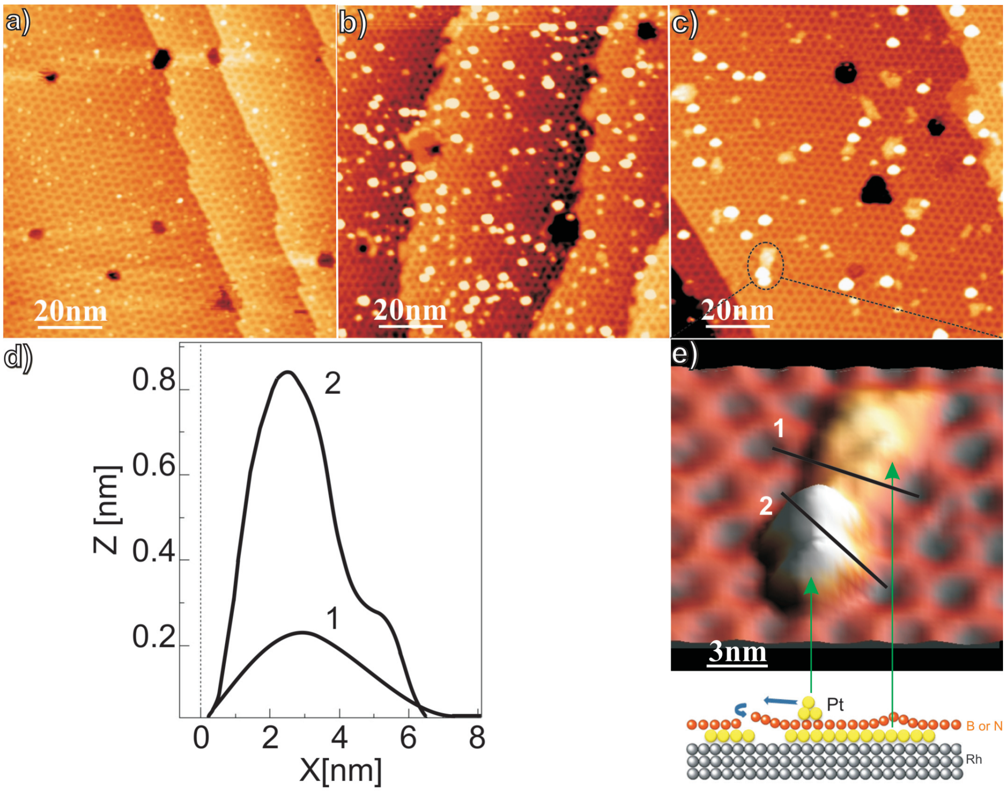

Figure 5.4 – STM images of Pt_7 clusters on h-BN/Rh(111) showing surface distribution and morphology of the clusters exposed to CO oxidation reaction condition , *i.e.*, exposed to CO and O_2 between 130 to 700 K: (a) as deposited at 300 K, (b) after reaction, (c) after exposing the sample in (a) to 60 L of CO at 700 K for 5 min. (d) cross-sectional apparent height along the indicated black lines in image (e) of both supported and intercalated Pt with distinct heights of 8.2 Å and 2.2 Å, respectively. (e) zoom in a region of the STM image (c) together with a schematic view, showing the cluster morphology of intercalated and non-intercalated Pt islands. Pt intercalation is more pronounced when exposed to the reaction conditions. Imaging was done with: Vt = -1 V and I = 100 pA.

TDS was first performed on a clean h-BN/Rh(111). The results are displayed in Figure 5.6. In the case of the clean h-BN (Fig. 5.6a), the CO desorbs from the surface at 260 K with an activation energy E_a = 0.7 eV estimated using equation 4.4 of chapter 4. As the coverage increases, the temperature peak moves down to 230 K and increases in size. The CO desorption peaks are attributed to the intrinsic defects present in the h-BN monolayer. The integration of the desorption peak gives 1% ML of defect concentrations, considering an initial sticking coefficient of 1 and one defect holds one molecule. This indicates that the CO molecules are unable to adsorb on the clean h-BN terraces, at least for the studied temperatures. In the case of Pt_7/h-BN/Rh(111), however, a broad peak extending from 300 to 600 K is obtained and is reminiscent to CO desorption from the Pt cluster terraces at 400 K, with an activation energy E_a = 1.1 eV, as well as from steps at 490 K with an activation energy E_a = 1.4 eV (Fig. 5.6b, black line). The desorption from low coordinated Pt atoms is found to be dominant which is a typical behavior that is encountered with small clusters. This result shows that contrary to non-structured surface (, *i.e.*, terraces), structured Pt surface presents stronger binding. A third peak is observed at 330 K which, by analogy with Pt/TiO_2,[148] can be attributed to CO desorbing from the Pt-(h-BN) perimeter sites such as edges of Pt clusters (or atoms) on h-BN. It is worth to mention that these desorption temperatures are close to the reported values for Pt on TiO_2.[148] The small desorption feature at lower temperatures, around 165 K, was found in all our TDS experiments. It has been observed before[185,186] and often ascribed to co-adsorbed CO molecules on water (that resides in the background pressure) which can desorb during water release.

Figure 5.6b (green curve) shows the CO TDS performed on the sample with the clusters partially intercalated beneath h-BN and whose STM image is shown in Figure. 5.4c. The desorption leads to a very small and broad peak centered at 400 K and shifted by almost 100 K compared to the non-intercalated system. The low peak intensity is attributed to the quenching of CO adsorption on the intercalated Pt because of h-BN which acts as a barrier against molecular adsorption. Only few remaining clusters on the surface can contribute to the desorption. The reduction in the CO desorption temperature is caused by the Pt intercalated species that modify the intrinsic influence of the h-BN/Rh(111) support on the non intercalated Pt clusters as a result of substrate effect and charge redistribution. A more detailed investigation on this result will be reviewed in chapter 7.

The h-BN/Rh(111) surface is inert towards CO oxidation; that is what we show experimentally in Figure 5.7a, where 0.2 L of Oxygen $^{18}O_2$ (Red) is pulsed alternately with 0.1 L of $^{13}C^{16}O$ (Black) onto the h-BN/Rh(111). The sample is slowly heated with a typical heating rate of 1 K/s, starting at T = 150 K. During the heating process, the signal of interest $^{13}C^{18}O^{16}O$ (green) is recorded with the mass spectrometer. No increase above the signal background was monitored. We only observe a broad CO desorption peak located at 260 K, in agreement with the above TDS of the clean h-BN (Fig. 5.6a). This finding defies some DFT calculations which predict that defected free standing h-BN can be catalytically active towards CO oxidation.[187] It should be noted that the sensitivity of the mass spectrometer provides a detection limit as low as 1×10^8 molecules/cm^2.s.

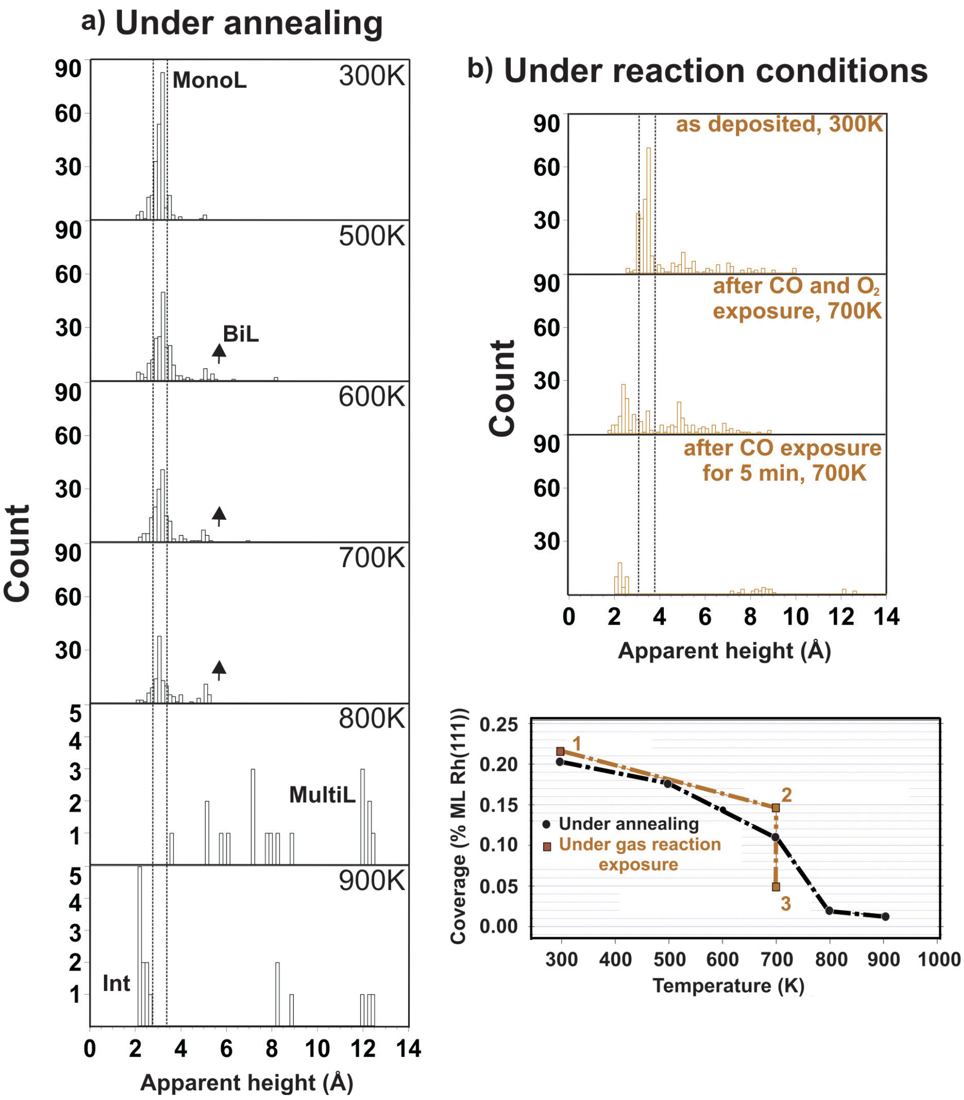

Figure 5.5 – Pt$_7$ stability on h-BN/Rh(111) showing ripening: (a) apparent height histogram corresponding to the STM images in Figure 5.2, upon annealing between 300 and 900 K. (b) apparent height histogram that corresponds to the STM images in Figure 5.4 upon exposing to CO oxidation reaction conditions. (c) Pt$_7$ density evolution under annealing and under reaction gas exposure. Annealing as a function of temperature gives rise to a second peak at 5.2 Å accompanied with a decrease in the cluster density without any shift in the initial size distribution (3.2 Å), indicating Smoluchowski ripening until intercalation beginning at 900 K. Exposing Pt to the reaction gas accelerates the intercalation process already at 700 K. MonoL : Monolayer structure, BiL : Bilayer structure, MultiL : Multilayer structure, Int : Intercalated.

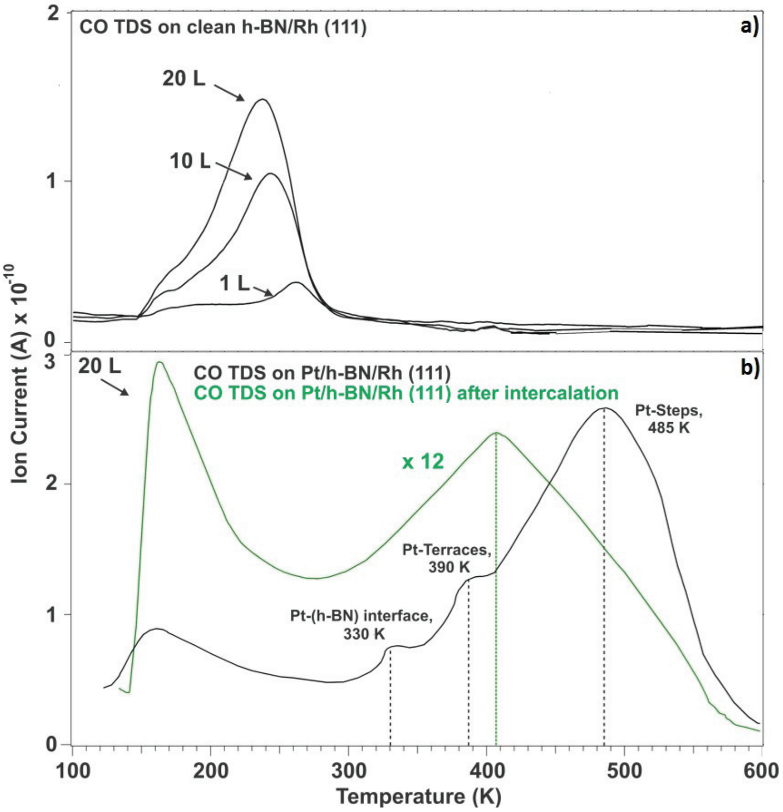

Figure 5.6 – TDS after adsorption of 20 L of CO at 120 K on (a) clean h-BN/Rh(111) where CO desorbs from defects at T = 260 K and shifts to 230 K at high coverage, (b) Pt/h-BN/Rh(111), as deposited and after partial Pt intercalation of the sample imaged in Figure 2c. CO exhibits 3 desorption peaks at 330 K, 390 K and a dominant peak at 490 K. The peak appearing at low temperature represents the desorption from coadsorbed water. TDS from the sample experiencing partial Pt intercalation (green) is magnified 12 × for better view.

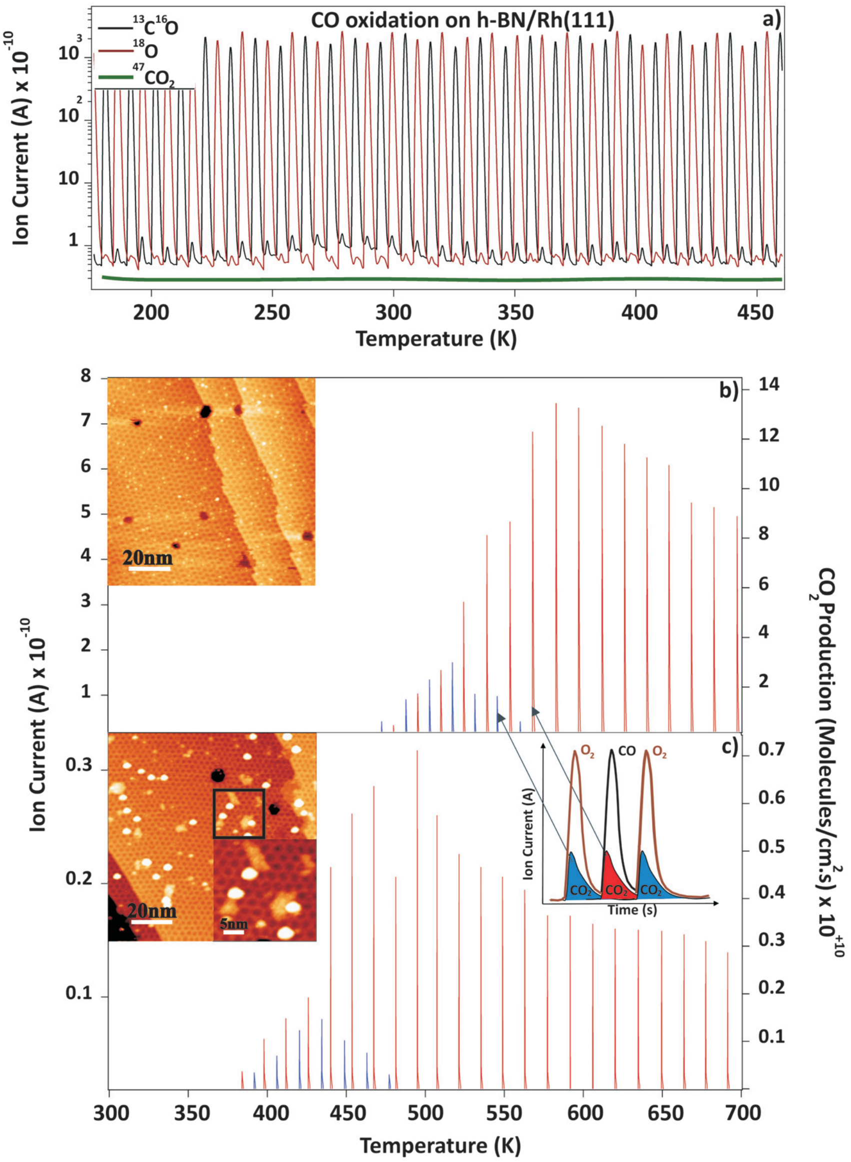

Figure 5.7 – (a) CO$_2$ production (green) obtained on clean h-BN/Rh(111) upon dosing alternating pulses of O$_2$ (red) and CO (black) as a function of the sample temperature and time (heating rate 1 K/s, pulse frequency 0.2 Hz). (b) CO$_2$ production obtained on the sample whose STM image is displayed in the inset (same conditions as in a). Red and blue colors refer to the CO$_2$ production synchronized with CO and O$_2$ pulses, respectively. (c) CO$_2$ production obtained on the sample whose STM image is displayed in the inset and which presents intercalated Pt under h-BN. This sample was kept for 5 min at 700 K while exposed to 60 L of CO. The temperature of CO$_2$ production is reduced by 100 K and the intensity is 20 fold lower.

Figure 5.7b displays the CO_2 production on the Pt_7/h-BN/Rh(111) surface of the sample whose STM image is shown in the inset, as a function of temperature. $^{13}C^{16}O$ and $^{18}O_2$ were pulsed alternately onto the surface while $^{47}CO_2$ was recorded. The amount of the dosed O_2 gas is two fold higher than that of CO because the sticking probability of oxygen on Pt is a half compared to CO. It is worthy to mention that, an increase in the O_2/CO ratio should increase the rate of CO oxidation on Pt-group metals.[188] Three regions in the graph of Figure 5.7b need to be commented. The region extending from 300 to 460 K is related to the CO poisoning in which no CO_2 production is recorded which is typically observed for Pt at low T. In this case, the catalytic reaction depends on the balance between sites of occupation, where the O_2 active sites are blocked due to the CO saturation of the Pt surface at low temperature. This saturation is a result of strong CO-Pt cluster binding. So, the desorption temperature depends on the strength of the CO binding to the Pt atoms. This indicates that the catalytic reaction follows a Langmuir-Hinshelwood mechanism where oxygen as well as CO has to adsorb on the surface to enable the catalytic process via adsorption. As soon as the temperature increases, CO starts to desorb leaving empty sites for O_2 occupation and the first CO_2 signal starts to rise. This latter (in blue) is synchronized with O_2 pulses. The pulsed O_2, then reacts instantly with the abundant CO on the Pt surface. That is what is called the CO rich region. The region above 520 K (Fig. 5.7b), known as O_2 rich region, contains CO weakly bonded to the catalyst at elevated temperature. Therein, the CO_2 production is synchronized with the CO pulses (in red) which reacts instantly with the abundant O_2 on the Pt cluster surface. The maximum CO_2 production is observed at 580 K in the oxygen rich regime and is estimated to 0.05 CO_2 per Pt atom, a slightly higher than that reported on the Pt clusters supported on TiO_2 (0.03 CO_2 per Pt atom).[189] Above 580 K, the catalytic activity decreases because the temperature is too high for the CO molecules to stay on the surface in the reaction time window. From this, it can be concluded that the Pt clusters supported on h-BN/Rh(111) cannot be considered as pseudo-free and that the support effect should be taken in consideration.

In Figure 5.7c, the CO_2 production on the $Pt_{27<x<74}$/h-BN/Rh(111) that has undergone partial intercalation, and whose STM image is shown in the inset, shows a behavior similar to what is observed for the non-intercalated Pt (Fig. 5.7b) but with very low intensities (by 20 fold). The decrease in the intensity indicates that the intercalated Pt catalytic activity is quenched by h-BN which acts as a barrier against gas adsorption under the present conditions of pressure and temperature. Only few remaining clusters on the surface contribute to the reaction. In fact, the screening behavior of the h-BN was recently reported for low gas pressure and high h-BN coverage.[190] Besides, we have performed in another experiment, presented in chapter 6, CO adsorption and oxidation reaction on a fully intercalated Pt clusters in which no adsorption or reaction was observed. The striking result here, with such few clusters on the h-BN, is that the CO oxidation temperature is reduced by almost 100 K. The reaction starts at 375 K and the poisoning is reduced as well. In fact, the Pt clusters are no longer supported by h-BN/Rh(111) alone but by h-BN/Pt/Rh(111). This is supported by STM (inset of Figure 5.7c) in which most of the non-intercalated Pt particles are located on top of the intercalated features. The maximum CO_2 production is observed at 490 K in the oxygen rich regime and is estimated to 0.02 CO_2

per deposited Pt atom. This is 2.5 fold less reactive than the non-intercalated Pt catalysts.

5.3 Conclusion

We reported on the stability and CO oxidation of Pt_7 clusters supported on h-BN/Rh(111), correlating the catalytic reactivity to the cluster stability and size before and after catalytic reaction. We found that the Pt clusters undergo partial intercalation after being exposed to the reaction gas, changing the catalytic behavior of the catalyst and reducing the reactivity due to h-BN screening which acts as a barrier against molecule adsorption onto the intercalated Pt. For the non-intercalated Pt clusters, the CO oxidation reaction starts at 480 K and follows the LH mechanism. For the Pt clusters that are adsorbed on the h-BN just above the intercalated Pt, the onset reaction temperature is shifted by 100 K towards lower temperatures.

6 Pt_7 on h-BN/Rh(111): energetic deposition and thermal stability

Supported small Pt clusters are effective as model catalysts for many catalytic reactions. The support plays a determining role on the final structure and reactivity of the catalyst. In this chapter, we report on the cluster-surface interaction of Pt_7 and h-BN/Rh(111), using STM and TDS for measuring CO oxidation reaction. The h-BN monolayer, was irradiated by a Pt cluster beam with kinetic energies E_k = 1.2 (soft landed), 30, 60, 100, 170, 314 and 416 eV/atom. The results show that even irradiation at 30 eV/atom can lead to non thermal cluster intercalation. The intercalated particles are found to settle under the h-BN wire sites above the Rh(111) crystal with induced visual surface defects for E_k exceeding 100 eV/atom. Furthermore, we studied the thermal stability of the intercalated Pt clusters for different annealing temperatures and also under gas reaction, *i.e.*, with exposing to CO and O_2 gases. TDS was used as probing technique to investigate the CO adsorption sites on the intercalated elements prior to CO oxidation reaction. Annealing the irradiated samples can lead to Pt agglomeration and defects healing. The platinum stay fully covered with h-BN which acts as a protective layer against CO penetration and adsorption on the intercalated species under ultra high vacuum.

6.1 Introduction

Clusters made of few up to thousands atoms are used as models to understand the fundamentals of physics bridging the gap between the bulk and the atomic scale of materials. The cluster-surface interaction depends on the cluster impinging kinetic energy. If this energy exceeds the cohesive energy between the atoms, the clusters could disintegrate on impact and the constituents become implanted, producing defects in the target. In the case of low kinetic energy, the clusters should, only, be soft landed or pinned on the substrate. Ion implantation is an effective and well developed tool for surface modification and material processing.[191–194] The impact of the implantation depends on the material chemical and physical properties and on the implant parameters such as ion beam energy, type of implant and ion current density. Since its first use by Yamada,[195,196] cluster implantation is favored upon ion beam implantation due to both low-energy and high-current features to meet small device scale shrinking demand, in addition to the large amount of mass and energy density per single charge that can be transported.[38,197] Energetic cluster irradiation is mainly used for doping of shallow layers, dry etching, cleaning and surface smoothing. High atomic density and low energy deposition at a local area are important characteristics of the irradiation by cluster ions in which the penetration range is much shallower, and where displacements remain tightly concentrated within the impact region at the target surface.[198,199] An exclusive cluster beam application range review can be found in ref.[200] In this work, the material under discussion interacting with the cluster beam is h-BN supported on Rh(111). The submerging of supported 2D nanomaterials layers such as graphene and h-BN is tremendously promising as these single layer structures exhibit novel and well established properties for many industrial and research applications. Driven by heat or gas co-adsorption, intercalation and trapping of variety of species (Co, Au, He, and H) beneath h-BN have been observed.[119,201–203] The related species penetrate, through defects, in between the h-BN and the support where they stabilize. Intercalation, under high pressure, of small molecules (CO, O_2, and H_2O) on both graphene and h-BN has, also, been observed.[26,204,205] Intercalation can, interestingly, affect the support properties in many ways. For example, Ge intercalation leads to decoupling of graphene and h-BN from their metallic substrate and formation of quasi-free-standing graphene and h-BN monolayers on Ge.[206] Very recently, ion implantation was performed on h-BN and graphene which leads to structural defects creation and ions intercalation. For instance, projected Ar^+ ions where found to be trapped beneath the wire crossings of h-BN and stabilized at room temperature.[11,141,142] Similarly, Rb ions penetrate the h-BN and settle beneath the wires regions when accelerated with a 100 eV kinetic energy.[12] Moreover, ions implantation on h-BN can lead to local structural change from h-BN to c-BN (cubic boron nitride phase) when bombarded with B ions.[207] Irradiation of graphene/Ir(111) interface with high energies (from 1 keV and up) results in the formation of line like depressions induced by the ion channeling within the interface. However, lower energies result in simpler defects such as vacancies.[208] In this contribution, we extend those works by studying ${Pt_7}^+$ cluster impact on h-BN/Rh(111) with various kinetic energies and using STM and CO TDS to investigate their subsequent catalytic activity.

6.2 Results and discussion

6.2.1 Pt clusters-surface interaction

The h-BN surface was exposed to ${Pt_7}^+$ clusters with kinetic energies E_k = 30, 60, 100, 170, 314 and 416 eV/atom as shown in Figure 6.1a-f, respectively. The STM images show bright protrusions with an average apparent height of 2.2 Å located at the h-BN wire regions in contrast to the soft landed Pt (upper inset of Fig. 6.1a) in which the clusters are sitting inside the h-BN depressions with a nominal apparent height of 3.2 Å (see chapter 5). A similar phenomenon has been observed for h-BN/Ar^+/Rh(111)[11,141] where the Ar ions penetrate the h-BN monolayer and stay underneath above the Rh(111) surface. For the mentioned kinetic energies, the protrusions are located around the h-BN depressions, particularly where the wires are crossing. The lodging of the Pt clusters under the h-BN can also be confirmed from TDS mea-

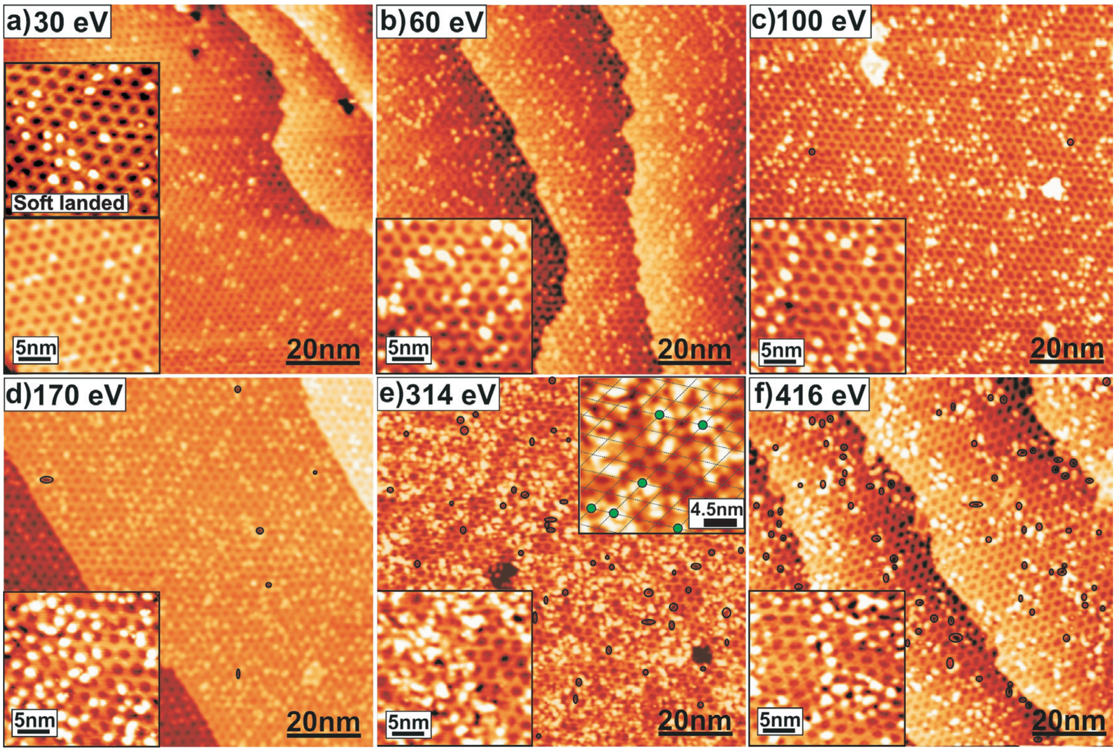

Figure 6.1 – Overview STM images of Pt_7 clusters deposited on h-BN/Rh(111) at (a) 30 eV, (b) 60 eV, (c) 100 eV, (d) 170 eV, (e) 416 eV/atom. The images show intercalation of Pt under h-BN and its stabilization under the wire regions. Cavities (circled black points) induced by the collision cascade in h-BN start to appear barely at 100 eV/atom and their density increases with increasing the projectile energy. The green circles, in the inset of image (e), indicate the protrusions that occupy the under depression zones Deposition temperature = 300 K, imaging temperature = 80 K.

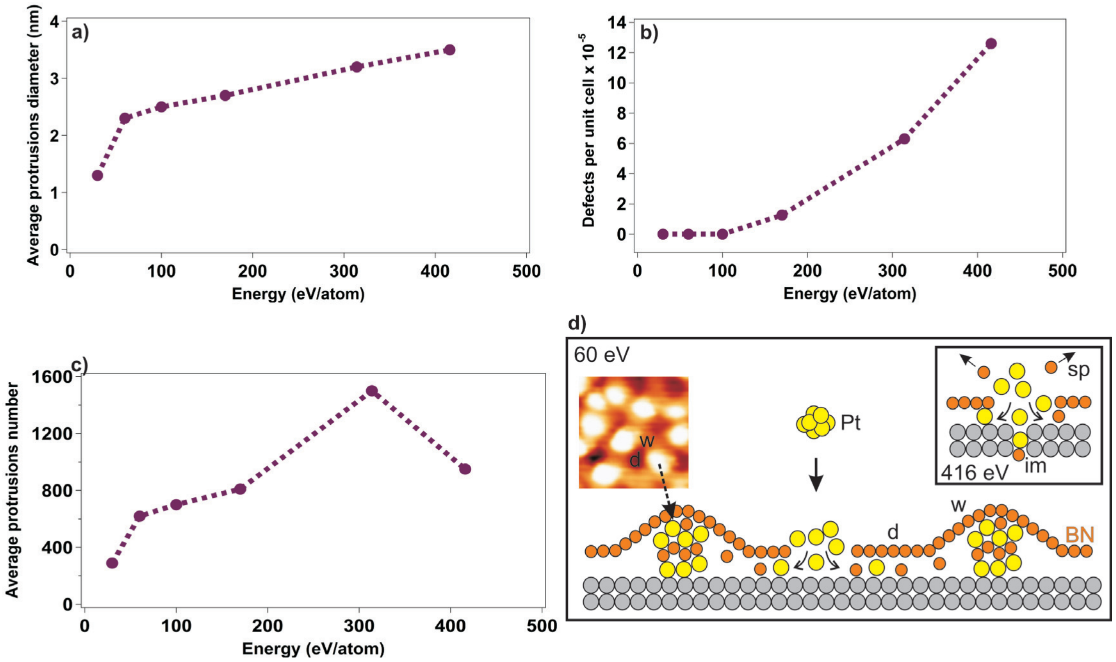

Figure 6.2 – Analysis on Pt_7 clusters after the impact, extracted from STM images, as a function of clusters energy. (a) average apparent protrusions diameter. (b) density per h-BN unit cell of visual induced defects (already targeted by black circles). (c) average counted protrusions per 100 x 100 nm^2. (d) schematic presentation of energetic Pt interaction with h-BN/Rh(111) showing intercalation process and protrusion formation for E_k = 60 eV/atom as well as implantation and sputtering for E_k = 416 eV/atom. w: wires, d: depressions, sp: sputtered and im : implanted.

surement which shows only desorption from h-BN (as it will be shown hereafter). Therefore we conclude that the h-BN shelters the metal clusters everywhere in Figure 6.1 where the bright protrusions refer to the non thermal intercalated Pt and h-BN defects created during impact.

The impacts of irradiated Pt_7 clusters at 170, 314 and 416 eV/atom on the surface are visible in Figure 6.1d-f where the STM images show the surface just after cluster bombardment. Cluster-induced defects are visible as cavities randomly distributed over the whole surface (indicated by black circles). For these energies, it is expected that the clusters get in contact with the Rh(111) substrate as well. Exposing graphene/Ir(111) to energetic Xe^+ or Ar^+ beam leads to formation of defects[209] comparable to what is obtained in our experiment. The robust B-N sigma bond, which is inert towards chemical attack, is a strong covalent bond with a short bond length and a high bond dissociation energy of about 6 eV.[210] It needs very high energetic clusters to be broken. Accordingly, increasing the impact energy amplifies the number of defects on the surface which start to appear barely at 100 eV/atom and their number increases from 1.2×10^{-5} ML to 1.2×10^{-4} ML at 416 eV/atom (Fig. 6.2c,f). These vacancies or cluster defects are related to B and N knocked out during Pt cluster penetration. A glance at the protrusion density reveals that the coverage is twice higher when the energy is increased to 60 eV/atom compared to that of 30 eV/atom. This step-up in the density persists with increasing the cluster energy which can be associated to cluster fragmentation after collision cascade with h-BN and the underlying Rh substrate or/and contribution of ejected N and B defects. This density was plotted in Fig. 6.2c and it monotonically increases as a function of the irradiation energy until it declines again for E_k = 416 eV/atom. We can explain this decline by an increase in the probability of detached B and N as well as Pt fragments being pushed beyond the h-BN surface into Rh(111) and/or sputtering of BN species to the vacuum. Figure 6.2d gives a schematic presentation of Pt_7 interaction with h-BN/Rh(111) at 60 and 416 eV/atom. At relatively lower energy, the clusters penetrate the h-BN layer ejecting, in their ways, BN species which diffuse with the Pt beneath the h-BN to the wire regions forming the protrusions seen in the STM. At relatively high energy (416 eV/atom), the cluster impact with h-BN induces species intercalation into Rh(111) accompanied by B-N sputtering.

A close examination of the STM images in Figure. 6.1e,f reveals that some protrusions occupy the under depression zones. The inset at the right upper corner of Figure. 6.1e displays some of these protrusions (marked by green cirlces). It can be stated that, at room temperature, when the deposition energy is relatively low, the Pt clusters do not stick to their impact sites but move further beneath the surface before they get stabilized at their favorite sites (under wire). Nevertheless, for E_k = 314 and 416 eV/atom, the impact energy is sufficiently high for the clusters to get implanted into the substrate in such a way that leaves them restrained at their landing sites (under depression). To further extend our analysis, the relation between protrusion size and the cluster energy was investigated and is displayed in Figure 6.2b. As a matter of fact, the apparent protrusion lateral size is found to increase with energy. This growth in lateral size may be due to a continuous supply from N, B and Pt species since their number should grow with impact energy. At the same time, no significant increase in the vertical size could be measured. One should take into consideration that supported h-BN is not as uniform and regular as, for example, graphene, making it difficult to clear up relatively small height variation.

Figure 6.3 shows the STM images of the same samples whose images are shown in Figure 6.1, after being exposed to CO and O_2 gases from 150 K to 650 K in the context of performing CO oxidation reaction. Two phenomena can be observed. First, the h-BN layer has undergone rearrangements which facilitated the reconstruction after the damage. As it can be seen, the cavity defects induced by collision with $E_k > 100$ eV/atoms disappeared after annealing under gas reaction leaving behind an h-BN layer with no visual defects. The knocked-out N and B atoms, trapped in the interlayer region after impact, should be able to recombine easily. Recent studies[209,211] have found that annealing the damaged sample to 1000 K can restore the initial graphene lattice. Second, the number of protrusions, drastically, decreased while their area increased, indicating that the aggregation of Pt under h-BN is much more facile. This considerable decline in the protrusion population is a clear indication that a large fraction of them is made of defects which disappear once annealed. In addition, the intercalated species do not populate the sub wires locations only, but they gather, mainly,

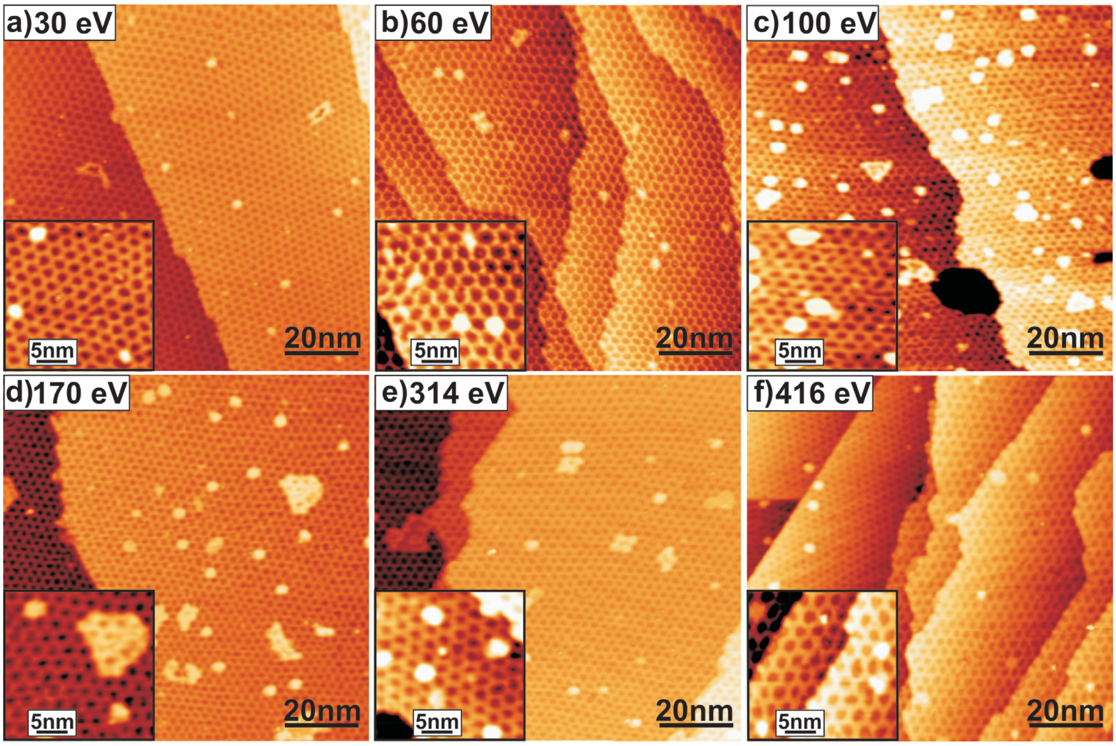

Figure 6.3 – Overview STM images of the samples whose images are shown in Figure 6.1, after being exposed to catalytic reaction conditions. The images show agglomeration of intercalated Pt under h-BN, and self-healing of cavities that were observed before. The protrusions are barely found under the wire regions. Instead, most of them are now located under the h-BN depressions.

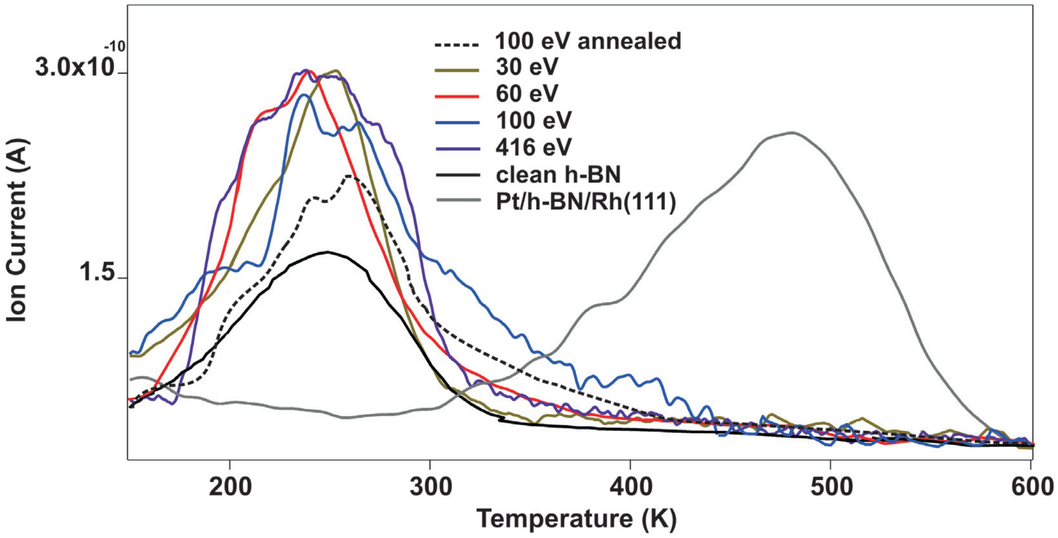

Figure 6.4 – CO TDS on intercalated Pt in h-BN/Rh(111) at various kinetic energies of the samples presented in Figure 6.1 a, b, c, f, with CO TDS on clean h-BN and Pt/h-BN/Rh(111) added for comparison. The dashed black line refers to CO desorbing from the sample irradiated with E_k = 100 eV/atom and then annealed to 600 K under gas exposure.

under the depression regions and the nanostructure becomes lifted off which refers to a strong agglomeration below the h-BN depressions. Moreover, we observe that not all the protrusions are restrained to the depressions but some of them, relatively larger in size, expand also under several h-BN unit cells and, sometimes, adopt the h-BN moiré with 2.2 Å apparent height. These large protrusions are found to grow in number when the sample is further annealed to higher temperatures as it will be shown later.

6.2.2 CO temperature desorption

Almost all the intercalated clusters, as shown in Figure 6.3, under the depression regions present an average apparent height of 3.2 Å (see apparent height histogram in supporting information (Fig. A.1)) which corresponds to that of a flat Pt_7 cluster sitting above the h-BN (as seen in chapter 5). However, below the depressions, the h-BN is located at 2.2 to 2.5 Å above the Rh(111) and interacts strongly with the Rh leaving no much space for deformation. This raises the question whether the catalyst breaks again the sp^2 bond and rebounds to the surface. To elucidate this phenomenon, the CO TDS was used as a probe for monitoring the presence of Pt above the h-BN surface. Figure 6.4 shows thermal desorption spectra related to the varying deposition energies. It is found that the dosed CO, at a surface temperature as low as 150 K, desorbs promptly at 250 K when the deposition energy is higher than 30 eV/atom. This value lies at the same interval of the CO desorption temperature from the pristine h-BN/Rh(111) where the maximum desorption occurs at 230 K. So, the observed desorption is linked to the h-BN intrinsic defects formed during pyrolysis growth, more precisely from nitrogen vacancies.[212,213] . Single nitrogen and boron vacancy (V_N, V_B) defects can exist in h-BN with V_N more stable than V_B.[128] Thus, the V_N vacancies are more likely to be observed than the boron vacancies in coherence with experimental findings.[214] Upon increasing the deposition energy, a considerable enhancement of the desorption signal takes place. Besides, the main peak splits gradually into 3 main peaks positioned at 210 K, 240 k and 260 K with an activation energy E_a = 0.54, 0.64 and 0.69 eV, respectively. We attribute these values to the desorption from B-vacancies (210 K), N-vacancies (240 k) and BN-vacancies (260 K). This is because the defects induced by the clusters in h-BN increase with increasing the deposition energy leading to much higher CO desorption fraction from these defects with nitrogen vacancies being the dominant ones, which is consistent with the work of Jiménez et al. who found, using ion bombardment, a large concentration of nitrogen type defects.[207] When performing CO desorption on the sample irradiated with E_k = 100 eV/atom and then annealed to 600 K under gas exposure, the desorption intensity is found smaller and the contribution of the CO desorbing from BN vacancies predominates. This is expected, as annealing reduces the density of single defects while the double vacancies become so abundant because B and N diffuse and recombine easily in order to lower their total energy. Therefore, the disappearance of the desorption peak at temperatures above 300 K, in the case when h-BN is irradiated with Pt clusters before and after annealing (dashed black line), excludes the possibility that Pt is laying above h-BN (see desorption from soft landed Pt on h-BN/Rh(111)). Thus, the h-BN top layer acting as a barrier keeps the intercalated species trapped underneath even after annealing. Accordingly, using accelerated Pt on a continuous h-BN layer supported on Rh(111) as a catalyst should be considered inadequate for CO oxidation reaction. It should be noted that no obvious effect of gas reaction on the Pt under h-BN was sensed.

6.2.3 Intercalation stability

Further annealing, without gas reaction, at 800 K was carried out to investigate the intercalated Pt behavior under higher temperature. Figure 6.5 a-e display the STM images, for each deposition regime, after annealing at 800 K. The deposition energy does not seem to have an effect on how the intercalated Pt behaves under high temperature. In all the cases, the Pt clusters undergo a massive diffusion under the h-BN. Most of the Pt that were, previously, located under the h-BN depressions randomly segregate under the depression and wire sites giving rise to the formation of large intercalation areas. The step-height of these layers was found to be 2.2 Å which, roughly, corresponds to that of a monoatomic Pt step. Gruber and coworkers, also, reported a 2D growth mode for an epitaxial growth of Pt on the Rh(111) surface at 700 K. Therefore, we conclude that only 2D Pt structure is present under the h-BN. We propose here that the above discussed protrusions with 3.2 Å are 3D Pt mold clusters which after annealing at 800 K expand laterally adapting a 2D structure. However, it should be noticed, that some of those protrusions with 3.2 Å confined at the depression sites, survived the annealing. It can be suggested that the confinement and high stability of Pt under a non favorable site (under depression) could be an effect of defect rearrangement. For instance, such defects induced by Ar^+ bombardment, when annealed, were found to assemble at the h-BN rims and get around

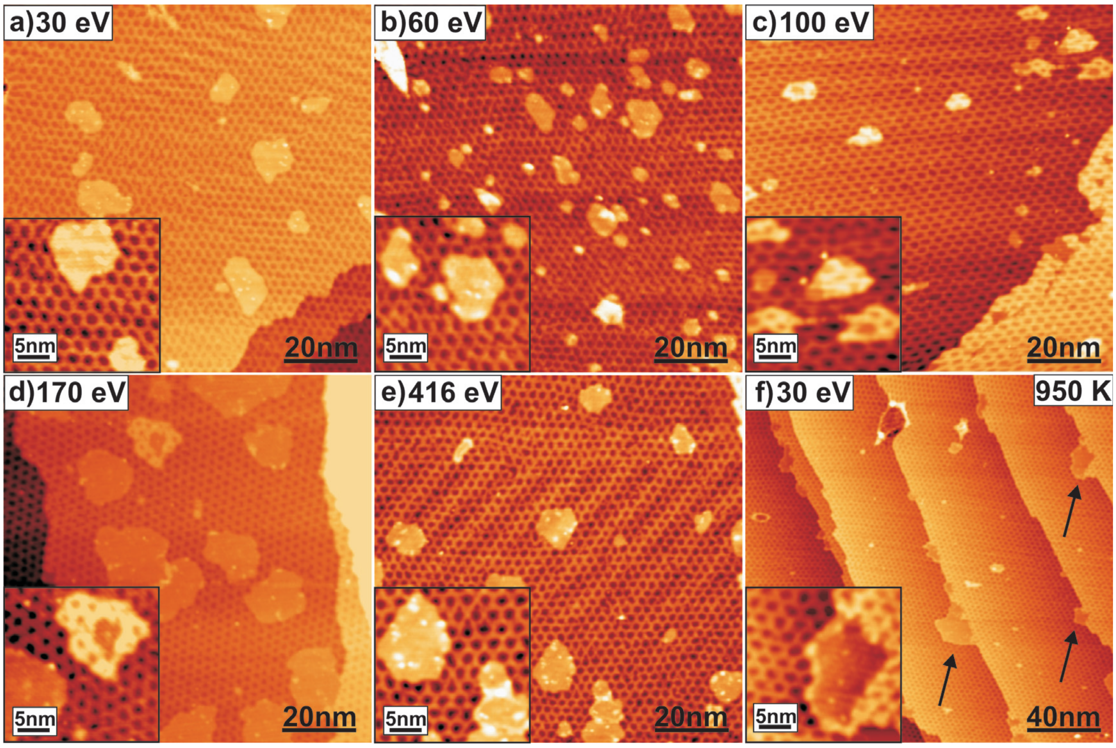

Figure 6.5 – Overview STM images of intercalated Pt_7 clusters under h-BN in the samples whose STM images are given in Figure 6.3, after annealing at 800 K (a-e). The intercalated Pt get more and more flatten and larger beneath the h-BN, compared to that in Figure 6.3. Further annealing to 950 K leads to the diffusion of the intercalated Pt to the Rh (111) steps as indicated by arrows (f).

where the bonding to the rhodium substrate is stronger.[142] Therefore, our Pt clusters could be trapped under the depressions by the electronic clouds of the agglomerated neighboring B and N defects around the h-BN rims.

Both intercalations where the periodicity of h-BN on top was conserved and where h-BN became flat were observed. Flat structure and flattening were observed in the case of h-BN grown on Pt(111)[139] and hydrogen intercalation.[138] This is explained by the weak interaction between h-BN and Pt (111). Thus, bonding through intercalation may remove the corrugation nature of h-BN leading to a flat state. That is what is observed in Figure 6.5; the regions where the Pt clusters are embedded become flattened. Nevertheless, it is very puzzling to find that some intercalated h-BN regions are commensurate with the pristine h-BN lattice keeping their corrugation structure and the periodicity on top similar to the surrounding periodicity. Rhodium and platinum have nearly the same atomic size as well as the metal bond energy. Thus, post annealing is expected to form some Pt-Rh surface alloy or can induce segregation of Rh to the surface. Rh segregation in Pt-Rh alloys is a well-known process but it is unlikely that Rh atoms segregates in a Pt rich surface at a temperatures below 800.[215,216] Therefore, we can rule out the possibility of such process to occur at our annealing temperature. One possible explanation could be that Pt, in some regions and because of the energetic impact, is tightly bound to Rh which inhibits Pt to occupy only positions favorable for adsorption. Thus, the variation in the bonding strength between favorable and unfavorable adsorption sites gives rise to the observed corrugation.

The Ostwalder group reported in their study on graphene and h-BN bombarded by Ar^+ ions what is called a can opener effect.[217,218] This effect emerges from B and N in the case of h-BN and from carbon in the case of graphene that are knocked out during ion implantation after annealing the sample to high temperature (1000 K for graphene and 900 K for h-BN). These defects become mobile and gather at the rim of the depressions due to minimum energy costs. As a consequence, detachment of 2 nm depression areas was reported leaving empty homogeneous voids of 2 nm width on the h-BN surface. In the present experiment (Fig. 6.5f), this phenomenon was not observed. Instead, annealing the sample to 950 K leads to the diffusion of the intercalated Pt into the h-BN (or Rh(111)) steps and stabilization.

6.3 Conclusion

Mass selected Pt_7 cluster interaction with h-BN/Rh(111) surface for CO oxidation reaction was studied using STM and CO desorption spectroscopy as probing techniques. Exposing h-BN to Pt clusters with kinetic energies above 30 eV/atom leads to non thermal cluster intercalation under the h-BN. The intercalated Pt atoms and clusters are site selective as they settle only under the h-BN wires. Visual induced defects start to appear at an energy above 100 eV/atom. Annealing to 600 K under CO and O_2 gas leads to defect healing and Pt exiting the wire sites to stabilize under the h-BN depression sites. Further annealing at 800 K leads to the agglomeration of the intercalated Pt and to h-BN flattening. No can opener effect was observed even when the annealing temperature reached 950 K. Instead, the intercalated Pt are found to diffuse and stabilize at h-BN/Rh(111) steps. Exposing the energetic Pt under h-BN to CO TDS exhibits the same pattern analogue to CO desorbing from the h-BN surface defects, indicating that Pt are below a protective h-BN layer that inhibits CO adsorption to the underlying particles under the studied pressure and temperatures. Therefore, the Pt clusters intercalated with relatively higher kinetic energy in h-BN/Rh(111) are inactive for CO oxidation reaction under the studied conditions.

7 Pt_7 on h-BN/Rh(111): Effect of Pt intercalation on CO poisoning

Poisoning, in general, quenches the low temperature catalytic activity. For instance, a large amount of harmful gas emission is released during the first minutes of car engine ignition before the catalyst can warm enough and become useful. Small Pt clusters are vulnerable to CO poisoning as well. This chapter deals with Pt surface interaction with h-BN/Rh(111) that was found to play an important role on how CO binds to Pt. This was motivated by the observation reported in chapter 5 which highlighted the reduction in CO oxidation temperature when Pt undergoes partial intercalation, suggesting that this intercalation could be a key factor in the observed effect. Based on the results of chapter 6, we propose a method on how CO binding to soft landed Pt_7 catalyst supported on h-BN/Rh(111) can be reduced through the introduction of an intercalated Pt layer between h-BN and Rh(111), using energetic Pt cluster beam irradiation. The intercalated layer was produced using successive energetic deposition and annealing. Upon annealing, the intercalated Pt species were found oriented along the h-BN depressions and the soft landed Pt_7 clusters show remarkably high thermal stability up to 800 K. TDS of CO shows that the desorption temperature on the soft landed Pt_7 can be tuned by the introduction of an intercalated Pt clusters under the h-BN monolayer.

7.1 Introduction

Catalyst deactivation is a major concern in chemical industrial processes where activity and selectivity quenching overtime costs billions of dollars to replace the decayed catalyst. The science of catalyst deactivation has expanded considerably,[56] providing knowledge for designing stable catalysts to prevent or slow down catalyst deactivation. The major causes of deactivation are basically chemical, mechanical or thermal.[219–221] Poisoning, for example, is a chemical deactivation mechanism and is considered as one of the worst catalyst deactivating process. It is known to occur in heterogeneous catalysis, in which the activity depends critically on the free sites available on the catalyst for reactant adsorption and reaction. Thus, poisoning can hinder the reaction by blocking the active sites as a result of strong adsorption of the reactants, products or impurities on the catalyst. Pt catalysts are extensively used in chemical industry and in fuel cells[222,223] and the binding strength of some species, such as carbon monoxide (CO) is primarily responsible for Pt catalyst deactivation. The strong binding of CO to Pt is due to the strong interaction and hybridization of CO s and anti π bands to the Pt d band.[224–226] A comparative study between clusters, monolayer and bulk Pt, showed an enhancement of adsorption on the clusters over bulk.[227] Thus, the excessive binding strength of CO may lead to more reactive catalytic activity but, at the same time, can increase the poisoning temperature. Alloying Pt with other metals is known to weaken the CO binding thus reducing poisoning.[228,229] Additionally, the support can, also, have considerable effect on how CO binds to the catalyst. For example, Pt supported on tungsten carbide was found to be less poisoned by CO compared to Pt/C.[230] In fact, the tungsten carbide support compared to traditional carbon supported Pt catalysts could impart much stronger negative electronic charge to Pt through an electron donating effect which, consequently, reduces CO binding strength.[230] Moreover, computational calculations show that graphene support makes the Pt catalyst capable of losing electrons and thereby weakens CO adsorption.[225,231] Adsorbed CO on Pt clusters supported on Ru were found to displace from Pt, through spillover, to the Ru support, hence continuously providing new free sites of adsorption.[232] Therefore, the adsorption of CO can be controlled using an appropriate substrate. In the present experiment, a novel method to reduce CO poisoning through building up a new catalyst configuration composed of Pt/h-BN/intercalated Pt/Rh(111) is proposed and CO thermal desorption spectroscopy was used to determine the desorption temperature on the catalyst.

7.2 Results and discussion

7.2.1 Combination of soft landing and energetic deposition of Pt clusters

Figure 7.1a,b show Pt_7 supported on h-BN/Rh(111) when the clusters are soft-landed with a typical energy of 1.2 eV per atom and when they are accelerated by an energy of 170 eV per atom. In the first regime, the clusters are sitting in the h-BN depressions at the edge sides and look bigger, compared to those observed in chapter 5, due to tip convolution. In the second case, the clusters are intercalated under h-BN and they shelter at the wire regions according to what was obtained in chapter 6. These observations incite us to combine the two regimes together to obtain soft landed Pt above the regions intercalated by Pt. Figure 7.2a-f display a combination between the preceding two states, in which Pt is on top and under the h-BN monolayer, using a sequence of energetic and soft deposition. To proceed, the sample related to Figure 7.1b was annealed at 800 K, then imaged as shown in Figure 7.2a. The diffusion of Pt under h-BN allows it to expand and produces large flake-like intercalated areas spreading under the moiré pattern. The apparent 2.2 Å height of these intrecalated features, measured from the STM height profile, indicates clearly that the annealed Pt remains entirely under h-BN.

Consecutively, the annealed sample of Figure 7.2a was exposed to a second irradiation with Pt beam of 170 eV/atom (In order to increase the density of intercalated areas) followed by a soft landing deposition. As one can observe in Figure 7.2b, the surface is covered with randomly

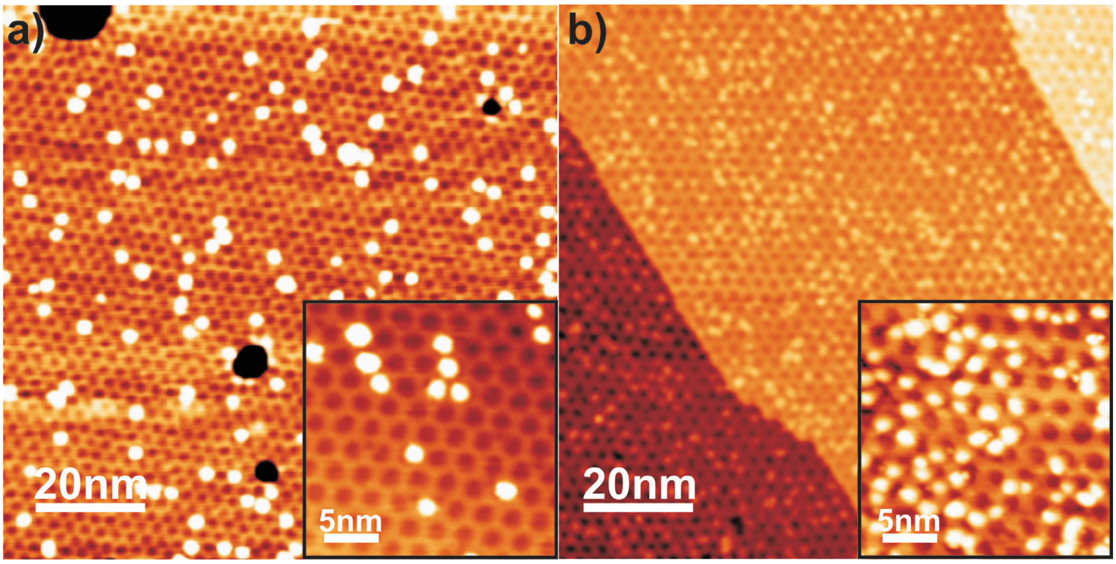

Figure 7.1 – Overview STM images of (a) Soft deposition, at 1.2 eV per atom, of Pt_7 on h-BN/Rh(111) showing Pt clusters as white protrusions landed in h-BN depressions. (b) Energetic deposition, at 170 eV per atom, of Pt_7 on h-BN/Rh(111) showing Pt as white protrusion housed under h-BN wires. The insets are magnified regions of their respective surface.

distributed Pt. Further, the sample was annealed again to 800 K and imaged as shown in Figure 7.2c. From this figure, one can notice that the density of the intercalated Pt clusters is increased with the appearance of particles in the form of white protrusions on top of them. These particles are Pt clusters brought by low energy (or soft-landing) deposition which remain on top of h-BN. As far as we repeat the previous energetic deposition; soft landing and annealing steps (Figure 7.2d,e), both the density of the intercalated Pt and those remaining on the top are found to increase. Figure 7.3c, illustrates the steps of producing Pt/h-BN/intercalated Pt/Rh (111) using a combination of energetic and soft deposition in conjunction with their respective apparent height histogram. After irradiating the h-BN/Rh(111) with the Pt clusters, the intercalation under the wire regions can be observed as shown in the schematic view of this figure. This sample is referred as EDe (Energetic Deposition). Adding annealing to EDe leads to a situation where the particles spread under the depressions and wire areas. This is named (EDe + annealing) step. The respective apparent height histogram in black shows a height of 2.2 Å. Intercalated Au under h-BN has been found to exhibit the same order of magnitude.[119] Contrary to the case of EDe, the soft deposition Pt (called SLDe) lands the clusters above the h-BN depressions. Combining all the steps together (EDe + annealing + SLDe) produce a situation in which a Pt/h-BN/intercalated Pt/Rh(111) configuration can be obtained. Related to this configuration, the apparent height (histogram in green), was found to be almost monosized at 5.2 Å. Since the apparent height profile is taken from the bottom of h-BN depressions and by considering an equivalent electrons density of state, the subtraction of 2.2 Å (apparent height of the EDe Pt) gives 3 Å which is not far from 3.2 Å. This matches the apparent height of the SLDe Pt on top of the h-BN (see the histogram in red) which could

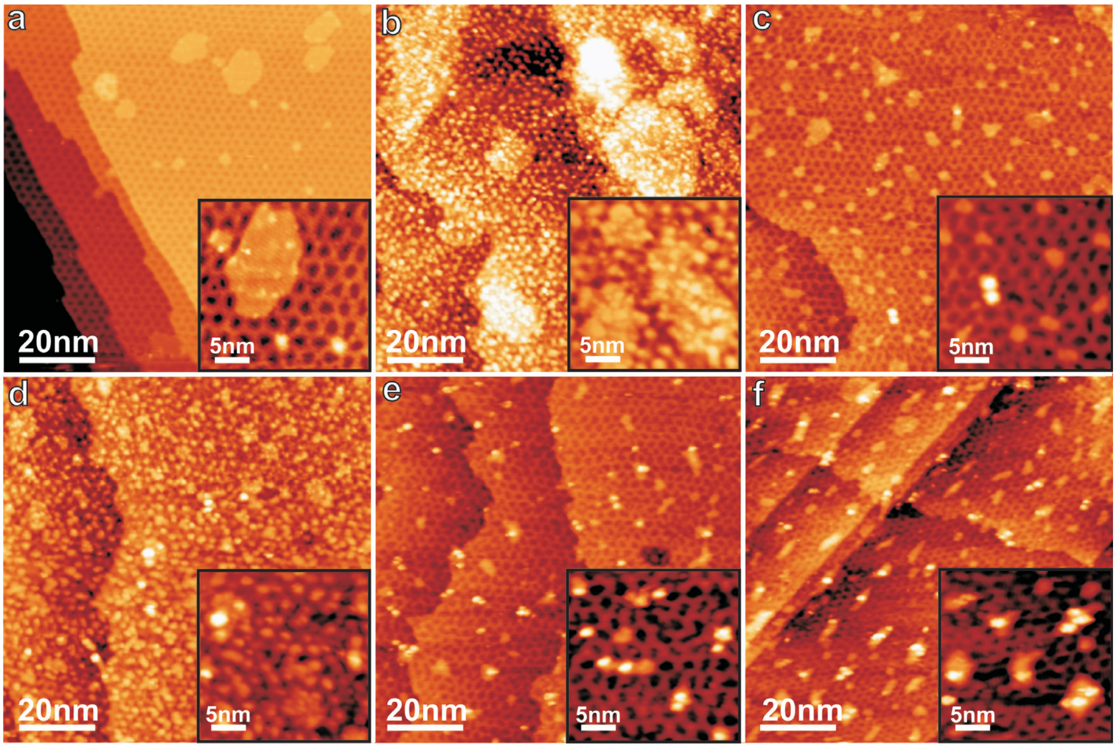

Figure 7.2 – Overview STM images of subsequent energetic and soft Pt$_7$ deposition on h-BN/Rh(111) at 170 eV/atom, followed by a deposition at 1.2 eV per atom (b, d). The image in (a) is taken on the sample of Figure 7.1b that was annealed at 800 K. (c, e, f) images of the samples annealed at 800 K. The images show the intercalation of Pt under the h-BN and stabilization under the wire regions as flakes-like features. The particles showing as bright protrusions in c, d, e and f are Pt particles on top of the intercalated Pt. Imaging was done with: V_t = -1 V and I_t = 100 pA.

indicate that the (EDe + annealing + SLDe) Pt clusters keep their initial size at deposition.

Moreover, even at high annealing temperature, adjacent soft landed Pt clusters (appearing as white protrusions) remain intact side by side as can be seen in the inset of Figure 7.2f. This means that the Pt particles remain stable up to 800 K which is an impressive result compared to soft landed Pt on h-BN/Rh(111) that were deposited at room temperature and annealed at the same temperature (see chapter 5), and where the annealed Pt clusters were found to agglomerate into larger particles with an apparent height of 8.3 Å. Furthermore, one can observe that the intercalated Pt particles orientate themselves in a specific manner, as shown in Figure 7.2f, where these particles appear as features elongated almost in the same direction. A closer inspection reveals that about 80 % of the intercalated Pt particles orientate themselves along the h-BN depressions.

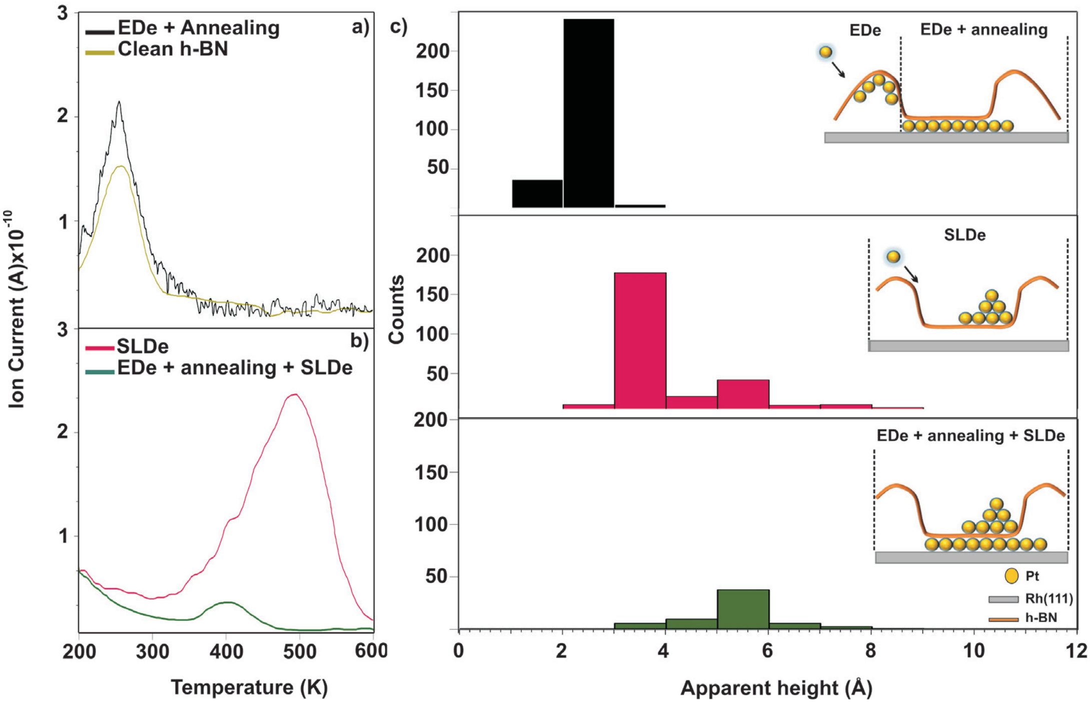

Figure 7.3 – CO TDS performed on (a) clean h-BN (yellow) and on energetic Pt deposited on h-BN/Rh(111), named EDe, and annealed at 800 K. (b) CO TDS on soft-landed Pt on h-BN/Rh(111) (named SLDe) together with CO TDS on EDe annealed at 800 K and followed by an SLDe, designed by (EDe + annealing + SLDe). (c) apparent height histogram deduced from STM images of EDe annealed at 800 K (black), SLDe (red) and (EDe + annealing + SLDe) (green). The schematic insets illustrate the configuration of EDe, (EDe + annealing), SLDe and (EDe + annealing + SLDe), respectively.

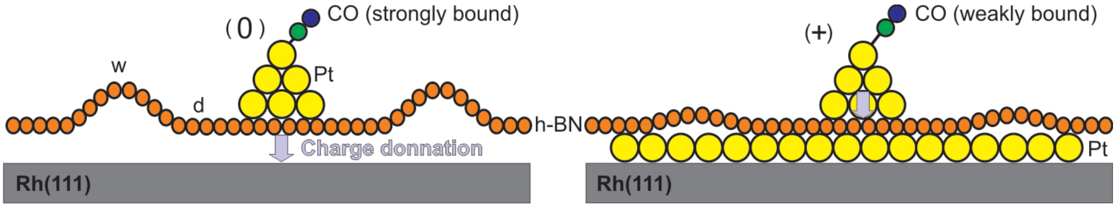

Figure 7.4 – Schematic overview showing CO binding to Pt clusters in the case when they are supported on h-BN/Rh(111) and in the case when they are supported on h-BN/Intercalated Pt/Rh(111). The w and d refer to wire and depression regions, respectively, and the gray arrow indicates the charge donation direction.

7.2.2 CO desorption temperature

Figure 7.3a,b show CO TDS measurement performed on the Pt/h-BN/intercalated Pt/Rh(111), *i.e.*, (EDe + annealing + SLDe) system. Measurement started with TDS on the EDe Pt, then on the SLDe sample, and finally on the Pt/h-BN/intercalated Pt/Rh(111) system. After fully saturating the surface with 30 L of CO gas at 150 K, the temperature was raised at a heating rate of 2 K/s until the desorption ceased. Figure 7.3a displays the CO desorption from the EDe Pt (in black) where one can observe a desorption peak at 250 K. The CO desorption temperature from the EDe Pt is similar to the desorption temperature from the clean h-BN surface (CO desorbs more precisely from h-BN defects). This, clearly, indicates that the CO is unable to access Pt under h-BN which acts as a barrier. On the other hand, the CO desorption from the SLDe Pt gives rise to a broad peak centered at 500 K, as shown in Figure 7.3b. The desorption temperature, above 500 K, is typical for CO desorption from Pt smooth steps,[148,233] as already shown in chapter 5. This high desorption temperature was found to result from a strong Pt-CO bond strength which inhibits large scale practical applications such as in fuel cells. It affects the reactivity of CO involved in catalytic reactions, depending on the nature of chemical bonding between the catalyst and reactants or intermediates. However, the CO desorption from the Pt/h-BN/intercalated Pt/Rh(111) system designed as (EDe + annealing + SLDe) (green line), exhibits a single peak situated at 400 K, that is 100 K lower compared to the desorption temperature from the SLDe Pt supported on h-BN. This shift in the desorption temperature, clearly, indicates that the introduction of an intermediate Pt layer between the h-BN and the Rh(111) helps in reducing CO poisoning on subsequently soft landed Pt on h-BN. It seems that Pt intercalation below h-BN modifies the electronic states of the non intercalated Pt in such a way that causes a decrease in the CO adsorption energy. Generally speaking, the more Pt is positively charged, the weaker the CO bonding to the metal. Therefore, one can expect a charge donation from the non intercalated Pt to the substrate in the presence of an intermediate intercalated Pt layer which weakens CO adsorption.

In the absence of theoretical calculations of CO adsorption on Pt supported by h-BN/Rh(111), one can suggest an interpretation of CO poisoning reduction in the presence of an intercalated Pt layer as follows. It is known that adjusting the charge state of the catalyst affects its adsorption behavior with reactants. On Pt(111), h-BN is weakly bonded to the substrate because of the weak Pt d,s–h-BN π orbital mixing, while on Rh(111) the bonding is significantly stronger as a consequence of better orbital overlap.[139] So it can be stated that, in the case of Pt/h-BN/Rh(111) only, the strong h-BN-Rh(111) interaction may cause the electronic clouds of the h-BN defects to polarize much more downward toward the substrate (Fig. 7.4). Thus, the Pt clusters on top will remain in more reduced state which strengthens the overlapping with CO π orbital resulting in a strong adsorption state. However when a Pt interlayer is inserted between h-BN and Rh(111), the weak interaction between h-BN and Pt will decouple the h-BN and pushes the defect electronic clouds upward maximizing their interaction with the adsorbed Pt clusters which results in a charge donation from the catalyst to the substrate. Consequently, it can be said that the resulting weakening of CO-Pt bonding may be caused by a reduction in CO π population. Figure 7.4 gives a simplified schematic overview of this mechanism. Also, the enhancement of the non intercalated Pt interaction with the underlaying h-BN may well explain the observed increase in the clusters stability. A perspective DFT calculation would be helpful to confirm these experimental results.

7.3 Conclusion

Pt/h-BN/intercalated Pt/Rh(111) configuration was accomplished by cluster implantation in consecutive cycles of irradiation and annealing to 800 K. Soft landed Pt on top of h-BN/Rh(111) is found to settle inside the h-BN depressions while energetic Pt clusters intercalate and settle below the h-BN wires. Annealing of the intercalated Pt to 800 K, leads to its expanding in a layered form under the h-BN. Combination of soft landed, energetic deposition of Pt and annealing forms a multilayer system made of the Pt/h-BN/intercalated Pt/Rh(111) system. Using TDS, we found that soft landed Pt/h-BN/Rh(111) configuration exhibits high CO desorption temperature (or CO poisoning) while the Pt/h-BN/intercalated Pt/Rh(111) configuration shows a lower desorption temperature. Hence, CO adsorption strength to Pt can be controlled using an appropriate support,*e.g.*, intercalated Pt layer between h-BN and Rh(111). Moreover, in this situation, it is found that the Pt clusters show remarkably high thermal stability up to 800 K.

8 Fe_3 on h-BN/Rh(111): Stability and ammonia synthesis

In this chapter, h-BN/Rh(111) supported Fe_3 system was prepared and used as a model catalyst for ammonia synthesis reaction. Iron is a well-known and efficient catalyst for dinitrogenase reduction. The small iron clusters show remarkably high activity for dinitrogen dissociation and ammonia synthesis at reduced temperature and under UHV conditions compared to conventional Fe single crystals. Iron clusters exhibit ripening according to the Ostwald mechanism up to 600 K and above this temperature, Fe partially intercalates between the h-BN monolayer and the Rh(111) substrate. This intercalation is found more pronounced after catalytic activity measurements,*i.e.*, under gas reaction exposure and temperature. At relatively low deposition temperatures (100 K), the STM topography of the Fe clusters shows the coexistence of 2 imaging states; a ring state structure around the h-BN depression and a dot like structure. The ring state structure is found thermally stable and disappears only upon annealing above room temperature. Using temperature programmed reduction (TPR) of dinitrogen and hydrogen, NH_3 production could be fully confirmed following the Haber-Bosch method. It was found that, in the presence of iron, the nitrogen gas reaction experiences an exchange with the nitrogen species forming the h-BN layer. In addition, two radicals NH and NH_2 together with desorbed atomic nitrogen were directly observed during the reaction, hence, they should be desorbed from the catalyst surface.

8.1 Introduction

Ammonia is one of the most intensively produced chemical by industry with a world annual production of around 235 million tons and a market of 100 billion dollar forecast in 2019.[234] Because of the vast use of nitrogenous fertilizers, ammonia is an important industrial chemical compound. Also, it has high potential as a source of hydrogen storage and supply.[235] Ammonia formation through dinitrogen (N_2) splitting and reduction with hydrogen (H) requires a high amount of energy and a complex chain of production. An effective ammonia conversion under ambient conditions is the ultimate goal. There has been few successful attempts along this way using molybdenum model complexes to mediate the stoichiometric conversion of N_2 to NH_3.[236–239] There are two standard routes to form ammonia; one is a biological process occurring under ambient conditions when nitrogen from air is fixed by bacteria found in the roots of some plants and then converted, using chemical energy, to ammonia by an enzyme called nitrogenase.[240,241] This enzyme is based on a Fe-Mo cofactor as the active center for ammonia synthesis. The iron-molybdenum active site of the enzyme nitrogenase has pushed efforts on exploring iron and molybdenum complexes as catalysts for N_2 reduction. However, it is now thought that iron is the only transition metal essential to all nitrogenases.[241,242] The second route, called the Haber-Bosch process and mediated by an iron-based catalyst[243] which catalyzes N_2 to ammonia under high temperatures and pressures, is an industrial method developed a century ago. Although the triple bound in N_2 is very strong making N_2 inert and hard to dissociate, iron is effective as a catalyst because it lowers the barrier for N_2 dissociation. It does this by breaking the triple N bond and forming Fe-N chemisorbed bonds. A non catalyzed reaction should proceed at 800 °C under 200 bars. Nevertheless, with the use of a catalyst in the Haber-Bosch process, the reaction can be conducted at typical temperatures as low as 500 °C. The role of the catalyst is to help N_2 dissociation, which is generally considered a rate-determining step, as well as reaction with hydrogen for the production of NH_3 which is a very stable nitrogen hydride.

Clusters have been shown to be good models for many catalytic reactions.[64] The use of nanocatalysts during ammonia synthesis could reduce energy consumption, while simultaneously improving the production efficiency. In a very recent study, model catalysts made of free iron-sulfur clusters are found to functionalize N_2 binding independently of the cluster size and charge.[244] Industrial nano-iron catalyst supported on oxide support has been produced allowing ammonia synthesis at reduced pressures and temperatures, so that about 50 % of energy could be saved against the present methods.[113] It was found that Ru-based model catalysts show superior performance over conventional iron-based catalysts.[245] However for cost and availability issues, Fe based catalyst is still the most used. Nevertheless, reducing the clusters size to what is called the non scalable regime makes them exposed to ripening and loss of the active sites by agglomeration. The catalytic activity is size dependent[7] and because of that, stability is an important parameter to be considered. Adding or removing an atom could considerably change the entire cluster properties. On the other hand, when particles get smaller, their interaction with the support could considerably affect their intrinsic activity and selectivity, so a better choice of support is crucial. For example, ammonia synthesized over Ru supported on $12CaO_7Al_2O_3$ provides a new and highly efficient way for N_2 bond dissociation[246] via strong electron donation from the support. Even so, it has been reported that suitable support materials for promoted ammonia synthesis should have a non reactive surface such as boron nitride or magnesium oxide.[247–249]

This part of the work reports on ammonia synthesis over Fe_3 clusters supported on h-BN/Rh(111) as a model catalyst. STM was used to study the cluster thermal stability before and after the reaction. TPR (Temperature Programed Reaction) was then used to elucidate dinitrogen dissociation and NH_x product formation as a function of temperature.

8.2 Results and discussion

8.2.1 Fe_3 stability

The stability and catalytic activity of Fe_3 clusters supported on h-BN/Rh(111) has not been studied yet. The first part of this study focuses on the cluster thermal stability before investigating the catalytic activity in ammonia synthesis. We start with an initial cluster coverage of 1.4 x 10^{-3} cluster per Rh atom (20 % with respect to the number of moiré supercell). Figure 8.1 shows STM images (taken at 80 K) of the iron clusters deposited at 100 K then annealed at various temperatures up to 800 K. These small clusters are found very prone to ripening and intercalation at high temperature. In the case of as deposited iron at 100 K, the STM topography was dominated by particles showing a circular structure which forms a ring around the h-BN depressions (donut-like) in conjunction with few clusters in the form of spherical protrusions (dots-like). The observed objects constitute a bistable adsorption complex mediated by tip-cluster interaction[120] that we will discuss in detail later. At room temperature, Figure 8.1b displays the coexistence of the two imaging states but most of the clusters regain their spherical form, which means that the temperature suppresses the previous observed effect. This is clearly confirmed from Figure 8.1c-d, where the annealing temperature is higher and where all the clusters are spherical in form and are found at the edge side of the h-BN depressions (such as in the Pt_7/h-BN/Rh(111)). Intercalation under the h-BN was observed in the case when iron clusters were annealed at 700 K or more. In this case, the structures appearing with low contrast in the STM image are Fe sandwiched between the h-BN and the Rh(111) and showing an apparent height of 3.3 Å. Those looking brighter are Fe_x still remaining above the h-BN surface and showing an apparent height of 5 Å. Further annealing at 800 K, leads to more pronounced Fe intercalation and agglomeration.

The cluster apparent height histograms shown in Figure 8.3 measures, at 100 K, two distinct heights. The first peak at 2 Å corresponds to the height of the circular shaped clusters and the second at 3 Å to the spherical shaped ones that matches roughly the height of a monoatomic iron sphere. It can be noticed, from STM topography, the presence of clusters with different sizes which refers to a ripening process during annealing. The corresponding histograms indicate an Ostwald ripening in which the clusters increase in height but the coverage remains almost constant up to 600 K. One has to note, that the difference in the apparent height of Fe (3.3 Å) and Pt (2.2 Å) intercalated species under h-BN is 0.7 Å higher in the case of Fe. This is simply due to the fact that h-BN on Pt adsorbs flat, whereas h-BN supported on iron exhibits a corrugation of 0.7 Å in height and about 2.4 nm periodicity as shown in Figure. 8.2 which explains the difference in the apparent height between the intercalated Fe and Pt. A recent study found that h-BN adsorbed on the Fe(110) surface revealed the presence of two primary domains with a specific 1D moiré pattern (or nanowaves).[16] The period of this 1D structure is about 2.6 nm, and the corrugation amplitude is nearly 0.8 Å, very close to our measured values.

The bistable configuration mentioned above can be considered as two distinct states of the

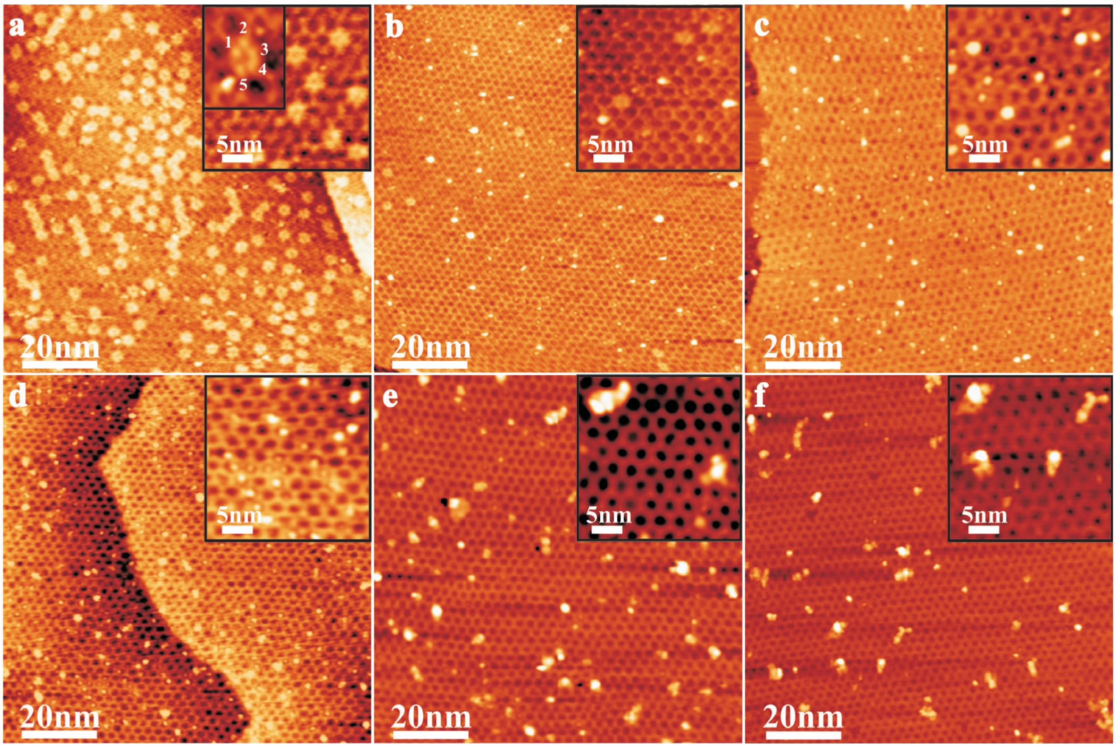

Figure 8.1 – Overview STM images of (a) soft landing of Fe_3 on h-BN/Rh(111) at 1.2 eV per atom and 100 K. (b-f) STM images of Fe_3 annealed at 300, 500, 600, 700 and 800 K, respectively. The insets are magnified regions of the respective surface.

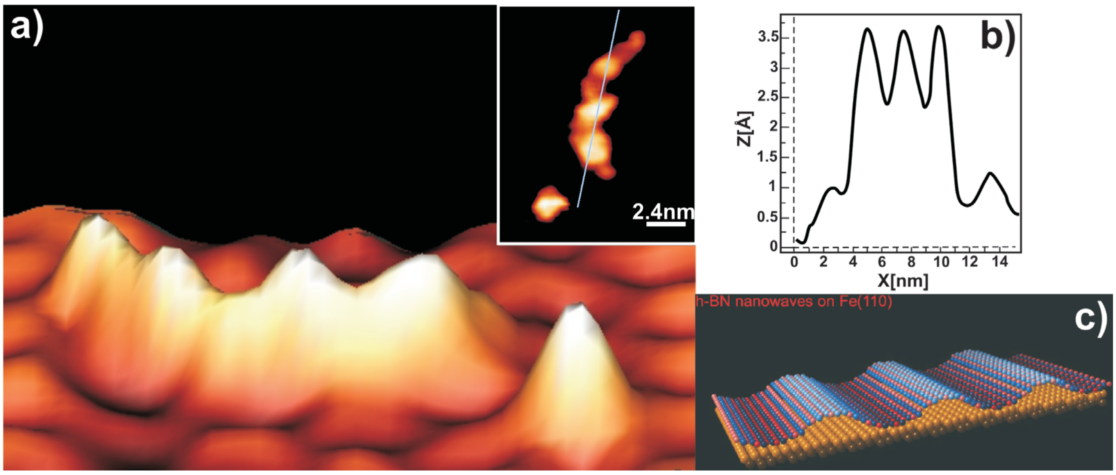

Figure 8.2 – h-BN corrugation on intercalated Fe. a) 3D STM image showing h-BN on Fe as nanowaves. b) height profile showing the corrugation amplitude and periodicity taken from the line profile traced as shown in the inset of (a). (c) schematic model of the h-BN corrugation on Fe(110), adapted from Ref. [16]

same cluster resulting from h-BN-Rh(111) weakening in the presence of Fe clusters. Precedently, Xe adsorption on h-BN/Rh(111) reveals a similar ring state feature consisting in 12 Xe atoms in the studied temperature range between 5 and 85 K. [32,250] Prior to the present study, F. Natterer and al. observed such a behavior, between 10 and 35 K, in the case of Mn, Fe and Co adatoms adsorbed at 10 K on h-BN/Rh(111). [120] They showed a switching between the dot and the ring state by applying a positive voltage pulse on top of the structure where the ring state is attributed to a single transition metal (TM) adatom only. Combining the two observations (TM adatoms and Xe clusters) the most relevant interpretation to our case, as reported by Natterer, would emphasizes the fact that interaction of the tip and the sample locally deformed and detached the h-BN layer, weakened by the TM adsorption, from the substrate which leads to the intriguing STM appearance while the adatom itself, for unknown reasons, is hidden within the ring state .

Since we know the cluster density which is extrapolated from the cluster ion current and deposition time, we can conclude that each observed bistable (a ring or a dot protrusion) structure, in Figure 8.1a, envelopes an Fe_3 cluster. Evidently, the reported ring state is not only restricted to Fe adatoms but to Fe clusters (at least containing 3 atoms) as well. The majority part of the ring protrusions donate five small protrusions surrounding h-BN depressions with an apparent height of 2 Å with respect to the depression (as shown in the inset of Fig. 8.1a). Natterer et al. observed similar feature in which one ring protrusion gives several small protrusions with an apparent height of 2 Å as well. However, the cluster based ring state exhibits a high temperature stability as it persists even at 300 K before completely switching to the dot state at 500 K. At the limit of our investigation, the stability of the ring state and its disappearance under thermal effect remains unexplained. Nonetheless, one could suppose that the disappearance of the ring state is related to a cluster size effect. As the temperature increases, small clusters grow to larger ones. Consequently, large clusters should have a tendency to promote metal-metal over metal-substrate interaction. Therefore, the substrate is less perturbed (or weakened) by Fe clusters which leads to the suppression of the related effect.

8.2.2 Ammonia synthesis

The iron clusters are used as model catalysts for ammonia synthesis. In contrast to dinitrogenase enzymes in which hydrogen fixation and reduction is the limiting step, N_2 dissociation on iron based catalysts, under high vacuum, is the rate limiting one. This is one reason why, in nature, N_2 bond can be functionalized already at mild conditions while the Haber-Bosch method applies high temperature and pressure to dissociate N_2 in the presence of iron based catalysts. In this part, TPR was used to elucidate the N_2 adsorption, dissociation and reduction to ammonia in the presence of H_2 and isotopic $^{30}N_2$ gases. During annealing, the crystal was continuously exposed to a static pressure of H_2 due to the presence of background H_2 in the gas line and in the ultrahigh vacuum (UHV) chamber (about 15 % of the dosed $^{30}N_2$). Figure 8.5a represents TPR for masses ^{14}N, ^{15}N, $^{29}N_2$, and $^{30}N_2$ after the surface was saturated with $^{30}N_2$ isotopic gas at 150 K and heated at 2K/s until the desorption ceased. Studies about the chemical nature of adsorbed nitrogen species are still under debates. It is believed that adsorbed molecular species dominate at low temperature while above room temperature tightly bound atomic species overcome.[251] Using CO adsorbed on iron precovered with nitrogen, Takezawa and Emmett[252] found that, from 400 and 600 K, a considerable portion of the chemisorbed nitrogen is held as nitrogen molecules whereas at temperatures of about 700 K it is primarily in the atomic form. It should be noted that, the release of neutral nitrogen atoms is unlikely and even surprising because it is energetically unfavorable. In fact, to our knowledge, direct observation of atomic nitrogen desorption from iron has never been reported. Only nitrogen molecular recombinative desorption was monitored using conventional methods such as TDS or TPR.

As shown in Figure 8.5a, chemisorbed ^{15}N desorbs with 2 peaks for which the desorption maximum occurs at about 620 and 710 K. This is 150 K lower than N_2 molecular recombinative desorption from Fe(111) or Fe(110) crystal.[253] The peak at 620 K could be attributed to C_7 sites (Fe atoms with the seven nearest neighbors). One can expect that agglomerated Fe_3 clusters could produce large clusters with highly coordinated C_7 sites. Describing the clusters by the hard sphere model (see chapter 5), their size N can be estimated from the STM apparent height. The corresponding cluster size are shown in Figure 8.3 in red. At 620 K, the average cluster size is N = 6 but we also identify clusters with a size N = 10,15, 25 and 33 as well. It is known that Fe(111) and Fe(211) exhibit the peak related to C_7 sites, contrary to Fe(100) or Fe(110) where these sites are spare.[254] This is due to the open structure of the Fe(111) that has both C_4 (four-fold coordinated atoms) and C_7 atoms exposed to the surface. The low index of Fe(111) and Fe(100) plane as well as the C_7 and C_4 surface atoms on body-centered cubic structures are sketched in Figure 8.4. The 620 K peak could, also, be attributed to a

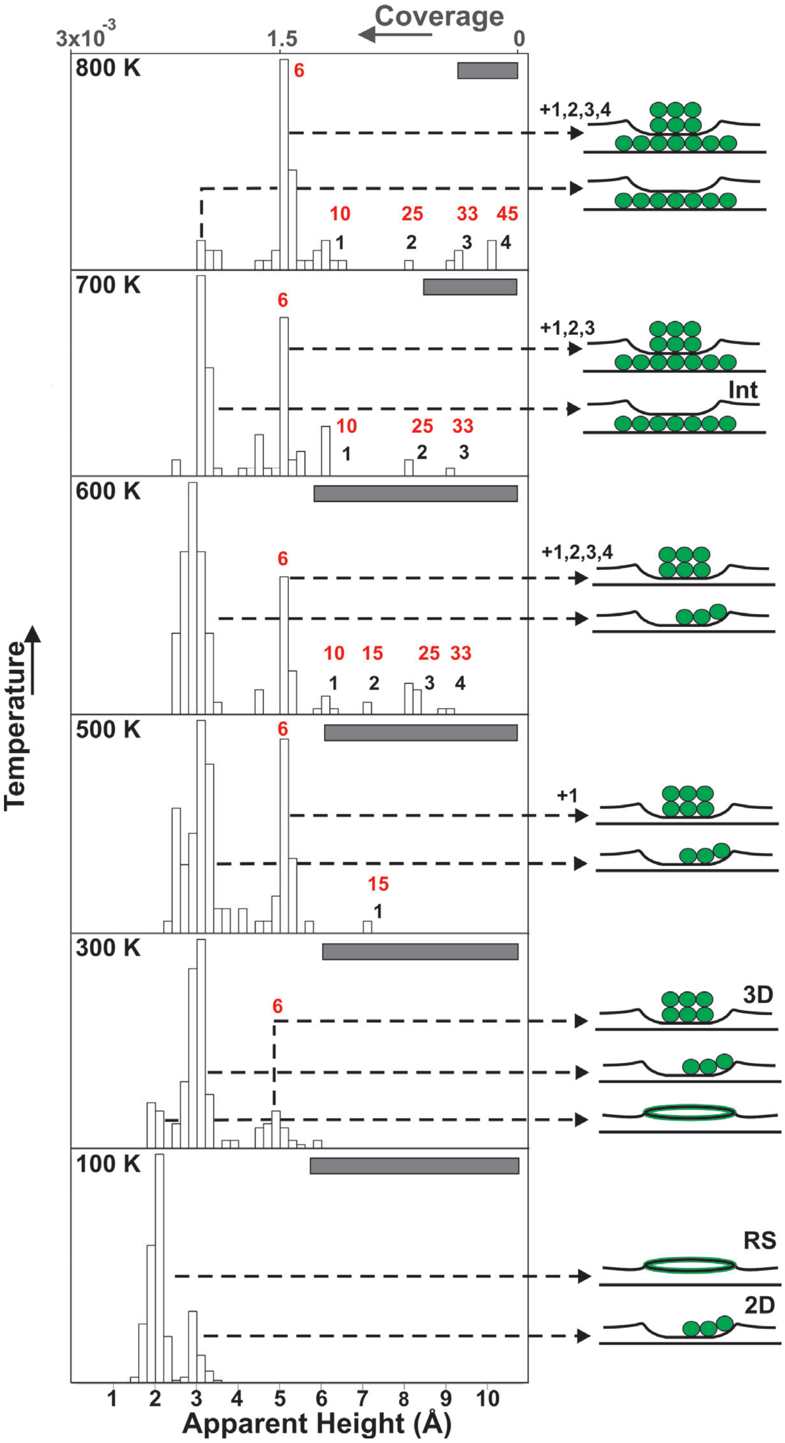

Figure 8.3 – Apparent height distributions of as deposited and post annealed Fe_3 in UHV. The initial coverage (in grey) was 1.4×10^{-3} clusters per Rh atom. RS: ring state, 2D: 2 dimensional structure, 3D: 3 dimensional structure, Int: Intercalated. The red colored values indicate the cluster size N deduced from the hard sphere model.

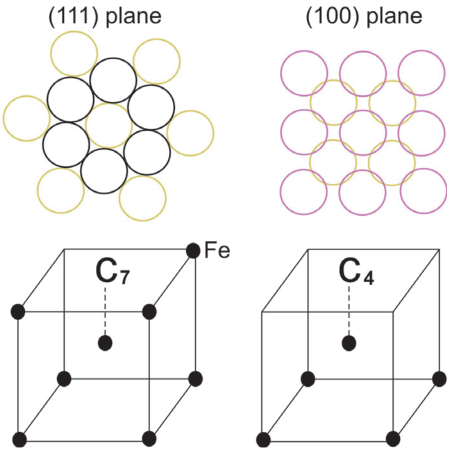

Figure 8.4 – Fe(111) and Fe(100) low index planes and iron body-centered cubic lattice showing the C_7 and C_4 surface atoms.

face specific adsorption. In fact, different crystallographic planes give different desorption temperatures. However, it is not straightforward to deduce the orientation plan of the iron clusters from STM images.

Molecular recombination desorption of $^{30}N_2$ and $^{29}N_2$ was, also, observed at a temperature slightly smaller (T_{max} = 670 K) compared to atomic ^{15}N and ^{14}N desorption (T_{max} = 710 K). The total amount of molecular desorbed N_2 is distinctively smaller. The simultaneous observation of ^{14}N and $^{29}N_2$ can only be ascribed to isotopic exchange with the ^{14}N constituent forming the h-BN layer. The ratio of ^{15}N to ^{14}N impurities present in the N_2 gas supply used in this experiment was found to be 250, while the amount of desorbing ^{15}N is by 2 fold greater than ^{14}N, which means that the majority of desorbing ^{14}N comes from the reaction itself. Hunter et al.[255] observed an isotopic exchange of ^{15}N with ^{14}N in cobalt molybdenum nitride lattice. This exchange becomes only active at temperature of 700 K and above. Adsorbed iron clusters on h-BN defects such as B vacancies would bind tightly to the dangling ^{14}N bonds of h-BN. Once the two species (atomic ^{15}N on iron surface and the ^{14}N of the support) encounter, nitrogen recombinative molecular desorption should be released ($^{29}N_2$). This would emphasize the possible occurrence of the Mars-van Krevelen mechanism (see chapter 1) in the ammonia synthesis reaction over the h-BN supported catalysts. Performing the same experiment on a clean h-BN/Rh(111) did not show any of ^{14}N desorption which means that iron clusters are the ones responsible for such desorption. The occurence of the TPR peaks and the existence of isotopic mixing of ^{14}N and ^{15}N show clearly that nitrogen at, 700 K, is adsorbed atomically on the iron clusters. Equation 8.1 shows the different possible combinations and sequences of nitrogen interaction with iron supported on h-BN/Rh(111). The "g" and "ad" refer to gaseous and adsorbed nitrogen species, respectively, and "sub" to nitrogen of the h-BN substrate.

$$^{30}N_{2,g} + * \rightarrow 2^{15}N_{ad} \;\Rightarrow\; ^{15}N_{ad} + ^{14}N_{sub} \rightarrow ^{29}N_{2,ad} \;\Rightarrow\; ^{15}N_{ad} + ^{15}N_{ad} \rightarrow ^{30}N_{2,ad} \quad (8.1)$$

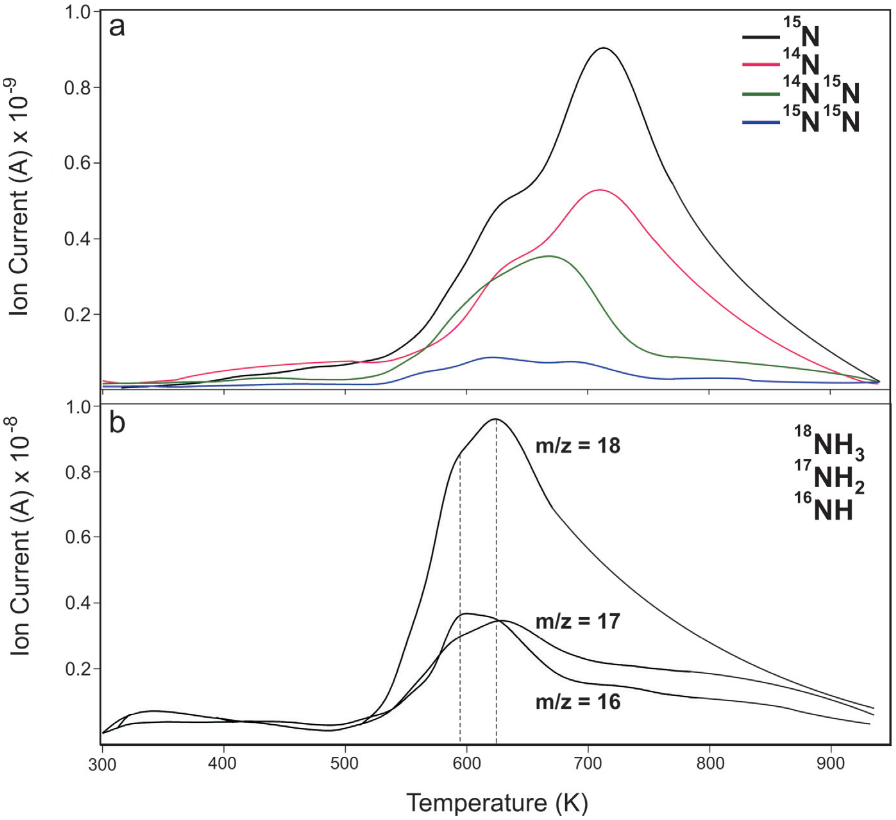

Figure 8.5 – N_2 TPR performed on Fe_3/h-BN/Rh(111). (a) nitrogen desorption. (b) NH_x formation.

The π orbitals of N were assumed to interact with the empty Fe orbitals, thus leading to weakening of the N-N bond which should be favorable for hydrogenation,[8] while the H_2 pressure in the gas supply, should be sufficient for some ammonia formation to be accomplished. Ammonia synthesis proceeds through reduction of either molecular or atomic nitrogen species :

$^{15}N_{ad} + 3H_{ad} \rightarrow {}^{18}NH_3$ (atomic species)
$^{30}N_{2,ad} + 6H_{ad} \rightarrow 2\,{}^{18}NH_3$ (molecular species)

Figure 8.5b shows dinitrogen reduction with hydrogen during the N_2 desorption. The occurrence of the peaks in the spectra where m/z = 16-17 and m/z = 18 further confirms the generation of NH_x species. The NH_x radicals are important in nitrogen-containing systems. It is used to reduce NO_x in the exhaust gases[256] and also is an important constituent in the fabrication of semiconducting materials.[257] Reaction intermediates during ammonia synthesis are usually identified through indirect method of identification based on theoretical calculations or using some detection techniques such as pulsed-laser stimulated field desorption.[258,259] Nevertheless some experimental studies, directly, observed NH and NH_2 radicals during ammonia decomposition on iron using different analysis techniques such as SIMS (Secondary Ion Mass Spectroscopy)[260] or mass spectrometer.[261] To our knowledge, this is the first observation of NH and NH_2 radicals occurring during NH_3 formation on a catalyst surface, using desorption spectroscopy technique. The possibility that the m/z = 16,17 and 18 peaks could originate from water desorbing from iron can be excluded since water desorption from a clean Fe(100) occurs, only, at low temperature (300 K).[262]

It is known that NH_3 which gives rise to the dominant peak in the TPR, proceeds by adding H to the intermediate radicals as indicated by the equations 8.2.

$$^{15}N_{ad} + H_{ad} \rightarrow ^{16}NH_{ad} \;\Rightarrow\; ^{16}NH_{ad} + H_{ad} \rightarrow ^{17}NH_{2,ad} \;\Rightarrow\; ^{17}NH_{2ad} + H_{ad} \rightarrow ^{18}NH_3 \tag{8.2}$$

The formation of NH and NH_2 intermediates confirms that the NH_3 formation involves the stepwise hydrogenation of atomic nitrogen. Also, it could be very likely that ^{14}N reacts with hydrogen forming ammonia ($^{17}NH_3$). An interesting alternatives to the above reactions are

$$^{14}N_{ad} + 2H_{ad} \rightarrow ^{16}NH_{2,ad} \qquad \Rightarrow \qquad ^{14}N_{ad} + 3H_{ad} \rightarrow ^{17}NH_3 \tag{8.3}$$

The identity corresponding to m/z = 17 is not clear, although only two possibilities can exist as given in equations 8.2 and 8.3.

Based on the results of Fe stability discussed above, it becomes worthy to shed light on the catalyst state after the reaction. Figure 8.6a,b show two STM images of the catalyst before (Fig. 8.6a) and after the reaction (Fig. 8.6b). The as deposited Fe_3 clusters are shown as white protrusions located on the h-BN depressions. The surface images are shown in a reverse topography in order to get a better imaging stability by reducing cluster drift. This topography is obtained when h-BN is tunneled with high voltage, in which the regions representing the wires are imaged as depressions and the regions showing depressions are imaged as hills.[263] At the end of the reaction, the Fe particles are found to undergo massive intercalation. It is well known that NH_3 formation is an exothermic process. The reaction energy excess is transferred to the catalyst promoting diffusion and intercalation. Therefore, three situations could face us; firstly, Fe is completely under h-BN. This is monitored as a low contrast flake-like structures. Secondly, the Fe clusters are in a non intercalated position and show as white protrusions on top of the h-BN and finally a dual combination between intercalated and non intercalated Fe. This latter situation, which is the majority configuration, shows Fe protrusions on top of the intercalated regions. At this level of study, it is unclear whether the Fe on top of the h-BN/intercalated Fe/Rh(111) exhibits the same chemical behavior as Fe on top of h-BN/Rh(111) or not. Figure 8.6c, represents a schematic illustration of the Fe intercalation during NH_3 formation. The catalyzing Fe_x ($6 < x < 45$) particles, are driven through the wires underneath h-BN where

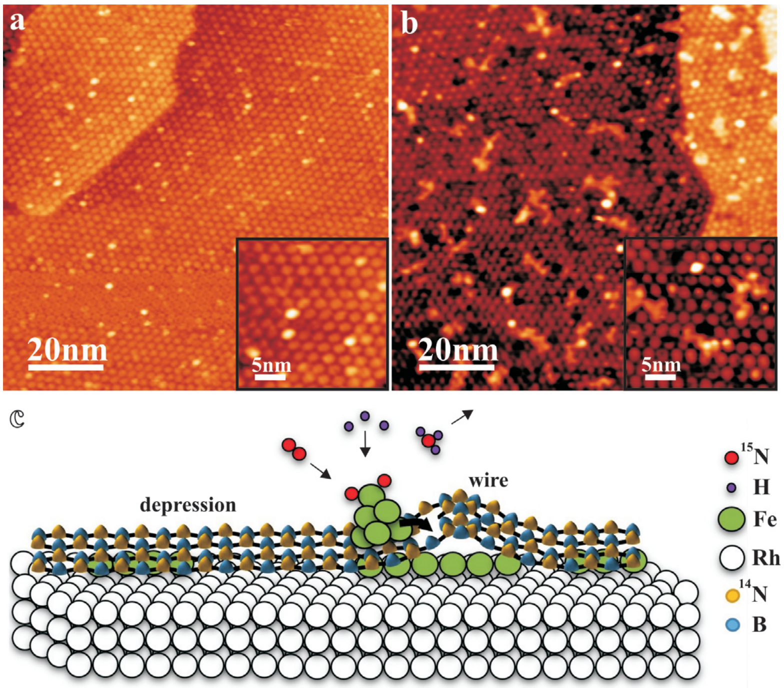

Figure 8.6 – Fe_3/h-BN/Rh(111) stability. (a) as deposited (b) after reaction (c) schematic view of Fe intercalation during the reaction. Tunneling conditions : I_t = 200 mA, V_t = 4 V.

they form an intermediate layer. Because of the relative high ammonia synthesis temperature, iron intercalation must be taken into account. A charge transfer between the support, in the presence of intercalated Fe_x, and the catalyst or vice versa is conceivable which then would have an effect on the catalytic behavior of the Fe clusters. This, however, needs future studies.

8.3 Conclusion

In summary, Fe clusters supported onto hexagonal boron nitride monolayer on Rh(111) are found to be an excellent catalyst for dinitrogen dissociation and ammonia synthesis under UHV. TPR confirmed that nitrogen adsorbs molecularly and atomically over the iron clusters following the Haber-Bosch method. The chemisorbed nitrogen was found to desorb from the catalyst with a peak whose maximum occurs at about 710 K. In addition, we have monitored the presence of a shoulder in the NH_3 peak that can be attributed to C_7 phase of the Fe_x clusters ($6 < x < 33$). The STM imaging of the sample after reaction shows that the clusters undergo a massive ripening and intercalation giving rise to their coarsening. It was found that, in the presence of iron, the isotopic nitrogen gas experiences an exchange with the nitrogen species forming the h-BN layer. The detection of the reaction intermediates NH and NH_2 during ammonia synthesis confirms that NH_3 formation involves the stepwise hydrogenation of atomic nitrogen. The cluster stability investigation, as a function of temperature, shows that the clusters grow by Ostwald ripening and undergo intercalation at higher temperature (T

= 700 K). Because of the relative high temperature of ammonia synthesis, iron intercalation must be taken into account during reaction. At lower temperature (T = 100 K) we featured the presence of a bistable configuration representing a ring state that is attributed to h-BN weakening in the presence of Fe clusters. In STM, the bistable appear either as a ring around h-BN depression or a conventional cluster imaged as a dot or sphere. This dual state remains even at room temperature and disappears only at 500 K.

9 General conclusion

The catalytic aspects and the surface interaction of very small Pt and Fe clusters supported on h-BN/Rh(111) were investigated. The clusters stability on h-BN/Rh(111) as a function of temperature and gas exposure was analyzed. This was achieved using state of the art STM, TDS and TPR techniques combined in an UHV experimental setup. In chapter 5, we investigated the stability and the catalytic activity of Pt_7 clusters for CO oxidation. It was found that soft landed Pt clusters are stable at room temperature as they settle at the h-BN side edge depressions with no sign of ripening. The Pt_7 was found to adapt a flat structure on the surface at room temperature and upon annealing it grow by Smoluchowski ripening establishing a 3D structure. Starting at 900 K, partial intercalation between the h-BN and the Rh(111) is observed. This is the first observation of Pt intercalation similar to several transition metal clusters such as Au or Co supported on h-BN. Upon annealing under gas reaction, Pt clusters undergo a massive intercalation and ripening even at lower temperatures. This is attributed to the skyhook effect for which the gas molecules that bind to Pt lift up the cluster providing easy access to ripening and intercalation. Temperature programmed desorption of CO reveals that h-BN terraces could not adsorb CO gas at a temperature as low as 150 K. Only a single desorption peak is found to occur at 250 K reminiscent to desorption from intrinsic h-BN defects. CO TDS was performed on P_7/h-BN/Rh(111) which give rise to a richly structured desorption around 500 K. In the case where partial Pt intercalation exist, weak desorption occurs but only at 400 K,$i.e.$, shifted by about 100 K compared to the non-intercalated system. Besides, we showed that the clean h-BN/Rh(111) surface is inert towards CO oxidation where no CO_2 production was monitored. For Pt_7 supported on h-BN/Rh(111), a high catalytic activity towards CO oxidation is found. The reaction starts at 480 K and reaches its maximum at 500 K before decreasing again, following the Langmuir Hinshelwood mechanism. For the Pt clusters that are adsorbed on the h-BN just above the intercalated Pt, the onset reaction temperature is shifted by 100 K towards lower temperatures. This reduction is caused by the Pt intercalated species that modify the intrinsic influence of the h-BN/Rh(111) support on the non intercalated Pt clusters as a result of substrate effect and charge redistribution.

In chapter 6, Pt_7 interaction with h-BN/Rh(111) was studied by means of energetic clusters in the energy range $416 > E_k > 30$ eV/atom. The clusters show a markably different behavior compared to soft landed ones. At room temperature, the energetic clusters are found to shelter under the h-BN wires, more precisely at the wire crossing, which is the largest available free volume for the particles. The sheltered species are made of Pt and h-BN defects created during impact since they were found to multiply with increasing energy as a consequence of Pt fragmentation and h-BN defect creation. At relatively high energy ($E_k \geq 314$ eV/atom), the under-depression sites begin to populate with intercalated species. For $E_k > 100$ eV/atom, cavity-type defects start to appear on the h-BN and become more abundant as the energy increases. Annealing was found to cure h-BN defects and restore a surface free from visual induced defects. Moreover, annealing at 600 K under gas reaction, is found to displace the intercalated Pt from the underwire sites to the under depression sites. These latter sites are considered non favorable for adsorption because of the strong interaction between h-BN and Rh(111) at that locations. The presence of intercalated species, after annealing, under the depression sites was interpreted by stabilization through agglomerated induced h-BN defects at the h-BN rims. Further annealing at 800 K leads to enhanced intercalation under h-BN resulting in a large intercalation areas. At 950 K the intercalated species diffuse and attach to the Rh(111) steps.

In chapter 7, we combined the two regimes in which Pt is on top (soft landed) and under the h-BN monolayer (energetic deposition), using successive energetic and soft deposition that were followed by annealing at 800 K. The energetic deposition intercalates Pt while annealing allows it to expand and produces large intercalated areas. The soft deposition lands the clusters above the h-BN depressions. Combining the steps produces a situation in which a Pt/h-BN/intercalated Pt/Rh(111) configuration can be obtained. We demonstrated that this configuration reduced CO poisoning by 100 K compared to the case where Pt is only soft landed on h-BN/Rh(111). This shift in the desorption temperature, clearly, indicates that the introduction of an intermediate Pt layer between h-BN and Rh(111) helps in reducing CO poisoning on subsequently soft landed Pt on h-BN/Rh(111). Furthermore, in this situation, it is found that the Pt clusters show remarkably high thermal stability up to 800 K compared to soft landed Pt on h-BN/Rh(111) that were deposited at room temperature and annealed at the same temperature. This configuration would be a strong prototype cluster catalyst system.

In chapter 8, the stability and ammonia synthesis of Fe_3 clusters supported on h-BN/Rh(111) were investigated. These small clusters are found very prone to ripening and intercalation at high temperature. The clusters deposited at 100 K are found to grow via Ostwald ripening at 600 K. From 700 K and more, Fe intercalation under h-BN is always observed. The h-BN regions situated above the intercalated Fe, reveals the presence of a 1D structure corrugation (or what is called nanowave) of about 2.4 nm period with an amplitude of nearly 0.7 Å. In the case of as deposited iron at 100 K, the STM topography is dominated by particles showing circular structure which forms a ring around the h-BN depressions. The ring state is found to exhibit high temperature stability as it persists even at 300 K. Chemisorbed ^{15}N and ^{14}N are found to desorb, each with 2 peaks, at about 620 and 710 K. The peak at 620 K could be attributed to C_7 sites (Fe atoms with the seven nearest neighbors) of agglomerated Fe_3 clusters. Molecular recombination desorption of $^{30}N_2$ and $^{29}N_2$ is, also, observed with a temperature slightly smaller (T_{max} = 670 K). The simultaneous observation of ^{14}N and $^{29}N_2$ is ascribed to an exchange with the ^{14}N constituent forming the h-BN layer emphasizing the possible occurrence of the Mars-van Krevelen mechanism in the ammonia synthesis reaction over h-BN supported Fe catalyst. Finally, dinitrogen reduction with hydrogen is observed at 620 K with the generation of NH_x (x = 1-3) species using temperature programmed reduction (TPR) following the Haber-Bosch method.

A Supporting information for chapter 6

The Apparent height histograms of energetic Pt_7 were measured by analyzing STM images. The results of the statistical analysis based on several images are shown in Figure A.1. The histograms are arranged vertically as a function of deposition energy for as deposited, after annealing at 600 K under gas reaction and after annealing at 800 K. The as deposited sample exhibits an apparent height peak at 3.2 Å in the case of soft landing deposition (1.2 eV/atom). In the case of energetic deposition at 30 eV/atom, the peak is shifted down to 2.2 Å. This can be assigned to the non thermal intercalation of Pt under h-BN. As the energy increases, the corresponding apparent height for different energies (60, 100, 170 ,314 and 416 eV/atom) was found unchanged with respect to each other. In the case of soft landed (1.2 eV/atom) Pt_7 annealed under gas reaction, the height distribution showed a mix of a 2.2, 3.2 and 5.2 Å peaks. Some clusters have undergo partial intercalation (2.2 Å), configuration reconstruction (5.2 Å) and some of them remain as deposited (3.2 Å). In the high energy regime (≥ 30 eV/atom), the apparent height was found to be 3.2 Å. As discussed in chapter 6, Pt leaves the under wire sites (with an apparent height of 2.2 Å) to move under the h-BN depressions and remains underneath. Finally, annealing of the sample on which the Pt_7 was soft landed (at 1.2 eV/atom) at 800 K leads to an intense apparent height peak at 2.2 Å reminiscent to Pt intercalation. Some clusters in this sample remained on the top of h-BN and are well visible with small peaks distributed at 8.3 and 12 Å. For energetic deposition (≥ 30 eV/atom), the apparent height, after annealing to 800 K, shifts back again to 2.2 Å as a consequence of intercalated species diffusion under the h-BN moiré.

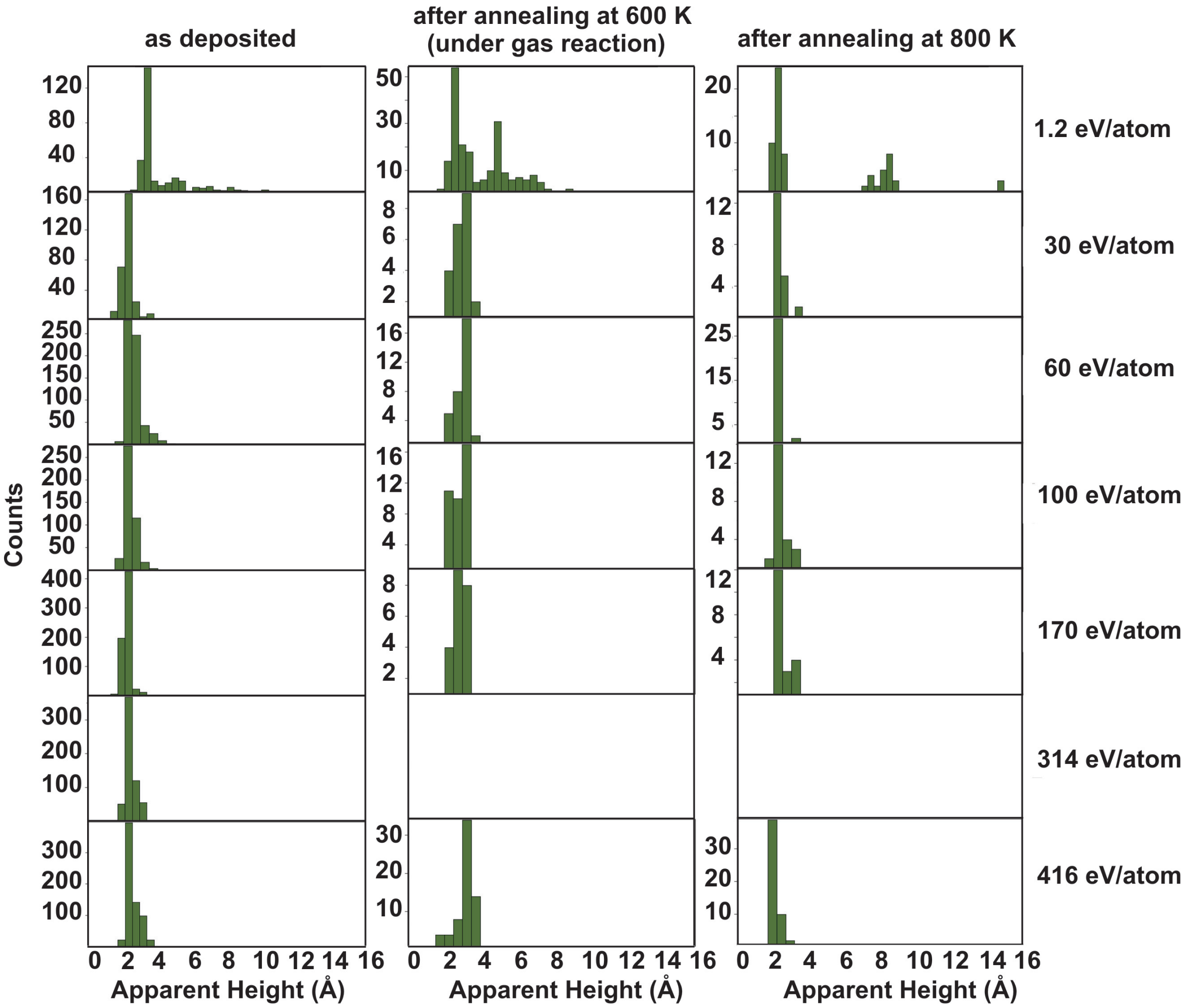

Figure A.1 – Histograms of apparent height showing the height distribution of the Pt_7 on h-BN/Rh(111) for as deposited, after annealing at 600 K under gas reaction and after annealing at 800 K vs the deposition kinetic energy.

Bibliography

[1] Flom, S. EDMST Carnegie Mellon University. 2003; http://environ.andrew.cmu.edu/.

[2] Heiz, U.; Landman, U. *Nanocatalysis. Nanoscience and Technology*; Springer, 2007.

[3] Mahata, A.; Rawat, K. S.; Choudhuri, I.; Pathak, B. *Scientific reports* **2016**, *6*.

[4] Hugentobler, M. Ph.D. thesis, EPFL, 2010.

[5] Longwitz, R. G. Study of gas ionization in a glow discharge and development of a micro gas ionizer for gas detection and analysis. Ph.D. thesis, Citeseer, 2004.

[6] Brune, H.; Bales, G. S.; Jacobsen, J.; Boragno, C.; Kern, K. *Physical Review B* **1999**, *60*, 5991.

[7] Bonanni, S.; Ait-Mansour, K.; Harbich, W.; Brune, H. *Journal of the American Chemical Society* **2014**, *136*, 8702–8707.

[8] Sljivancanin, Z.; Brune, H.; Pasquarello, A. *Physical Review B* **2009**, *80*, 075407.

[9] Brihuega, I.; Michaelis, C. H.; Zhang, J.; Bose, S.; Sessi, V.; Honolka, J.; Schneider, M. A.; Enders, A.; Kern, K. *Surface Science* **2008**, *602*, L95–L99.

[10] Berner, S.; Corso, M.; Widmer, R.; Groening, O.; Laskowski, R.; Blaha, P.; Schwarz, K.; Goriachko, A.; Over, H.; Gsell, S. *Angewandte Chemie international edition* **2007**, *46*, 5115–5119.

[11] Cun, H.; Iannuzzi, M.; Hemmi, A.; Osterwalder, J.; Greber, T. *ACS nano* **2013**, *8*, 1014–1021.

[12] De Lima, L.; Cun, H.; Hemmi, A.; Kalin, T.; Greber, T. *Review of Scientific Instruments* **2013**, *84*, 126104.

[13] Woodruff, D. P.; Delchar, T. A. *Modern techniques of surface science*; Cambridge university press, 1994.

[14] Vallotton, R. Ph.D. thesis, EPFL, 2009.

[15] Bliem, R.; van der Hoeven, J. E.; Hulva, J.; Pavelec, J.; Gamba, O.; de Jongh, P. E.; Schmid, M.; Blaha, P.; Diebold, U.; Parkinson, G. S. *Proceedings of the National Academy of Sciences* **2016**, *113*, 8921–8926.

[16] Vinogradov, N. A.; Zakharov, A.; Ng, M. L.; Mikkelsen, A.; Lundgren, E.; Mårtensson, N.; Preobrajenski, A. *Langmuir* **2012**, *28*, 1775–1781.

[17] Binnig, G.; Rohrer, H.; Gerber, C.; Weibel, E. *Physical review letters* **1982**, *49*, 57.

[18] Heiz, U.; Sanchez, A.; Abbet, S.; Schneider, W.-D. *Journal of the American Chemical Society* **1999**, *121*, 3214–3217.

[19] Sanchez, A.; Abbet, S.; Heiz, U.; Schneider, W.-D.; Hakkinen, H.; Barnett, R.; Landman, U. *The Journal of Physical Chemistry A* **1999**, *103*, 9573–9578.

[20] Schnabel, P.; Weil, K. G.; Irion, M. P. *Angewandte Chemie International Edition in English* **1992**, *31*, 636–638.

[21] Blagojevic, V.; Jarvis, M. J.; Flaim, E.; Koyanagi, G. K.; Lavrov, V. V.; Bohme, D. K. *Angewandte Chemie International Edition* **2003**, *42*, 4923–4927.

[22] Yoon, B.; Hakkinen, H.; Landman, U.; Worz, A. S.; Antonietti, J.-M.; Abbet, S.; Judai, K.; Heiz, U. *Science* **2005**, *307*, 403–407.

[23] Bonanni, S.; Ait-Mansour, K.; Harbich, W.; Brune, H. *Journal of the American Chemical Society* **2012**, *134*, 3445–3450.

[24] Bonanni, S.; Ait-Mansour, K.; Brune, H.; Harbich, W. *Acs Catalysis* **2011**, *1*, 385–389.

[25] Sun, W.; Meng, Y.; Fu, Q.; Wang, F.; Wang, G.; Gao, W.; Huang, X.; Lu, F. *ACS applied materials & interfaces* **2016**, *8*, 9881–9888.

[26] Zhang, Y.; Weng, X.; Li, H.; Li, H.; Wei, M.; Xiao, J.; Liu, Z.; Chen, M.; Fu, Q.; Bao, X. *Nano letters* **2015**, *15*, 3616–3623.

[27] Lin, C.-A.; Wu, J. C.; Pan, J.-W.; Yeh, C.-T. *Journal of Catalysis* **2002**, *210*, 39–45.

[28] Lu, Z.; Lv, P.; Xue, J.; Wang, H.; Wang, Y.; Huang, Y.; He, C.; Ma, D.; Yang, Z. *RSC Advances* **2015**, *5*, 84381–84388.

[29] Xu, D.; Liu, Y.-j.; Zhao, J.-x.; Cai, Q.-h.; Wang, X.-z. *The Journal of Physical Chemistry C* **2014**, *118*, 8868–8876.

[30] Koch, H. P.; Laskowski, R.; Blaha, P.; Schwarz, K. *Physical Review B* **2011**, *84*, 245410.

[31] Abbet, S.; Riedo, E.; Brune, H.; Heiz, U.; Ferrari, A. M.; Giordano, L.; Pacchioni, G. *Journal of the American Chemical Society* **2001**, *123*, 6172–6178.

[32] Dil, H.; Lobo-Checa, J.; Laskowski, R.; Blaha, P.; Berner, S.; Osterwalder, J.; Greber, T. *Science* **2008**, *319*, 1824–1826.

[33] Fukamori, Y.; Konig, M.; Yoon, B.; Wang, B.; Esch, F.; Heiz, U.; Landman, U. *ChemCatChem* **2013**, *5*, 3330–3341.

[34] Akizuki, M.; Matsuo, J.; Yamada, I.; Harada, M.; Ogasawara, S.; Doi, A. *Nuclear Instruments and Methods in Physics Research Section B: Beam Interactions with Materials and Atoms* **1996**, *112*, 83–85.

[35] Klopcic, S. A.; Jarrold, M. F. *Journal of Chemical Physics* **1997**, *106*, 8855–8861.

[36] Yoshida, A.; Deguchi, M.; Kitabatake, M.; Hirao, T.; Matsuo, J.; Toyoda, N.; Yamada, I. *Nuclear Instruments and Methods in Physics Research Section B: Beam Interactions with Materials and Atoms* **1996**, *112*, 248–251.

[37] Borland, J.; Hautala, J.; Gwinn, M.; Tetreault, T.; Skinner, W. *Solid State Technology* **2004**, *47*, 53–57.

[38] Seki, T.; Murase, T.; Matsuo, J. *Nuclear Instruments and Methods in Physics Research Section B: Beam Interactions with Materials and Atoms* **2006**, *242*, 179–181.

[39] Kunimatsu, K.; Sato, T.; Uchida, H.; Watanabe, M. *Langmuir* **2008**, *24*, 3590–3601.

[40] Somorjai, G. A.; Li, Y. *Introduction to surface chemistry and catalysis*; John Wiley & Sons, 2010.

[41] Somorjai, G.; Rioux, R. *Catalysis Today* **2005**, *100*, 201–215.

[42] Wu, X.; Deng, Z.; Yan, J.; Zhang, F.; Zhang, Z. *Industrial & Engineering Chemistry Research* **2014**, *53*, 14601–14606.

[43] Jennings, J. R. *Catalytic ammonia synthesis: fundamentals and practice*; Springer Science & Business Media, 2013.

[44] Campbell, C.; Ertl, G.; Kuipers, H.; Segner, J. *The Journal of Chemical Physics* **1980**, *73*, 5862–5873.

[45] Socaciu, L. D.; Hagen, J.; Bernhardt, T. M.; Woste, L.; Heiz, U.; Hakkinen, H.; Landman, U. *Journal of the American Chemical Society* **2003**, *125*, 10437–10445.

[46] Mars, P.; Van Krevelen, D. W. *Chemical Engineering Science* **1954**, *3*, 41–59.

[47] Doornkamp, C.; Ponec, V. *Journal of Molecular Catalysis A: Chemical* **2000**, *162*, 19–32.

[48] Noyori, R. *Nature chemistry* **2009**, *1*, 5–6.

[49] Chen, G.; Xu, C.; Huang, X.; Ye, J.; Gu, L.; Li, G.; Tang, Z.; Wu, B.; Yang, H.; Zhao, Z. *Nature materials* **2016**,

[50] Njagi, E. C.; Chen, C.-H.; Genuino, H.; Galindo, H.; Huang, H.; Suib, S. L. *Applied Catalysis B: Environmental* **2010**, *99*, 103–110.

[51] Santra, A.; Goodman, D. *Electrochimica Acta* **2002**, *47*, 3595–3609.

[52] Tao, F.; Dag, S.; Wang, L.-W.; Liu, Z.; Butcher, D. R.; Bluhm, H.; Salmeron, M.; Somorjai, G. A. *Science* **2010**, *327*, 850–853.

[53] Zetterberg, J.; Blomberg, S.; Gustafson, J.; Evertsson, J.; Zhou, J.; Adams, E. C.; Carlsson, P.-A.; Aldén, M.; Lundgren, E. *Nature communications* **2015**, *6*.

[54] Kunz, S.; Schweinberger, F. F.; Habibpour, V.; Rottgen, M.; Harding, C.; Arenz, M.; Heiz, U. *The Journal of Physical Chemistry C* **2009**, *114*, 1651–1654.

[55] Craig, J. *Applied surface science* **1986**, *25*, 333–340.

[56] Argyle, M. D.; Bartholomew, C. H. *Catalysts* **2015**, *5*, 145–269.

[57] Modak, J. M. *Resonance* **2002**, *7*, 69–77.

[58] Stoltze, P.; Nørskov, J. *Journal of Catalysis* **1988**, *110*, 1–10.

[59] Ferguson, M. J. *Lawrence Berkeley National Laboratory* **2005**,

[60] Ertl, G.; Lee, S.; Weiss, M. *Surface Science* **1982**, *114*, 527–545.

[61] Spencer, M. *Catalysis letters* **1992**, *13*, 45–53.

[62] Dellwig, T.; Hartmann, J.; Libuda, J.; Meusel, I.; Rupprechter, G.; Unterhalt, H.; Freund, H.-J. *Journal of Molecular Catalysis A: Chemical* **2000**, *162*, 51–66.

[63] Heiz, U.; Sanchez, A.; Abbet, S.; Schneider, W.-D. *The European Physical Journal D-Atomic, Molecular, Optical and Plasma Physics* **1999**, *9*, 35–39.

[64] Tyo, E. C.; Vajda, S. *Nature nanotechnology* **2015**, *10*, 577–588.

[65] Gates, B. *Chemical reviews* **1995**, *95*, 511–522.

[66] Kaden, W. E.; Kunkel, W. A.; Kane, M. D.; Roberts, F. S.; Anderson, S. L. *Journal of the American Chemical Society* **2010**, *132*, 13097–13099.

[67] Mostafa, S.; Behafarid, F.; Croy, J. R.; Ono, L. K.; Li, L.; Yang, J. C.; Frenkel, A. I.; Cuenya, B. R. *Journal of the American Chemical Society* **2010**, *132*, 15714–15719.

[68] Cuenya, B. R.; Ortigoza, M. A.; Ono, L.; Behafarid, F.; Mostafa, S.; Croy, J.; Paredis, K.; Shafai, G.; Rahman, T.; Li, *Physical Review B* **2011**, *84*, 245438.

[69] Mott, D.; Luo, J.; Njoki, P. N.; Lin, Y.; Wang, L.; Zhong, C.-J. *Catalysis Today* **2007**, *122*, 378–385.

[70] Libuda, J.; Freund, H.-J. *Surface Science Reports* **2005**, *57*, 157–298.

[71] Bruix, A.; Rodriguez, J. A.; Ramirez, P. J.; Senanayake, S. D.; Evans, J.; Park, J. B.; Stacchiola, D.; Liu, P.; Hrbek, J.; Illas, F. *Journal of the American Chemical Society* **2012**, *134*, 8968–8974.

[72] Campbell, C. T. *Nature chemistry* **2012**, *4*, 597–598.

[73] Yan, Z.; Chinta, S.; Mohamed, A. A.; Fackler, J. P.; Goodman, D. W. *Journal of the American Chemical Society* **2005**, *127*, 1604–1605.

[74] Chrétien, S.; Metiu, H. *The Journal of chemical physics* **2007**, *126*, 104701.

[75] Hutchings, G. J.; Hall, M. S.; Carley, A. F.; Landon, P.; Solsona, B. E.; Kiely, C. J.; Herzing, A.; Makkee, M.; Moulijn, J. A.; Overweg, A. *Journal of Catalysis* **2006**, *242*, 71–81.

[76] Jiang, Z.; Xie, J.; Jiang, D.; Wei, X.; Chen, M. *CrystEngComm* **2013**, *15*, 560–569.

[77] Geng, J.; Jefferson, D. A.; Johnson, B. F. *Chemical Communications* **2007**, 969–971.

[78] Haruta, M. *The chemical record* **2003**, *3*, 75–87.

[79] Lang, S. M.; Bernhardt, T. M. *Physical Chemistry Chemical Physics* **2012**, *14*, 9255–9269.

[80] Haruta, M.; Kobayashi, T.; Sano, H.; Yamada, N. *Chemistry Letters* **1987**, 405–408.

[81] Koch, H. P.; Laskowski, R.; Blaha, P.; Schwarz, K. *Physical Review B* **2012**, *86*, 155404.

[82] Henry, C. R. *Surface Science Reports* **1998**, *31*, 231–325.

[83] Hakkinen, H.; Abbet, S.; Sanchez, A.; Heiz, U.; Landman, U. *Angewandte Chemie International Edition* **2003**, *42*, 1297–1300.

[84] Pinna, F. *Catalysis Today* **1998**, *41*, 129–137.

[85] Jacobs, P.; Ribeiro, F.; Somorjai, G.; Wind, S. *Catalysis letters* **1996**, *37*, 131–136.

[86] Hamm, G.; Becker, C.; Henry, C. *Nanotechnology* **2006**, *17*, 1943.

[87] Buck, U.; Meyer, H. *Surface Science* **1985**, *156*, 275–281.

[88] Keller, R.; Nohmayer, F.; Spadtke, P.; Schonenberg, M. *Vacuum* **1984**, *34*, 31–35.

[89] Schaffner, M.-H.; Jeanneret, J.-F.; Patthey, F.; Schneider, W.-D. *Journal of Physics D: Applied Physics* **1998**, *31*, 3177.

[90] Harbich, W. Collision of clusters with surfaces: surface modification and scattering. 2000.

[91] Félix, C.; Vandoni, G.; Massobrio, C.; Monot, R.; Buttet, J.; Harbich, W. *Physical Review B* **1998**, *57*, 4048.

[92] Carroll, S.; Pratontep, S.; Streun, M.; Palmer, R.; Hobday, S.; Smith, R. *The Journal of Chemical Physics* **2000**, *113*, 7723–7727.

[93] Goldby, I. Ph.D. thesis, Cambridge, 1996.

[94] Ostawald, W. *Z. Phys. Chem.* **1900**, *34*, 495.

[95] Lifshitz, I.; Slyozov, V. *J. Phys. Chem. Solids* **1961**, *19*, 35.

[96] Wettergren, K.; Schweinberger, F. F.; Deiana, D.; Ridge, C. J.; Crampton, A. S.; Rotzer, M. D.; Hansen, T. W.; Zhdanov, V. P.; Heiz, U.; Langhammer, C. *Nano letters* **2014**, *14*, 5803–5809.

[97] Zhang, Y.; Zhang, Y.; Ma, D.; Ji, Q.; Fang, W.; Shi, J.; Gao, T.; Liu, M.; Gao, Y.; Chen, Y. *Nano Research* **2013**, *6*, 887–896.

[98] Nair, M. N. Functionalization of epitaxial graphene by metal intercalation and molecules. Ph.D. thesis, Université de Haute Alsace-Mulhouse, 2013.

[99] Alattas, M.; Schwingenschlogl, U. *Scientific reports* **2016**, *6*.

[100] Vu, A.-D.; Coraux, J.; Chen, G.; N'Diaye, A.; Schmid, A.; Rougemaille, N. *Scientific reports* **2016**, *6*.

[101] der Merwe, J. H. V. *Interface Sci.* **1993**, *1*, 77.

[102] Bauer, E.; Poppa, H. *Thin Solid Films* **1972**, *12*, 167.

[103] Zhang, S.; Chang, C.-R.; Huang, Z.-Q.; Li, J.; Wu, Z.; Ma, Y.; Zhang, Z.; Wang, Y.; Qu, Y. *Journal of the American Chemical Society* **2016**, *138*, 2629–2637.

[104] Kowalczyk, Z.; Sentek, J.; Jodzis, S.; Mizera, E.; Goralski, J.; Paryjczak, T.; Diduszko, R. *Catalysis Letters* **1997**, *45*, 65–72.

[105] Mazzieri, V. A.; Sad, M. R.; Vera, C. R.; Pieck, C. L.; Grau, R. *Quimica Nova* **2010**, *33*, 269–272.

[106] Vajda, S.; Pellin, M. J.; Greeley, J. P.; Marshall, C. L.; Curtiss, L. A.; Ballentine, G. A.; Elam, J. W.; Catillon-Mucherie, S.; Redfern, P. C.; Mehmood, F. *Nature materials* **2009**, *8*, 213–216.

[107] Harding, D. J.; Kerpal, C.; Rayner, D. M.; Fielicke, A. *The Journal of chemical physics* **2012**, *136*, 211103.

[108] Sebetci, A.; Guvenc, Z. B. *Surface science* **2003**, *525*, 66–84.

[109] Huda, M.; Niranjan, M. K.; Sahu, B.; Kleinman, L. *Physical Review A* **2006**, *73*, 053201.

[110] Shi, Y.; Ervin, K. M. *Journal of Chemical Physics* **1998**, *108*, 1757–1760.

[111] Isomura, N.; Wu, X.; Watanabe, Y. *The Journal of chemical physics* **2009**, *131*, 164707–164707.

[112] Lauher, J. W. *Journal of the American Chemical Society* **1978**, *100*, 5305–5315.

[113] Notestein, J. M.; Prieto-Centurion, D.; Fanson, P. T.; Roberts, C. A. Ceria-supported metal catalysts for the selective reduction of NO_x. 2016; US Patent 9,283,548.

[114] Pakdel, A.; Bando, Y.; Golberg, D. *Chemical Society Reviews* **2014**, *43*, 934–959.

[115] Liu, X.; Duan, T.; Meng, C.; Han, Y. *RSC Advances* **2015**, *5*, 10452–10459.

[116] Kim, K. K.; Hsu, A.; Jia, X.; Kim, S. M.; Shi, Y.; Dresselhaus, M.; Palacios, T.; Kong, J. *ACS nano* **2012**, *6*, 8583–8590.

[117] Corso, M.; Auwarter, W.; Muntwiler, M.; Tamai, A.; Greber, T.; Osterwalder, J. *Science* **2004**, *303*, 217–220.

[118] Kim, K. K.; Hsu, A.; Jia, X.; Kim, S. M.; Shi, Y.; Hofmann, M.; Nezich, D.; Rodriguez-Nieva, J. F.; Dresselhaus, M.; Palacios, T. *Nano letters* **2011**, *12*, 161–166.

[119] Goriachko, A.; He, Y.; Over, H. *The Journal of Physical Chemistry C* **2008**, *112*, 8147–8152.

[120] Natterer, F. D.; Patthey, F.; Brune, H. *Physical review letters* **2012**, *109*, 066101.

[121] Lin, Y.; Connell, J. W. *Nanoscale* **2012**, *4*, 6908–6939.

[122] Bacle, P.; Seitsonen, A. P.; Iannuzzi, M.; Hutter, J. *CHIMIA International Journal for Chemistry* **2014**, *68*, 596–601.

[123] Nagashima, A.; Tejima, N.; Gamou, Y.; Kawai, T.; Oshima, C. *Physical review letters* **1995**, *75*, 3918.

[124] Corso, M.; Auwarter, W.; Muntwiler, M.; Tamai, A.; Greber, T.; Osterwalder, J. *Science* **2004**, *303*, 217–220.

[125] Goriachko, A.; He, Y.; Knapp, M.; Over, H.; Corso, M.; Brugger, T.; Berner, S.; Osterwalder, J.; Greber, T. *Langmuir* **2007**, *23*, 2928–2931.

[126] Cicoira, F.; Rosei, F. *Surface science* **2006**, *600*, 1–5.

[127] Gao, M.; Lyalin, A.; Taketsugu, T. *The Journal of chemical physics* **2013**, *138*, 034701.

[128] Orellana, W.; Chacham, H. *Physical Review B* **2001**, *63*, 125205.

[129] Natterer, F.; Patthey, F.; Brune, H. *Surface Science* **2013**, *615*, 80–87.

[130] Auwärter, W.; Muntwiler, M.; Osterwalder, J.; Greber, T. *Surface science* **2003**, *545*, L735–L740.

[131] Wang, H.; Yuan, H.; Hong, S. S.; Li, Y.; Cui, Y. *Chemical Society Reviews* **2015**, *44*, 2664–2680.

[132] Zeng, H.; Zhi, C.; Zhang, Z.; Wei, X.; Wang, X.; Guo, W.; Bando, Y.; Golberg, D. *Nano letters* **2010**, *10*, 5049–5055.

[133] Zhou, J.; Wang, Q.; Sun, Q.; Jena, P. *Physical Review B* **2010**, *81*, 085442.

[134] Rokuta, E.; Hasegawa, Y.; Suzuki, K.; Gamou, Y.; Oshima, C.; Nagashima, A. *Physical review letters* **1997**, *79*, 4609.

[135] Preobrajenski, A.; Vinogradov, A.; Martensson, N. *Surface science* **2005**, *582*, 21–30.

[136] Lyalin, A.; Nakayama, A.; Uosaki, K.; Taketsugu, T. *The Journal of Physical Chemistry C* **2013**, *117*, 21359–21370.

[137] Dong, G. *Formation of graphene and hexagonal boron nitride on Rh(111) studied by in-situ scanning tunneling microscopy*; Kamerlingh Onnes Laboratory, Leiden Institute of Physics, Faculty of Science, Leiden University, 2012.

[138] Brugger, T.; Ma, H.; Iannuzzi, M.; Berner, S.; Winkler, A.; Hutter, J.; Osterwalder, J.; Greber, T. *Angewandte Chemie International Edition* **2010**, *49*, 6120–6124.

[139] Preobrajenski, A.; Vinogradov, A.; Ng, M. L.; Cavar, E.; Westerstrom, R.; Mikkelsen, A.; Lundgren, E.; Martensson, N. *Physical Review B* **2007**, *75*, 245412.

[140] Loh, G.; Nigam, S.; Mallick, G.; Pandey, R. *The Journal of Physical Chemistry C* **2014**, *118*, 23888–23896.

[141] Cun, H.; Iannuzzi, M.; Hemmi, A.; Roth, S.; Osterwalder, J.; Greber, T. *Nano letters* **2013**, *13*, 2098–2103.

[142] Iannuzzi, M. *The Journal of Physical Chemistry C* **2015**, *119*, 22198–22207.

[143] Ng, M. L. Characterization and Functionalization of 2D Overlayers Adsorbed on Transition Metals. Ph.D. thesis, Uppsala, 2010.

[144] Rut'kov, E.; Tontegode, A. Y.; Usufov, M. *Technical Physics* **1999**, *44*, 1066–1068.

[145] Turner, M.; Golovko, V. B.; Vaughan, O. P.; Abdulkin, P.; Berenguer-Murcia, A.; Tikhov, M. S.; Johnson, B. F.; Lambert, R. M. *Nature* **2008**, *454*, 981–983.

[146] Yang, Y.; Fu, Q.; Wei, M.; Bluhm, H.; Bao, X. *Nano Research* **2015**, *8*, 227–237.

[147] Ng, M. L.; Shavorskiy, A.; Rameshan, C.; Mikkelsen, A.; Lundgren, E.; Preobrajenski, A.; Bluhm, H. *ChemPhysChem* **2015**, *16*, 923–927.

[148] Bonanni, S.; Ait-Mansour, K.; Hugentobler, M.; Brune, H.; Harbich, W. *The European Physical Journal D* **2011**, *63*, 241–249.

[149] King, D. A. *Surface Science* **1975**, *47*, 384–402.

[150] De Jong, A.; Niemantsverdriet, J. *Surface Science* **1990**, *233*, 355–365.

[151] Redhead, P. *Vacuum* **1962**, *12*, 203–211.

[152] Bauer, E.; Bonczek, F.; Poppa, H.; Todd, G. *Surface Science* **1975**, *53*, 87–109.

[153] Bardeen, J. *Physical Review Letters* **1961**, *6*, 57.

[154] Tersoff, J.; Hamann, D. *Scanning Tunneling Microscopy*; Springer, 1985; pp 59–67.

[155] Convers, P. Ph.D. thesis, EPFL, 2005.

[156] Dong, G.; Fourré, E. B.; Tabak, F. C.; Frenken, J. W. *Physical review letters* **2010**, *104*, 096102.

[157] Tyo, E. C.; Vajda, S. *Nature nanotechnology* **2015**, *10*, 577–588.

[158] Watanabe, Y. *Science and Technology of Advanced Materials* **2016**,

[159] Remediakis, I. N.; Lopez, N.; Norskov, J. K. *Angewandte Chemie* **2005**, *117*, 1858–1860.

[160] Qiao, B.; Wang, A.; Yang, X.; Allard, L. F.; Jiang, Z.; Cui, Y.; Liu, J.; Li, J.; Zhang, T. *Nature chemistry* **2011**, *3*, 634–641.

[161] Lei, Y.; Mehmood, F.; Lee, S.; Greeley, J.; Lee, B.; Seifert, S.; Winans, R. E.; Elam, J. W.; Meyer, R. J.; Redfern, P. C. *Science* **2010**, *328*, 224–228.

[162] Vajda, S.; Pellin, M. J.; Greeley, J. P.; Marshall, C. L.; Curtiss, L. A.; Ballentine, G. A.; Elam, J. W.; Catillon-Mucherie, S.; Redfern, P. C.; Mehmood, F. *Nature materials* **2009**, *8*, 213–216.

[163] Herzing, A. A.; Kiely, C. J.; Carley, A. F.; Landon, P.; Hutchings, G. J. *Science* **2008**, *321*, 1331–1335.

[164] Sun, S.; Zhang, G.; Gauquelin, N.; Chen, N.; Zhou, J.; Yang, S.; Chen, W.; Meng, X.; Geng, D.; Banis, M. N. *Scientific reports* **2013**, *3*.

[165] Wettergren, K.; Schweinberger, F. F.; Deiana, D.; Ridge, C. J.; Crampton, A. S.; Rotzer, M. D.; Hansen, T. W.; Zhdanov, V. P.; Heiz, U.; Langhammer, C. *Nano letters* **2014**, *14*, 5803–5809.

[166] Fukui, N.; Yasumatsu, H. *The European Physical Journal D* **2013**, *67*, 1–4.

[167] Bartholomew, C. H. *Applied Catalysis A: General* **2001**, *212*, 17–60.

[168] Wynblatt, P.; Gjostein, N. *Progress in solid state chemistry* **1975**, *9*, 21–58.

[169] Charreteur, F.; Jaouen, F.; Ruggeri, S.; Dodelet, J.-P. *Electrochimica acta* **2008**, *53*, 2925–2938.

[170] Campbell, C. T. *Nature chemistry* **2012**, *4*, 597–598.

[171] OConnor, A. M.; Meunier, F. C.; Ross, J. R. *Studies in surface science and catalysis* **1998**, *119*, 819–824.

[172] Bonanni, S.; Ait-Mansour, K.; Brune, H.; Harbich, W. *Acs Catalysis* **2011**, *1*, 385–389.

[173] Xu, D.; Liu, Y.-j.; Zhao, J.-x.; Cai, Q.-h.; Wang, X.-z. *The Journal of Physical Chemistry C* **2014**, *118*, 8868–8876.

[174] Liu, X.; Duan, T.; Meng, C.; Han, Y. *RSC Advances* **2015**, *5*, 10452–10459.

[175] Gao, M.; Lyalin, A.; Taketsugu, T. *The Journal of chemical physics* **2013**, *138*, 034701.

[176] Mao, K.; Li, L.; Zhang, W.; Pei, Y.; Zeng, X. C.; Wu, X.; Yang, J. *Scientific reports* **2014**, *4*.

[177] Lin, S.; Ye, X.; Johnson, R. S.; Guo, H. *The Journal of Physical Chemistry C* **2013**, *117*, 17319–17326.

[178] Isomura, N.; Wu, X.; Watanabe, Y. *The Journal of chemical physics* **2009**, *131*, 164707–164707.

[179] Wang, S.; Zhang, Y.; Abidi, N.; Cabrales, L. *Langmuir* **2009**, *25*, 11078–11081.

[180] Mezey, L.; Giber, J. *Japanese Journal of Applied Physics* **1982**, *21*, 1569.

[181] Bennett, R.; Tarr, D.; Mulheran, P. *Journal of Physics: Condensed Matter* **2003**, *15*, S3139.

[182] Goriachko, A.; He, Y.; Over, H. *The Journal of Physical Chemistry C* **2008**, *112*, 8147–8152.

[183] Auwarter, W.; Muntwiler, M.; Greber, T.; Osterwalder, j. v. n. p. y. p., Jurg

[184] Gerber, T.; Knudsen, J.; Feibelman, P. J.; Granas, E.; Stratmann, P.; Schulte, K.; Andersen, J. N.; Michely, T. *ACS nano* **2013**, *7*, 2020–2031.

[185] Collings, M.; Dever, J.; Fraser, H.; McCoustra, M.; Williams, D. *The Astrophysical Journal* **2003**, *583*, 1058.

[186] McKee, W. C.; Patterson, M. C.; Huang, D.; Frick, J. R.; Kurtz, R. L.; Sprunger, P.; Liu, L.; Xu, Y. *The Journal of Physical Chemistry C* **2016**,

[187] Lyalin, A.; Nakayama, A.; Uosaki, K.; Taketsugu, T. *Topics in catalysis* **2014**, *57*, 1032–1041.

[188] Chen, M.; Cai, Y.; Yan, Z.; Gath, K.; Axnanda, S.; Goodman, D. W. *Surface Science* **2007**, *601*, 5326–5331.

[189] Bonanni, S.; Ait-Mansour, K.; Brune, H.; Harbich, W. *Acs Catalysis* **2011**, *1*, 385–389.

[190] Zhang, Y.; Weng, X.; Li, H.; Li, H.; Wei, M.; Xiao, J.; Liu, Z.; Chen, M.; Fu, Q.; Bao, X. *Nano letters* **2015**, *15*, 3616–3623.

[191] Yamada, I.; Matsuo, J.; Toyoda, N.; Aoki, T.; Seki, T. *Current Opinion in Solid State and Materials Science* **2015**, *19*, 12–18.

[192] Suda, T.; Toyoda, N.; Hara, K.-i.; Yamada, I. *Japanese Journal of Applied Physics* **2012**, *51*, 08HA02.

[193] Makarov, G. N. *Physics-Uspekhi* **2006**, *49*, 117–166.

[194] Yamada, I.; Nagai, I.; Horie, M.; Takagi, T. *Journal of Applied Physics* **1983**, *54*, 1583–1587.

[195] Yamada, I. New horizons in material processing with ICB. Proceedings of 14th Symposium on Ion Sources Ion-Assisted Technology, Tokyo, Japan. 1991; pp 227–235.

[196] Yamada, I.; Matsuo, J.; Insepov, Z.; Takeuchi, D.; Akizuki, M.; Toyoda, N. *Journal of Vacuum Science* & *Technology A* **1996**, *14*, 781–785.

[197] Haberland, H.; Insepov, Z.; Moseler, M. *Physical Review B* **1995**, *51*, 11061.

[198] Yamada, I.; Matsuo, J.; Jones, E.; Takeuchi, D.; Aoki, T.; Goto, K.; Sugii, T. Range and damage distribution in cluster ion implantation. MRS Proceedings. 1996; p 363.

[199] Takeuchi, D.; Shimada, N.; Matsuo, J.; Yamada, I. Shallow junction formation by polyatomic cluster ion implantation. Ion Implantation Technology. Proceedings of the 11th International Conference on. 1996; pp 772–775.

[200] Popok, V.; Campbell, E. E. *Rev. Adv. Mater. Sci* **2006**, *11*, 19–45.

[201] Auwarter, W.; Muntwiler, M.; Greber, T.; Osterwalder, J. *Surface science* **2002**, *511*, 379–386.

[202] Preobrajenski, A.; Ng, M. L.; Vinogradov, N.; Vinogradov, A.; Lundgren, E.; Mikkelsen, A.; Mårtensson, N. *Nano letters* **2009**, *9*, 2780–2787.

[203] Ding, Y.; Iannuzzi, M.; Hutter, J. *Chimia* **2010**, *65*, 256–259.

[204] Duong, D. L.; Han, G. H.; Lee, S. M.; Gunes, F.; Kim, E. S.; Kim, S. T.; Kim, H.; Ta, Q. H.; So, K. P.; Yoon, S. J. *Nature* **2012**, *490*, 235–239.

[205] Feng, X.; Maier, S.; Salmeron, M. *Journal of the American Chemical Society* **2012**, *134*, 5662–5668.

[206] Verbitskiy, N.; Fedorov, A.; Profeta, G.; Stroppa, A.; Petaccia, L.; Senkovskiy, B.; Nefedov, A.; Woll, C.; Usachov, D. Y.; Vyalikh, D. *Scientific reports* **2015**, *5*.

[207] Jiménez, I.; Jankowski, A.; Terminello, L. J.; Carlisle, J. A.; Sutherland, D.; Doll, G.; Mantese, J.; Tong, W. M.; Shuh, D. K.; Himpsel, F. J. *Applied physics letters* **1996**, *68*, 2816–2818.

[208] Ahlgren, E.; Hamalainen, S.; Lehtinen, O.; Liljeroth, P.; Kotakoski, J. *Physical Review B* **2013**, *88*, 155419.

[209] Standop, S.; Lehtinen, O.; Herbig, C.; Lewes-Malandrakis, G.; Craes, F.; Kotakoski, J.; Michely, T.; Krasheninnikov, A. V.; Busse, C. *Nano letters* **2013**, *13*, 1948–1955.

[210] Auwarter, W.; Suter, H. U.; Sachdev, H.; Greber, T. *Chemistry of materials* **2004**, *16*, 343–345.

[211] Herbig, C.; Ahlgren, E. H.; Jolie, W.; Busse, C.; Kotakoski, J.; Krasheninnikov, A. V.; Michely, T. *ACS nano* **2014**, *8*, 12208–12218.

[212] Gibb, A. L.; Alem, N.; Chen, J.-H.; Erickson, K. J.; Ciston, J.; Gautam, A.; Linck, M.; Zettl, A. *Journal of the American Chemical Society* **2013**, *135*, 6758–6761.

[213] Suenaga, K.; Kobayashi, H.; Koshino, M. *Physical review letters* **2012**, *108*, 075501.

[214] Jiménez, I.; Jankowski, A.; Terminello, L.; Sutherland, D.; Carlisle, J.; Doll, G.; Tong, W.; Shuh, D.; Himpsel, F. *Physical Review B* **1997**, *55*, 12025.

[215] Williams, F. L.; Nelson, G. *Applications of Surface Science* **1979**, *3*, 409–415.

[216] Sano, N.; Sakurai, T. *Le Journal de Physique Colloques* **1989**, *50*, C8–321.

[217] Cun, H.; Iannuzzi, M.; Hemmi, A.; Osterwalder, J.; Greber, T. *ACS nano* **2014**, *8*, 7423–7431.

[218] Cun, H.; Iannuzzi, M.; Hemmi, A.; Osterwalder, J.; Greber, T. *Surface Science* **2015**, *634*, 95–102.

[219] Butt, J. *Activation, deactivation, and poisoning of catalysts*; Elsevier, 2012.

[220] Melo, L.; Bott, T. R.; Bernardo, C. *Fouling science and technology*; Springer Science & Business Media, 2012; Vol. 145.

[221] Wanke, S. E.; Flynn, P. C. *Catalysis Reviews* **1975**, *12*, 93–135.

[222] Daggolu, P.; Joseph, A.; Kumar, D.; Cursetji, R. *Small Pt Cluster Size Diesel Oxidation Catalyst for Cold Start CO Oxidation*; 2015.

[223] Debe, M. K. *Nature* **2012**, *486*, 43–51.

[224] Blyholder, G. *The Journal of Physical Chemistry* **1964**, *68*, 2772–2777.

[225] Tang, Y.; Yang, Z.; Dai, X. *Journal of Nanoparticle Research* **2012**, *14*, 1–11.

[226] Dimakis, N.; Navarro, N. E.; Mion, T.; Smotkin, E. S. *The Journal of Physical Chemistry C* **2014**, *118*, 11711–11722.

[227] Yourdshahyan, Y.; Cooper, V. R.; Kolpak, A. M.; Rappe, A. M. Catalytic behavior at the nanoscale: CO adsorption on Al2O3-supported Pt clusters. Optical Science and Technology, SPIE's 48th Annual Meeting. 2003; pp 223–231.

[228] Liu, J.; Lucci, F. R.; Yang, M.; Lee, S.; Marcinkowski, M. D.; Therrien, A. J.; Williams, C. T.; Sykes, E. C. H.; Flytzani-Stephanopoulos, M. *Journal of the American Chemical Society* **2016**,

[229] Gasteiger, H. A.; Markovic, N.; Ross Jr, P. N.; Cairns, E. J. *The Journal of Physical Chemistry* **1993**, *97*, 12020–12029.

[230] Cui, G.; Shen, P. K.; Meng, H.; Zhao, J.; Wu, G. *Journal of Power Sources* **2011**, *196*, 6125–6130.

[231] Tang, Y.; Yang, Z.; Dai, X. *Physical Chemistry Chemical Physics* **2012**, *14*, 16566–16572.

[232] Stolbov, S.; Ortigoza, M. A.; Adzic, R.; Rahman, T. S. *The Journal of chemical physics* **2009**, *130*, 124714.

[233] Miura, H.; Gonzalez, R. D. *The Journal of Physical Chemistry* **1982**, *86*, 1577–1582.

[234] Ceresana, Market Study: Ammonia. 2012.

[235] Cheddie, D. *system* **2012**, *250*, 400.

[236] Schrock, R. R. *Accounts of chemical research* **2005**, *38*, 955–962.

[237] Arashiba, K.; Miyake, Y.; Nishibayashi, Y. *Nature chemistry* **2011**, *3*, 120–125.

[238] Yandulov, D. V.; Schrock, R. R. *Science* **2003**, *301*, 76–78.

[239] Lan, R.; Irvine, J. T.; Tao, S. *Scientific reports* **2013**, *3*.

[240] Rod, T. H.; Hammer, B.; Norskov, J. K. *Physical review letters* **1999**, *82*, 4054.

[241] Schimpl, J.; Petrilli, H. M.; Blochl, P. E. *Journal of the American Chemical Society* **2003**, *125*, 15772–15778.

[242] Anderson, J. S.; Rittle, J.; Peters, J. C. *Nature* **2013**, *501*, 84–87.

[243] Haber, F.; Weiss, J. **1934**, *147*, 332–351.

[244] Heim, H. C.; Bernhardt, T. M.; Lang, S. M.; Barnett, R. N.; Landman, U. *The Journal of Physical Chemistry C* **2016**,

[245] Saadatjou, N.; Jafari, A.; Sahebdelfar, S. *Chemical Engineering Communications* **2015**, *202*, 420–448.

[246] Kitano, M.; Kanbara, S.; Inoue, Y.; Kuganathan, N.; Sushko, P. V.; Yokoyama, T.; Hara, M.; Hosono, H. *Nature communications* **2015**, *6*.

[247] Bielawa, H.; Hinrichsen, O.; Birkner, A.; Muhler, M. *Angewandte Chemie International Edition* **2001**, *40*, 1061–1063.

[248] Jacobsen, C. J. *Journal of Catalysis* **2001**, *200*, 1–3.

[249] Hansen, T. W.; Hansen, P. L.; Dahl, S.; Jacobsen, C. J. *Catalysis letters* **2002**, *84*, 7–12.

[250] Widmer, R.; Passerone, D.; Mattle, T.; Sachdev, H.; Gröning, O. *Nanoscale* **2010**, *2*, 502–508.

[251] Ponec, V.; Knor, Z. *Journal of Catalysis* **1968**, *10*, 73–82.

[252] Takezawa, N.; Emmett, P. *Journal of Catalysis* **1968**, *11*, 131–134.

[253] Bozso, F.; Ertl, G.; Grunze, M.; Weiss, M. *Journal of Catalysis* **1977**, *49*, 18–41.

[254] Strongin, D.; Bare, S.; Somorjai, G. *Journal of Catalysis* **1987**, *103*, 289–301.

[255] Hunter, S. M.; Gregory, D. H.; Hargreaves, J. S.; Richard, M.; Duprez, D.; Bion, N. *ACS catalysis* **2013**, *3*, 1719–1725.

[256] Zhou, Q.; Yao, S.-C.; Russell, A.; Boyle, J. *Journal of the Air* & *Waste Management Association* **1992**, *42*, 1193–1197.

[257] Denbaars, S. *Proceedings of the IEEE* **1997**, *85*, 1740–1749.

[258] Liu, W.; Tsong, T. *Surface science* **1986**, *165*, L26–L30.

[259] Selwyn, G. S.; Fujimoto, G.; Lin, M. *The Journal of Physical Chemistry* **1982**, *86*, 760–765.

[260] Drechsler, M.; Hoinkes, H.; Kaarmann, H.; Wilsch, H.; Ertl, G.; Weiss, M. *Applications of Surface Science* **1979**, *3*, 217–228.

[261] Melton, C. E.; Emmett, P. H. *The Journal of Physical Chemistry* **1964**, *68*, 3318–3324.

[262] Hung, W.-H.; Schwartz, J.; Bernasek, S. *Surface science* **1993**, *294*, 21–32.

[263] Joshi, S.; Ecija, D.; Koitz, R.; Iannuzzi, M.; Seitsonen, A. P.; Hutter, J.; Sachdev, H.; Vijayaraghavan, S.; Bischoff, F.; Seufert, K. *Nano letters* **2012**, *12*, 5821–5828.

Acknowledgements

I am indebted to all those who have supported me over the last few years.

Foremost, I want to thank my thesis director Dr. Wolfgang Harbich, who I have my privileges to work under his supervision, knowledge and experience. His frequent patience with me is always appreciated. I could benefit from his constant presence and of his countless ideas to solve problems in the lab during all this time. The teaching duties under your supervision were very rewarding. I would also like to thank my thesis co-director Pof. Harald brune who gave me the opportunity to carry out this work in his group and who has always shown great interest in my work. Thank you for your advice and inspiration.

I would like to thank Dr. Friedrich Esch, Dr. Veronique Dupuis and Prof. Marco Grioni for accepting to be part of my thesis jury, and Prof. Vincenzo Savona for having presided it.

I would like to thank my first lab colleagues, Simon Bonnani and Kamel Ait-Mansouri, who taught me the secrets of the machine, and with whom I shared the first experiments in the lab.

As part of the institute, several other people have been fundamental for this work. Thanks to Gilles Grandjean and to all the workshop team and technicians, in particular, Claude Amendola. Thank you for your participation to solve small and major problems of every day.

A big thank to my colleagues, past and present, and friends at EPFL and Lausanne. Thanks for the friendly atmosphere and for the many activities we shared. A big thank also to my partner for sharing two years with me, I really enjoyed your presence.

A big thank to my family: my brother Amine, and my sisters Imene, Amina and Merieme for supporting me. A special thank goes to my father for his unfailing support throughout my life in general. He taught me, really, a lot and I would never been here without him. Last but not least, I am extremely grateful to my mother who passed away two years ago. My gratitude to you is boundless and cannot be expressed in sufficient words. A man will continue acting like a child until his mother's death, then he will age in a sudden.

Lausanne, 07 November 2016 H. Achour.

Curriculum Vitae

Full name: Hamed Achour
Date of birth: 08.01.1989
Place of birth: Constantine, Algeria

- PhD student/Research assistant in physics
- Engineer of EPFL in materials science

EDUCATION

2012 - 2016 PhD in Physics (EPFL): Transition metal clusters on h-BN/Rh(111): surface interaction and catalytic activity.

2010 - 2012 Master in materials science and engineering (EPFL): materials for microelectronics and microengineering.

Master thesis (Institute of MicroTechnology Neuchâtel (IMT)): Implementation of planarizing layers in tandem solar cells.

2007 - 2010 Bachelor in materials science (Mentouri University of Constantine, Algeria).

EXPERIENCE

2012 - 2016 **Teaching assistant in physics department (EPFL)**.
2011 **Internship (IMT)**: Development of triple junction and tandem thin film silicon solar cells.
2010 **Semester project (3D-Oxides company)**: Metal-oxide thin film deposition and characterization by Chemical Beam Epitaxy (CBE).
2010 **Semester project (EPFL)**: Gold nanoparticles deposition and characterization by Langmuir Blodgett method.

LANGUAGES SPOKEN:

Arabic, English, French.

HONOURS AND AWARDS:

Former holder of the Swiss Government Excellence Scholarship for Foreign Students.

Hobbies:

Football, Skiing, Ice-Skating, Tennis, Traveling, Fishing.